Hybrid-Electro

Hybrid-Electrolytes Design Strategy for High-Voltage Li-Ion Battery Systems

March　２０１９

Qiao Yu

Hybrid-Electrolytes Design Strategy for High-Voltage Li-Ion Battery Systems

Graduate School of Systems and Information Engineering
University of Tsukuba

March　２０１９

Qiao Yu

Hybrid-Electrolytes Design Strategy for High-Voltage Li-Ion Battery Systems

高電圧リチウムイオン電池実現のためのハイブリッド電解質開発

Qiao Yu

Department of Engineering Mechanics and Energy
Graduate School of System and Information Engineering
University of Tsukuba
Tsukuba, Ibaraki, Japan

March 2019

Chief Reviewer:

Prof. Haoshen Zhou (周豪慎　教授)

Department of Engineering Mechanics and Energy,
Graduate School of System and Information Engineering,
University of Tsukuba

Energy Technology Research Institute,
National Institute of Advanced Industrial Science and Technology (AIST)

The Thesis Review Committee:

Prof. Haoshen Zhou (周豪慎　教授)
Prof. Masayoshi Ishida (石田　政義　教授)
Prof. Keiichi Okajima (岡島　敬一　教授)
Prof. dr. Hirohisa Aki (安芸　裕久　准教授)
Dr. Hirokazu Kitaura (北浦　弘和　博士)

This thesis is based upon the following project:

Japanese Government (Monbukagakusho) Scholarship from Japanese Ministry of Education

China Scholarship Council (CSC)

National Basic Research Program of China (2014CB932300)

National Natural Science Foundation (NSF) of China (21633003)

This thesis is based upon the following publications:

Qiao, Y.; He, Y.; Jiang, K.; Liu, Y.; Li, X.; Jia, M.; Guo, S.; Zhou, H. High-Voltage Li-Ion Full-Cells with Ultralong Term Cycle Life at Elevated Temperature. *Adv. Energy Mater.* **2018**, 8, 1802322.

Qiao, Y.; Jiang, K.; Li, X.; Deng, H.; He, Y.; Chang, Z.; Wu, S.; Guo, S.; Zhou, H. A Hybrid Electrolytes Design for Capacity-Equivalent Dual-Graphite Battery with Superior Long-Term Cycle Life. *Adv. Energy Mater.* **2018**, 8, 1801120.

To my parents

両 親 へ

Contents

Chapter 1 General Introduction..1

Chapter 2 Experimental Section 9

Chapter 3 Hybrid Electrolytes Design (HED) for $LiNi_{0.5}Mn_{1.5}O_4$ | Graphite High-Voltage Li-ion Battery 19

3.1 Introduction..20

3.2 Results and Discussion..21

3.2.1 Deterioration mechanism of LNMO || Li half-cell and stable catholyte introduction......21

3.2.2 Choosing a competent anolyte for reversible Li-GIC at elevated temperature……….....40

3.2.3 Introduction of MOF-based separator for synergistical hybrid-electrolytes design…….48

3.2.4 Superior cycling performance of LNMO || Graphite full-cell at elevated temperature…53

3.3 Conclusion..61

Chapter 4 Hybrid Electrolytes Design (HED) for Graphite | Graphite Dual-Carbon High-Voltage Li-ion Battery 63

4.1 Introduction..64

4.2 Results and Discussion..65

4.2.1 Electrochemical performance of GIC processes in IL-based electrolyte……………..…65

4.2.2 Degradation mechanism of cation-GIC process in IL-based electrolyte…………………73

4.2.3 Discovering a reversible Li-GIC process in super-concentrated ether-based electrolyte..79

4.2.4 Synergistical hybrid electrolytes design for dual-graphite battery with capacity-equivalent electrodes loading…………………………………………………………………………….90

4.3 Conclusion..94

Chapter 5 General Conclusion and Perspective 97

References..99

Acknowledgements 107

Chapter 1

General Introduction

Chapter 1. General Introduction

The practical applications of rechargeable Li-ion batteries (LIBs) have run through our whole life, spreading from smart portable electronic devices to pure/hybrid electrical vehicles (EVs).[1-3] In order to respond the urgent demands for higher energy density LIBs, extensive research efforts focus on increasing the output voltage of full-cell while maintaining considerable specific capacity during long-term cycle life.[4-5] However, the development of high-voltage Li-ion full-cell is still severely hindered, due to the absence of suitable electrolyte system. Comprehensive modification strategies towards electrolyte system should not only guarantee a safe oxidative/reductive electrochemical window, but also satisfy good cathode-electrolyte compatibility, superior reversibility for anode electro-chemistry (conventional graphite, Si, etc.) and thermal stability, etc.[4] Such "perfect" optimizations can hardly be achieved, which simultaneously cover every aspects of the practical issues highlighted above. Thus, trade-offs between employing high-voltage cathodes and sacrificing the cycle performance have essentially reduced the significance of the original motivation.[4, 6-9]

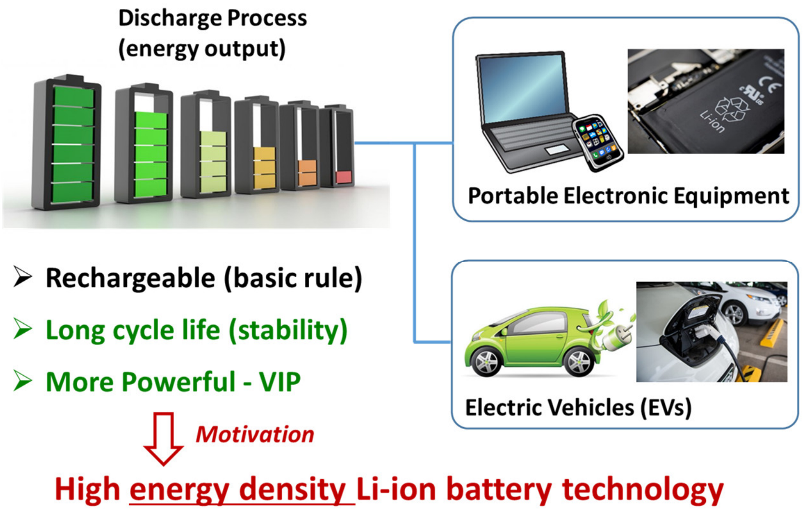

Figure 1. Widely employed Li-ion battery system in our daily life.

Generally speaking, for classic high-voltage cathode materials (Ni-rich and Li-rich layered oxides, LiNi$_{0.5}$Mn$_{1.5}$O$_4$ spinel, etc.), the most pronounced common drawback reveals to be the parasitic electrolyte oxidation, since the continuous accumulation of parasitic products would inevitably induce the increasing of interface resistance and capacity deterioration.[4]

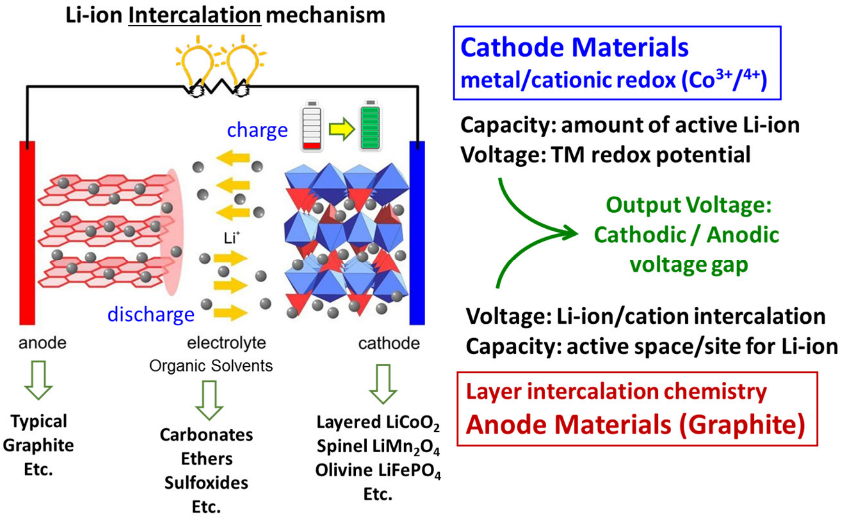

Figure 2. Typical working mechanism of currently Li-ion battery system.

Besides, just like a very serious blood disease flowing around the whole cell structure, such detrimental decomposition on cathode would lead to concurrent side reactions within other cell organs/components.[6] For instance, as a product of $LiPF_6$ salt decomposition, hydrofluoric acid (HF) would aggravate the dissolution of transition-metals (TMs) on cathode, resulting in both surface structural distortion and loss of reversible active capacity.[10-12] Moreover, TMs dissolution-crossover-deposition process would result in additionally irreversible loss of active Li-ion on practical anode in full-cell (reduction of LiC_6 on lithium-intercalated graphite anode), which leads to severer capacity loss than half-cell system.[13-15] As for remedial strategies, surface inert coating layer and additives would, to some extent, protect the cathode, and achieve relatively excellent cyclability in simplified Li foil-assembled half-cell.[16-19] However, these rigid strategies are by no means helpful to essentially enhance the oxidative stability of electrolyte. What was worse, the prices of these strategies are sacrificing the specific capacity and coulombic efficiency, which obvious against the original intention.[4] Furthermore, in a harsher but practical full-cell environment, all of the active lithium-ion are derived from cathode material, and trace consuming of active Li-ion (no matter cathode or anode) would lead to the irreversible loss of energy density.[9, 20] Thus, any electrolyte optimization strategy should not neglect the compatibility with cathode and reversibility towards commercial anode (graphite and Si), which substantially raise the difficulty of modification. Additionally, elevated temperature derived from practical cell operation environment would exacerbate the cell deterioration due to the poor thermal stability of typical $LiPF_6$ carbonate-based electrolyte.[16, 20-24] In a word, improving the energy density of cell can be likened as extend the capacity of wood bucket. Rigidly lengthening one piece of the boards on the bucket (e.g. introducing a high-voltage cathode) cannot obtain more capacity, unless comprehensive enhancements have been achieved, which is definitely a large project. In this case, although some considerable improvements have been achieved in high-voltage cathode half-cell systems, the corresponding full-cell system still suffer from rapid capacity deterioration, which is far from satisfying practical demand.

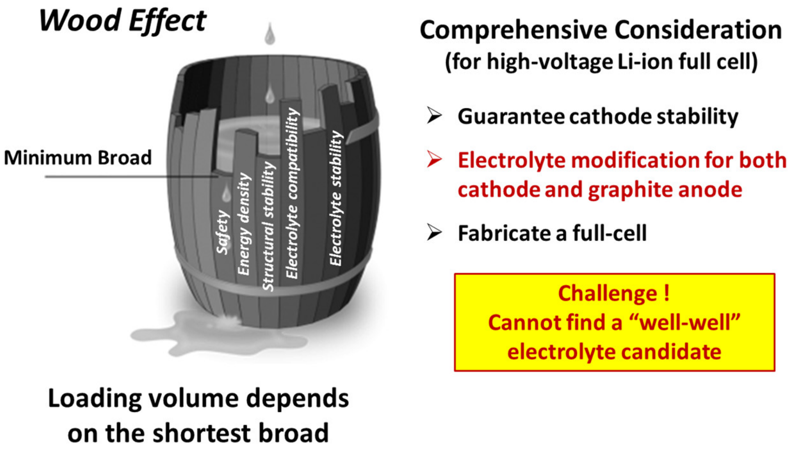

Figure 3. "Wood Effect" for the current development of high-voltage Li-ion batteries.

Another novel high-voltage Li-ion battery system focus on the anionic graphite intercalation process. Typically speaking, Owning to the interlayer gaps of the lattice, graphite can act as an intercalation host for either anion or cation guests at different redox potentials.[25-27] Benefit from the low electrochemical intercalation potential of Li^+ cation guest, graphite has been established as a classical anode material for state-of-art Li-ion batteries.[28-29] Recently, due to the high electrochemical intercalation potentials, anionic graphite intercalation chemistry (GIC) behaviors have received considerable attention for designing novel energy storage devices.[30-34] Actually, in 1990s, the model of dual-graphite intercalation battery has been introduced,[26] in which, simultaneously, anion/cation guests can intercalate into graphite-based cathode/anode respectively, and the output voltage of the cell can be provided by the redox potential gap between the pair of amphoteric GIC processes. In nonaqueous electrolyte systems, the concept of intercalation-based dual-graphite batteries have been further modified, wherein the Li-GIC and anion-GIC (PF_6^-, $TFSI^-$, etc.) have been in the focus of researches.[30, 35-41] Compared with conventional Li-ion batteries, the most outstanding advantages of dual-graphite energy storage devices can be summarized as: (I) high output voltage; (II) environmental safety; (III) cost benefits.[30, 38]

However, a dominated drawback is concentrated on the anion-GIC process, during which the intercalation potential typically approaches 5 V vs. Li/Li^+, while conventional organic electrolytes cannot endure such a high working potential, resulting in continuously oxidative electrolyte decomposition and low coulombic efficiency (CE).[30, 36] Owning to their high stability vs. electrochemical oxidation, the employment of ionic liquids (ILs) based electrolytes can efficiently restrain the related cathodic degradation, which is well proved within the graphite/Li (anion-GIC) half-cell.[36, 38, 40-43] Unfortunately, as for the cation-GIC process hosted on graphite anode in IL electrolyte, although the inner degradation mechanism has not been clearly illustrated, the irreversible behavior can be ascribed to the unstable solid electrolyte interphase (SEI) protective film and/or harmful co-intercalation of large solvent cation (Pyr_{14}^+, EMI^+, etc.).[38, 42, 44] As a result, due to the low CE and weak reversibility on anodic side, intercalated anion on the cathodic side would be trapped within graphite cathode, in which the active space cannot be released for subsequent anion-GIC process. Notably, rigidly assembling excessive cathode would, indeed, provide preparatory space to remedy the irreversible de/intercalation, however, breaking the balance of the capacity-equivalent loading proportion between cathode and anode would inevitably lead to the waste of output power density, which cannot essentially solve the practical problems. Thus, the employment of IL become a “double-edged sword” for dual-graphite technology. Moreover, in order to enabling the use of ILs, graphite anode is replaced by metal oxides and metallic anodes, only retaining the anion-GIC hosted on graphite cathode in the design of some dual-ion batteries.[32, 45-47] Although the cycling stability of dual-ion batteries, to some extent, have been improved, some precious superiorities of dual-graphite battery have also been sacrificed. For example, the use of metal oxide anodes would draw down the cell voltage, and the employment of metallic anodes would unavoidably introduces their original defects: dendrite issue; low initial CE loss and volume expansion. In this case, without sacrificing the advantages, designing modification strategies within the dual-graphite framework is pressing.[30, 38]

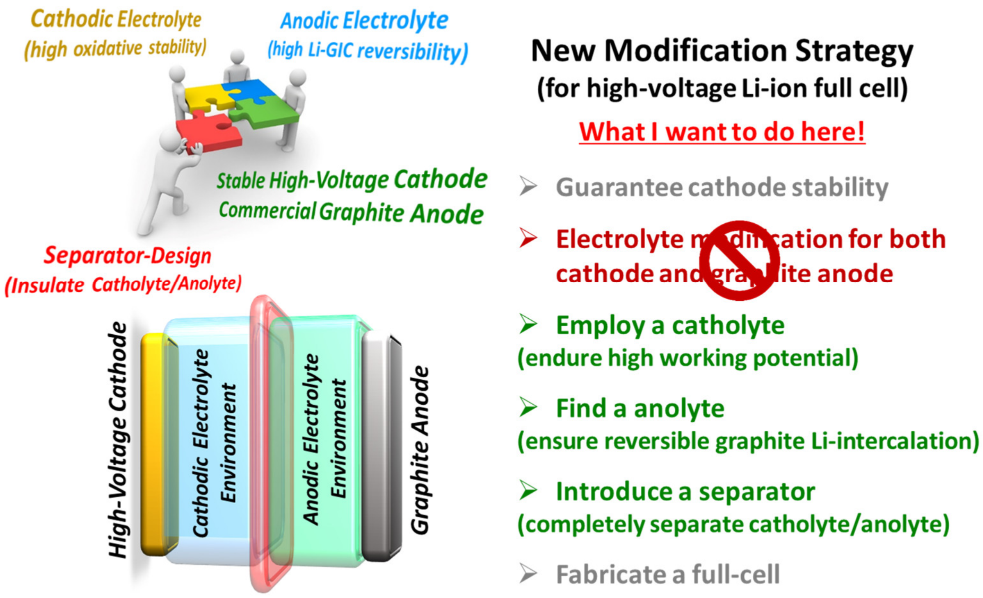

Figure 4. Concept of Hybrid-Electrolytes-Design (HED) strategy.

Herein, for the 1st issue, LNMO cathode-based Li-ion battery system, without being limited within specific remedial modifications, we try to make a comprehensive optimization towards the basic cell architecture by introducing a hybrid-electrolytes design strategy. Typical 5 V-class spinel $LiNi_{0.5}Mn_{1.5}O_4$ (LNMO) and graphite anode are employed as a competitive electrode couple.[6, 48-50] The design principle of hybrid-electrolytes strategy is separating the cathodic/anodic electrochemical processes within their adaptive electrolyte environments, and solving the certain problems without mixing additionally concurrent influences. Specifically, isolated by a porous sieve-like

MOF-based separator, ionic liquid catholyte (LiTFSI/Pyr_{13}TFSI) exhibits outstanding oxidative stability and high compatibility with LNMO cathode, while an equimolar LiTFSI/G_3 complex is employed as anolyte due to its high graphite-intercalation-chemistry (GIC) reversibility. Besides, both of the electrolyte systems deliver superior thermal stability and nonflammability. As a result, the high-voltage LNMO/graphite Li-ion full cell fabricated with hybrid-electrolytes strategy delivers ultrahigh capacity retention rate of 83.8% over 1000 cycles at harsh elevated temperature condition. The realization of long-term cycling reversibility and stability also demonstrates that the novel cell architecture herein can be further extended as a promising strategy to promote the practical development of high-voltage Li-ion full-cell systems.

As for the 2nd issue, dual-carbon high-voltage battery system, Recently, by adding anodic SEI-forming additives into IL electrolytes, Rothermel et al. provided an effective strategy to achieve the reversible cycling of dual-graphite cell.[38] However, the long-term cycling stability and CE still need to be further improved to offset the moderate energy density, which is inherently limited by specific capacity of anion-GIC. In this study, we introduce a specific hybrid electrolytes design into dual-graphite battery system, in which a Nafion-based separator segregates two different electrolyte systems into each of their suitable GIC environments. On the cathodic side, outstanding oxidative stability of IL electrolyte (LiTFSI-Pyr_{13}TFSI) enables the high reversibility of anion-GIC (TFSI-GIC) process. Simultaneously, on the anodic side, specific aggregated ion-pair structure within a super-concentrated ether-based electrolyte (LiTFSI-G_3) insures the highly reversible Li-GIC process. Moreover, the full-cell has been assembled with balanced capacity-equivalent mass loading proportion between cathode and anode, while this very important practical issue has also been firstly highlighted to the forefront in dual-graphite/ion cell systems. The hybrid electrolytes strategy in dual-graphite cell synergistically combines the advantages of each electrolyte systems, displaying a promising high CE (around 99.7%) and superior long-term cycling stability (over 3000 cycles at 100 mA/g current density). In addition, spectroscopic investigations have been systematically conducted to clearly reveal degradation mechanism of cation-GIC in IL electrolyte system, and elucidate the influence of different electrolyte features on the mechanism of Li^+ intercalation (Li-GIC) processes.

Chapter 2

Experimental Section

Chapter 2. Experimental Section

Modification of $LiNi_{0.5}Mn_{1.5}O_4$ (LNMO) spinel cathode

The principle and reason for this modification of LNMO was further interpreted in the corresponding following section. All the chemicals employed in this synthesis section were purchased from Wako Pure Chemical Industries Ltd. without additional exception.

(I) Synthesis of $MnCO_3$ microspheres. Manganese sulphate ($MnSO_4{\cdot}H_2O$, 0.507 g) and sodium bicarbonate ($NaHCO_3$, 2.32 g) were separately dissolved in 200 ml distilled water. 20 ml of ethanol was then added to the $MnSO_4$ solution under vigorous magnetic stirring, and the $NaHCO_3$ solution is continuously injected for precipitation. The mixture solution was maintained within thermostat (25°C) for 3 h ($Mn^{2+} + HCO_3^- + OH^- = MnCO_3\downarrow + H_2O$). The as-precipitated $MnCO_3$ was further obtained by centrifuging and washed with distilled water and absolute alcohol solution for 3 times, and then dried at 80°C for 1 h in vacuum.

(2) Synthesis of yolk-structured MnO_2 microspheres. The as-prepared $MnCO_3$ (0.2 g, insoluble) microsphere powder was dispersed into 40 ml distilled water. Then 20 ml of 0.032 mol/L $KMnO_4$ solution was added under vigorous stirring for 40 min to form a homogeneous solution ($2MnO_4^- + 3MnCO_3 + 2H^+ = 5MnO_2 + 3CO_2 + H_2O$). The color of the solution gradually turned from purple into dark brown, during which the core-shell structured $MnCO_3$@MnO_2 microsphere could be obtained. Then 20 ml of 0.6 mol L1 HCl was added into the above suspension and the mixture was continuously stirring for 2 min followed by a rapid centrifuging step ($2H^+ + MnCO_3 = Mn^{2+} + H_2O + CO_2$). In this case, the space between MnO_2 shell and $MnCO_3$ core can be obtained by HCl etching, resulting the formation of yolk-structured $MnCO_3$ (core) @ MnO_2 (shell) micro-sphere. The as-obtained powder was washed (with distilled water and absolute alcohol solution) for several times and dried at 80°C for 1 h in vacuum. Finally, the as-prepared yolk-structured $MnCO_3$ (core) @ MnO_2 (shell) micro-sphere was

further oxidized to pure yolk-structured MnO_2 microsphere by additional heat treatment (400°C for 10 hours).

(3) Synthesis of yolk-structured $LiNi_{0.5}Mn_{1.5}O_4$ microspheres. The as-prepared yolk-structured MnO_2 microsphere was mixed and ground with lithium hydroxide mon-hydrate ($LiOH{\cdot}H_2O$) and Nickel nitrate hexahydrate ($Ni(NO_3)_2{\cdot}H_2O$) in the stoichiometric molar ratio (Li:Ni:Mn=1.05:0.5:1.5). Then the mixtures were calcined at 800°C for 20 h. The heat treatment process was carried out in air atmosphere. It should be mentioned that the synthesis methods here are similar to previous report for $LiMn_2O_4$ synthesis.[51-52]

Electrolytes

Ionic liquid: 1-methyl-1-propylpipridinium, namely $Pyr_{13}TFSI$, was purchased from Solvionic Chemicals. Tri-ethylene glycol dimethyl ether (G_3) (Sigma Aldrich, >99%) was dried over freshly activated 4 Å molecular sieves for several days. Lithium bis(trifluoromethane) sulfonimide salt (LiTFSI, purity of >98 %, Wako Chemicals) was dried by heating under vacuum at 80 °C oven overnight. Electrolytes are prepared and stored in a glove box under Ar atmosphere. The water concentration in the electrolyte measured by Karl Fischer titration was around 30 ppm.

Preparation of MOF-based Separator

The HKUST-1 precursor solution was prepared according a process based on the reported procedures[53-54]: cupric nitrate trihydrate ($Cu(NO_3)_2{\cdot}3H_2O$, 0.72 mmol, 99.5%, TCI, Tokyo Chemical Industry Co., Ltd.) was dissolved into 125 mL ethanol (Wako Pure Chemical Industries Ltd. >99.5 %) under continuously stirring, and then the equal volumetric 1,3,5 benzenetricarboxylic acid (0.4 mmol, 99.5%, TCI, Tokyo Chemical Industry Co., Ltd.) ethanol solution was added into the above $Cu(NO_3)_2{\cdot}3H_2O$ solution. After stirring for 2 h, the mixed system changed from a blue clear state to a cloudy one. The MOF-based separators were fabricated by a vacuum filtration method.[55] The HKUST-1 precursor solution was filtered through the conventional PP separators firstly. It was followed by the addition of 0.05 mg mL^{-1} poly(vinylidene fluoride-co-hexafluoropropylene) (P(VDF-HFP) polymer, Mw 455000), Sigma Aldrich, >99%) colloidal fluid. After drying at 60°C for 12 h in a vacuum oven, the MOF@P(VDF-HFP) membrane on PP with an areal loading of ~0.24 mg/cm^2 were obtained.

Preparation of Nafion-based Separator

The pristine commercial Nafion 117 membrane (N117, in the protonated form, H-Nafion) was purchased from Sigma Aldrich. The pre-treatment processes for the as-received Nafion-based separator were very similar as the ones present in previous classic reports.[56-57] In brief, firstly, in order to transfer the Nafion membrane into a form of $–SO_3H$, the Nafion film was pretreated by boiling in a bath of deionized water for 3~5 h, then transferred into another bath containing 5% hydrogen peroxide (H_2O_2, Wako Chemicals) for 3~5 hours. Then Nafion membrane was boiled in a dilute sulfuric acid (0.5 M, H_2SO_4, Wako Chemicals) solution for 2 hours and finally washed in boiling deionized water. For the subsequent Li^+ exchange procedure, the Nafion membrane was boiled in a solution of 1 M LiOH (Wako Chemicals) in 1:2 volume ratio of ethanol and deionized water for 2 h under strong stirring. The membrane was then re-rinsed and re-washed in boiling deionized water again to remove the residue salt and ethanol. Finally, after vacuum drying at 80° C for 5 days, the lithiated Nafion membrane was transferred into an argon-filled glove box and punched into separator plates (14 or 16 mm in diameter). Before assembled into the coin cell, the lithiated Nafion-based separators were bathed into a specific home-made device (very similar as the permeation V-type device shown in corresponding following section) filled with corresponding hybrid-electrolytes for 5 days at ~55° C (for further infiltration/wetting).

Electrodes Preparation

The as-prepared LNMO and graphite powder (Lion Chemical Industry Co., Ltd.) were employed as electrode materials. 0.2 g electrode powder was stirring into a binder gel solution (0.37 ml), which composed by polyvinylidene fluoride (PVDF, Du Pont-Mitsui Fluorochemicals Co. Ltd.) powder and N-methyl pyrrolidine (NMP, Sigma Aldrich, 99%) solvent (PVDF:NMP=6:94 wt%). The obtained slurry was homogeneously coated onto current collector (Al foil for LNMO and Cu foil for graphite) by a scraper (0.1 mm height). After tiny pressing procedure, the active materials-loaded metal foil was dried at 80 °C in an air oven for 1 hour, and final electrode plates (11 mm in diameter) were punched out. The electrode plates were placed in separated glass bottles with further drying process in vacuum at 100 °C for 10 hours, and then transferred into a glove box under Ar atmosphere. The mass loading for each LNMO electrode plate was 2.0-2.1 mg/cm^2. Typically, the mass loading ratio (LNMO:graphite) was fixed at 2:1 and 1:1. The mass loading can be controlled by the height of scraper.

0.2 g graphite powder (Lion Chemical Industry Co., Ltd.) was stirring into a binder gel solution (0.37 ml), which composed by polyvinylidene fluoride (PVDF, Du Pont-Mitsui Fluorochemicals Co. Ltd.) powder and N-methyl pyrrolidine (NMP, Sigma Aldrich, 99%) solvent (PVDF:NMP = 6:94 wt%). The obtained slurry was homogeneously coated onto Cu (anode) or Al (cathode) foil current collector by a scraper (0.1 mm height). After tiny pressing procedure, the graphite-loaded metal foil was dried at 80 °C in an air oven for 1 hour, and final electrode plates (11 mm in diameter) were punched out. The electrode plates were placed in separated glass bottles with further drying process in vacuum at 100 °C for 10 hours, and then transferred into a glove box under Ar atmosphere. The mass loading for each cathode plate was 2.0-2.1 mg/cm^2.

Cell Assembly

The typical assembly process of the 2032 coin-type cell and in-situ Raman cell present the same as our previous reports.[58] The in-situ Raman cell herein has been designed and modified based on the typical cell (Hohsen Corp., Osaka, Japan).[59] In detail, a thin quartz window (thickness, 0.5 mm) has been fixed on the top of the cell as a sight window. The cathode was assembled at the bottom of the cell with the active material-face upward. On the top of the cathode, 50-100 μL of electrolyte was homogeneously dropped onto the glassy fiber filter separator (GF/A, Whatman). As a standard two-electrode configuration cell, lithium foil (thickness, 0.4 mm) was assembled at the top as the reference and counter electrode. Note that, a small hole was punched on the center of both the separator and Li foil, through which the laser and Raman signals can fluidly cross. Note that the assembly of the cell was conducted in an Ar-filled glove box that has a dew point of around -90 °C and O_2 content below 5 ppm.

Electrochemical Measurements

For coin-type cells, the galvanostatic electrochemical measurements were carried out under potential control using the battery tester system HJ1001SD8 (Hokuto Denko) at 25 °C. Typically, the characterizations of the cell were carried out under galvanostatic control at the specific current density from the open-circuit potential (OCP) unless other noted. For the in-situ Raman test, the electrochemical experiments were carried out under the control of a potentiostat (Potentiostat/Galvanostat PGSTAT30, Autolab Co. Ltd., Netherlands) at room temperature. The current and potential outputs from the potentiostat were recorded by a multifunction data acquisition module/amplifier (PGSTAT30 Differential Electrometer, Autolab), which was controlled by General Purpose Electrochemical Software (GPES). The cells were operated with a potential limit between: 2.55-4.75 V (for dual-graphite full-cell); 0.01-3.0 V (for anodic Li-GIC half-cell) and 2.8-5.0 V (for cathodic TFSI-GIC half-cell) in the study. The cells were operated with a potential limit between: 3.4-4.8 V (for LNMO || graphite full-cell); 3.0-4.9 V (for LNMO || Li half-cell) and 0.01-3.0 V (for graphite || Li half-cell) in the study.

Before each electrochemical characterization, the cells were kept on open circuit for 8-10 hours. All of the potentials in this study were referenced to Li/Li^+.

Characterizations

Raman Measurements

The Raman spectra were recorded using a JASCO microscope spectrometer (NRS-1000DT). The excitation light of an air-cooled He−Ne laser at 632.8 nm wavelength was focused on the electrode surface through a 50×long working distance lens (Olympus America Inc.). The confocal slit was adjusted to be 4.0 µm to minimize the band broadening effect due to the contribution of non-confocal signal. The scattered light was collected in a backscattering geometry along the same optical path as the pumping laser. The power of laser beam delivered to the electrode surface was roughly 10% of the maximum 30 mW laser intensity, unless specified, to avoid degradation to the products and/or carbon-based cathode. The Raman spectrum acquisition time varied from 600-800 s with 1-2 accumulations. At least 3 different places on the electrode surface at each cathode plate were checked to ensure the Raman spectra were credible and reproducible. The spectral resolution of the Raman spectra in the study was ca. 1.0 cm^{-1}.

HR-TEM, SEM and X-Ray Photoelectron Spectroscopy Characterizations

HR-TEM images were obtained using a JEM-2100 (HR) electron micro-scope. SEM measurements were performed on a LEO Gemini Supra 35 system, and images were obtained at an electron current of 50 pA with an accelerating voltage of 5 kV. X-ray photoelectron spectroscopy (XPS) was performed using a VG scientific ESCALAB 250 spectrometer with monochromic Al Kα excitation (1486.6 eV). Note that, in order to restrain the exposure time to the ambient, XPS samples (cycled Li foil anode) were tightly sealed into a glass bottle (fill with Ar gas), and transfered to the XPS chamber as quickly as possible.

For the pre-treatment procedures: The cycled cells were transferred into an Ar glove box once the discharge processes finished, and the electrodes were extracted from the cell and placed in a glass bottle. The cathodes were twice rinsed by dimethoxyethane (DME, Sigma Aldrich, 99%) to wash off the electrolyte salt and the residual solvent, and then evaporated in a vacuum chamber, connected to the glove box, for 15~30 min. The dried cathodes were moved back to glove box and placed onto a SEM or XPS sample holder. The sample holder was sealed in an airtight container and then transferred into the SEM or XPS sample loading chamber. For the HR-TEM observation, the dried electrodes were ultra-sounded in newly-filled DME solvent. After some of the electrode powders were divorced away from the bulk electrode plate, we employed a Cu mesh to harvest the dispersed electrode materials for HR-TME observation. Note that the time from open the sealed container to pump down the chamber was less than 3 seconds, and we assumed the morphology and the component of electrode surface would not change for such a short time exposure to the open air.

Nuclear Magnetic Resonance (NMR) Spectroscopy Characterizations

The NMR spectra were recorded using a spectrophotometer (500MHz Ultra-Shield^{TM}, Bruker). Typically, 128 times were accumulated for one spectrum (both ^{1}H and ^{19}F). After corresponding electrochemical treatments, the cells were transferred to an Ar-filled glove box, and the electrodes and separators were extracted without further pretreatment, respectively. 750 μL of D_2O (99.9 atom % D, Wako Chemicals) was used to extract the souluble products (carboxylates and fluorids) from the electrodes and the separators, then the solution was transferred to septa-sealed NMR tube. To quantify the amount of formate, acetate species (carboxylates) and/or LiF (fluoride), 1 μL of benzene (C_6H_6, Sigma Aldrich, 99%) and 1uL of fluorobenzene (C_6H_5F, Sigma Aldrich, 99%) were mixed and injected through the septa and empolyed as an internal/inner standard. The method here is very similar as the one in our previous works.[60]

Inductively-Coupled Plasma (ICP) Characterizations

ICP-OES (optical emission spectroscopy) results were recorded using Thermo Scientific iCAP 5600 and PerkinElmer Optima 4300 DV. Metal loss from the LNMO-based electrodes were quantitatively confirmed measuring the Mn and Ni-ion concentrations both in the electrolyte solutions and on the lithium-metal anode.[15-16, 20-21] The cycled separators (infiltrated by cycled electrolyte solutions) and lithium electrodes were bathed in DME solvent for 5 hours aging. The separator was salvaged out, then the DME solution and Li anode were mixed with a mixture of concentrated hydrochloric acid and nitric acid mixture (3:1 in volume ratio). The solution was heated in a microwave for 2 hours (150°C). Note that, for measuring the dissolved Mn/Ni, only the electrolytes would be extracted by DME solution, while the Li anode would not be drop into acid solution anymore. The emission lines of Mn and Ni were employed for quantification and calibration.

Chapter 3

Hybrid Electrolytes Design (HED) for $LiNi_{0.5}Mn_{1.5}O_4$ | Graphite High-Voltage Li-ion Battery

Chapter 3. Hybrid Electrolytes Design (HED) for $LiNi_{0.5}Mn_{1.5}O_4$ | Graphite High-Voltage Li-ion Battery

3.1 Introduction

The practical applications of rechargeable Li-ion batteries (LIBs) have run through our whole life, In order to obtaining higher energy density in rechargeable Li-ion batteries, the key point focus on increasing the output voltage, while maintaining considerable specific capacity during long-term cycling in a practical full-cell system. However, the problems cannot be simplified by introducing a high-voltage cathode and a stable electrolyte against oxidative decomposition in a half-cell system. Since, for a practical full-cell system with limited active-Li^+ source, electrolyte modification strategies should not only guarantee a safe oxidative/reductive electrochemical window, but also satisfy good cathode-electrolyte compatibility, superior reversibility for anode electro-chemistry (conventional graphite, Si, etc.) and thermal stability, etc. Such "perfect" optimizations are extremely hard to be achieved, because simultaneously covering every aspects of these practical issues is very difficult. Thus, trade-offs between employing high-voltage cathodes (high energy density) and sacrificing the cell cyclability have essentially reduced the significance of the related researches/modifications.

In this study, not rigidly limiting within additives/electrolyte/electrode modifications in half-cell system (a fundamental research level), we try to alleviate the difficulties of optimizations on high-voltage Li-ion full-cell systems (a practical aspect), and disperse the above-mentioned pressures into dual separated cathodic/anodic-reaction environments. Followed by this core motivation, we introduce a novel dual-organic hybrid-electrolytes cell architecture design strategy. A MOF-based separator is employed to separate the full-cell into pair of relatively independent electrolyte environments, while only Li^+ can fluently transport through the MOF-derived sieve. LiTFSI/Pyr_{13}TFSI ionic liquid-based electrolyte is rationally employed as catholyte, due to its superior oxidative and thermal stabilities. Meanwhile, we introduce another independent anolyte system, equimolar LiTFSI/G_3 complex, which reveals pronounced irreversibility during Li^+ de-/intercalation on graphite anode. As a result, fabricated with this hybrid-electrolytes strategy, a 5 V-class $LiNi_{0.5}Mn_{1.5}O_4$/graphite full-cell delivers ultra-high long-term cyclability and superior capacity retention rate at elevated temperature (83.8% after 1000 cycles). The achievement of outstanding electrochemical performance at harsh cell working condition (high-voltage and elevated-temperature) strongly prove the practical availability of the newly-introduced cell architecture.

In a word, by specifically modifying the cell architecture, we introduced a novel optimization strategy (hybrid-electrolytes design) for improving the electrochemical performance of high-voltage Li-ion full-cell device at harsh elevated temperature environment. Advantages and drawbacks of dual electrolyte systems can be synergistically tuning within their isolated environments. We hope this feasible design strategy can be further developed as a universal design principle, promoting the practical application of high-voltage Li-ion full cells.

3.2 Results and Discussion

3.2.1 Deterioration mechanism of LNMO || Li half-cell and stable catholyte introduction.

In this study, we select 5 V-class spinel $LiNi_{0.5}Mn_{1.5}O_4$ (LNMO) as the targeted high-voltage cathode, due to its 4.7 V (vs. Li/Li^+) Ni^{2+}/Ni^{4+}-based redox potential and 148 mAh/g theoretical capacity, which indicates nearly 25% higher energy density (~650 Wh/kg) beyond conventional $LiFePO_4$ and $LiCoO_2$ cathodes.[61] Before systematically discussing the electrolyte-related issues, the modification towards LNMO cathode would be briefly introduced. Most of the reported LNMO spinel are, indeed, non-stoichiometric disordered $LiNi_{0.5}Mn_{1.5}O_{4-\delta}$ structures, in which the existence of Mn^{3+} would achieve a lower plateau around 4.0 V (vs. Li/Li^+).[61-63] More importantly, the Mn^{3+}-related Jahn-Teller effect would induce significant capacity loss, especially at elevated temperature, which is a specific inherent defect for LNMO spinel system.[61] Herein, benefitting from morphology architecture and re-annealing calcination, an ordered spinel phase can be obtained, and the Mn^{3+} concentration has been effective controlled, which proved by the obvious restraining of Mn-related plateau during cycling and corresponding XRD characterization (Figure 1~6).

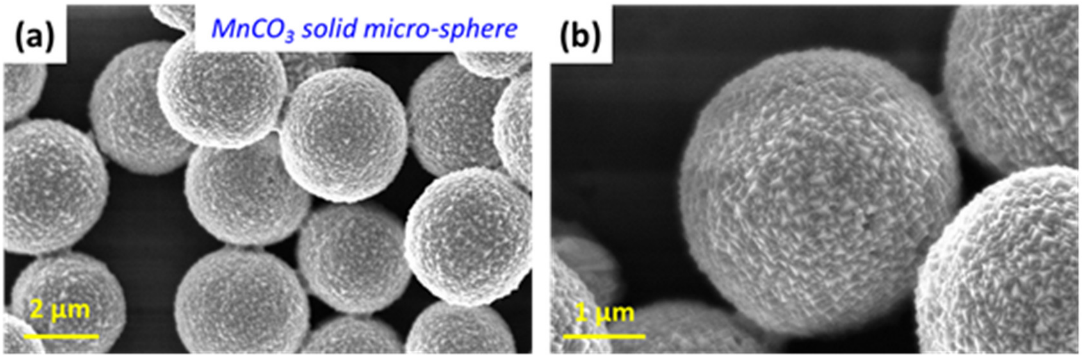

Figure 1. SEM images of as-prepared $MnCO_3$ microsphere.

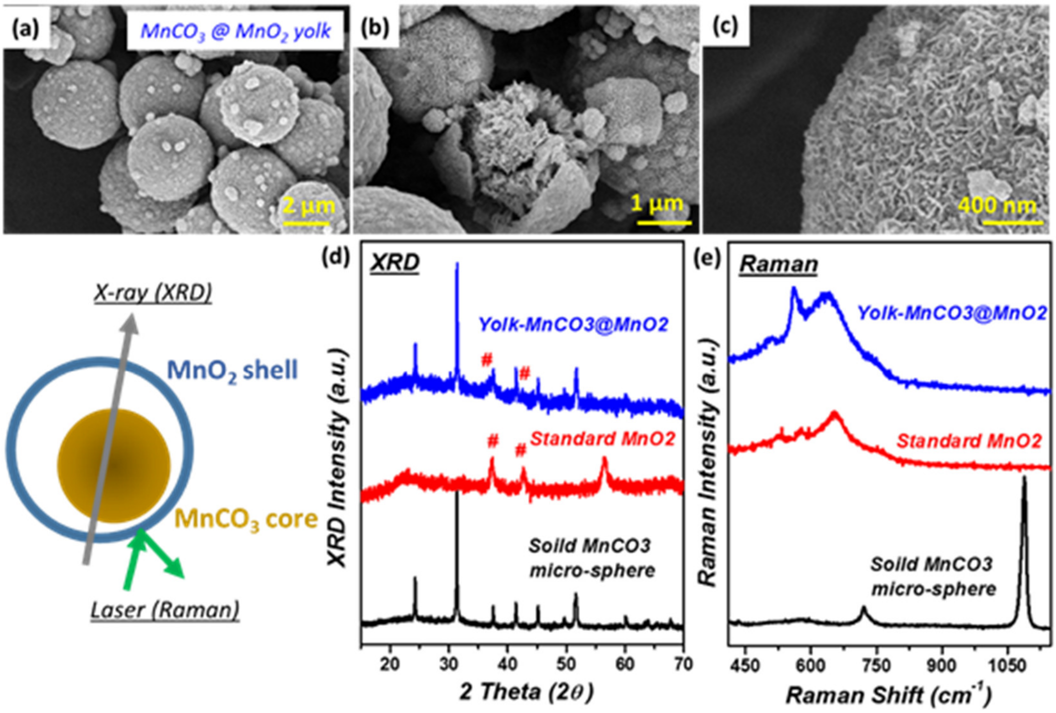

Figure 2. (a to c) SEM images, (d) XRD patterns, and (e) Raman spectrum of as-prepared yolk-structured $MnCO_3@MnO_2$ microspheres.

Firstly, we obtained $MnCO_3$ micro-sphere (Figure 1). After appropriate HCl-related etching treatment, the space between $MnCO_3$-core and MnO_2-shell would be achieved, which can be partially proved by the broken microsphere shown in b. Different from the $MnCO_3$, $KMnO_4$-oxidized surface of the microsphere presents an obvious porous structure, which can be attributed the evolution of CO_2 gas: $2KMnO_4(aq) + 3MnCO_3 + H_2O = 5MnO_2 + 3CO_2 + KOH(aq)$. The MnO_2-shell do not react with HCl, thus the $MnCO_3$-core would be partially etched (the concentration/amount of HCl has been controlled).[51] As a result, the yolk-structured $MnCO_3@MnO_2$ microspheres can be obtained. Based on XRD, both inner $MnCO_3$-core and poorly crystallized MnO_2 shell can be observed. However, due to the sheltering of MnO_2-shell, Raman spectrum (a relative surface spectroscopy) of the yolk-structured sample do not deliver any characterization signal/peak assigned to $MnCO_3$.

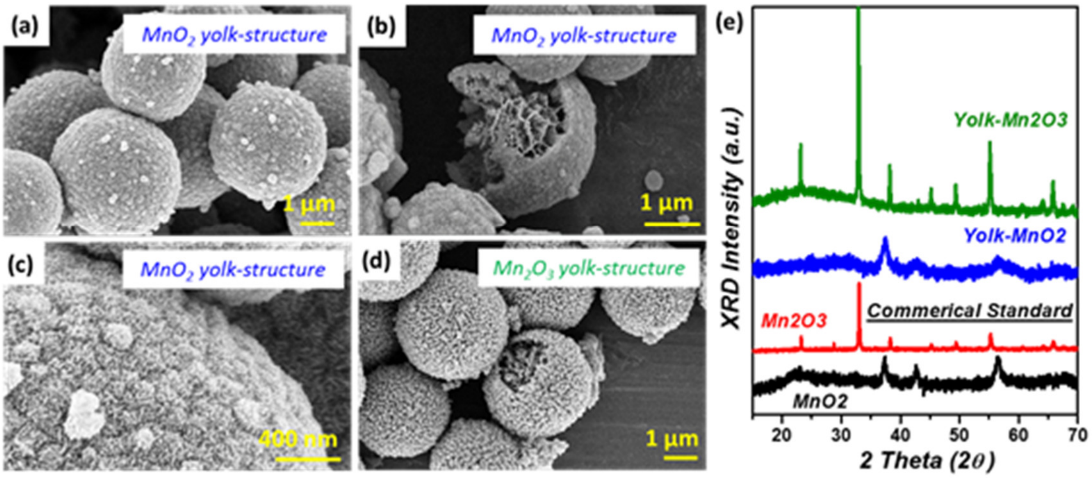

Figure 3. SEM images of yolk-structured MnO_2 (a to c) and Mn_2O_3 (d). (e) Corresponding XRD patterns are collected as compared with standard patterns.

After 400°C heat treatment, the inner $MnCO_3$-core has been totally oxidized into MnO_2,[49] which is illustrated by corresponding XRD pattern (blue trace). Compared with the $MnO_2@MnCO_3$, the surface morphology of MnO_2 microspheres do not suffer from obvious change. Besides, if the heat-treat temperature increases to 530°C, the final oxidative product would be turned to Mn_2O_3.[51-52]

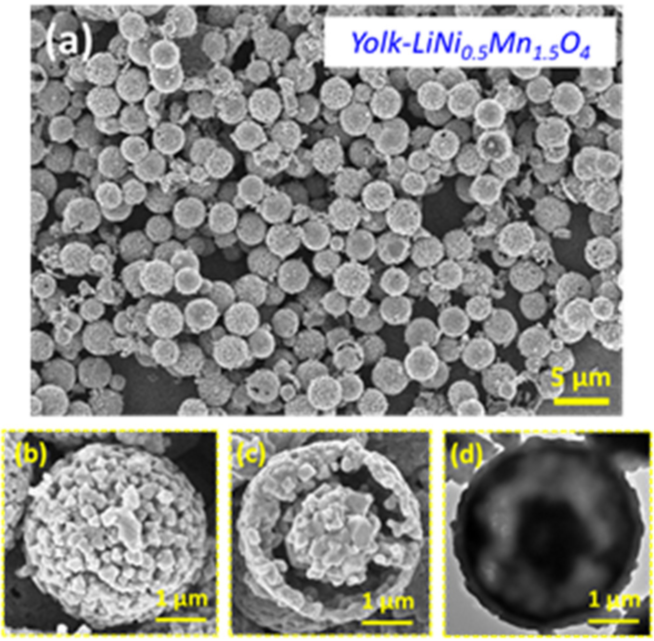

Figure 4. SEM and TEM image of the as-prepared yolk-structured $LiNi_{0.5}Mn_{1.5}O_4$ microspheres. Both the SEM image of the broken microsphere (c) and TEM image (d) demonstrate the yolk morphology.

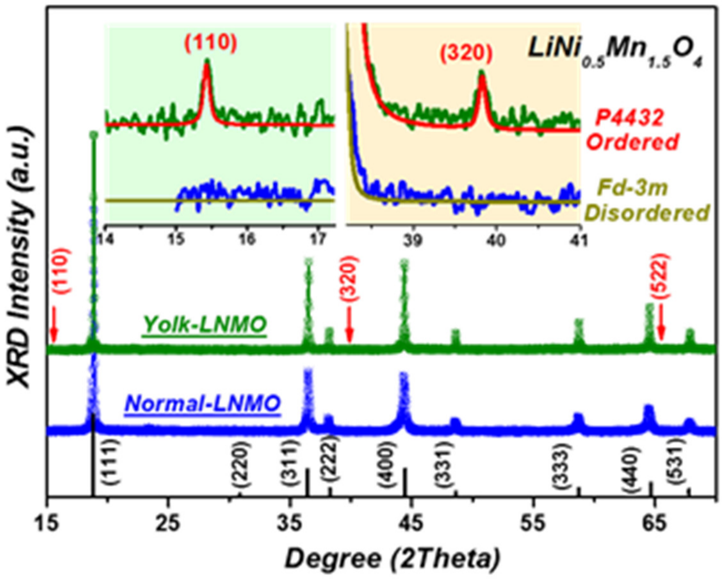

Figure 5. XRD patterns of the yolk-structured (green trace) and normal (blue trace) $LiNi_{0.5}Mn_{1.5}O_4$ spinel.

The dominate difference between the two patterns is mainly attributed the different crystallographic structures: disordered face-centered spinel (Fd3m, blue) and ordered cubic ($P4_332$, green).[61-63] Actually, $LiNi_{0.5}Mn_{1.5}O_4$ (LNMO) with different morphologies and various particle sizes can be synthesized by varying synthesis routes. However, most of the reported $LiNi_{0.5}Mn_{1.5}O_4$ spinel is a non-stoichiometric, disordered, Mn^{3+}-contained and oxygen deficient one, indicates $LiNi_{0.5}Mn_{1.5}O_{4-\delta}$. (disordered Fd3m). For the well-ordered phase stoichiometric $LiNi_{0.5}Mn_{1.5}O_4$, it can be prepared by prepared by using very slow cooling followed by lengthy reannealing and continuously O_2 supplement. Typically, ordered LNMO (P4332) induced low structural reversibility at high current rate, while disordered LNMO (Fd3m) can maintain good structural reversibility.[63] However, due to the presence of Mn^{3+} in disordered LNMO (Fd3m), the Mn^{3+} dissolution would lead to the loss of active material and dissolution-migration-deposition, which would severely poison the anode.[61] Herein, without additional O_2-purging nor slow cooling process, we successfully synthesis an ordered-phase-contained LNMO powder. The yolk-structure facilitates the production of ordered phase, and further restrains the Mn^{3+} concentration. At the same time, the special morphology would also help to modify the rate performance.

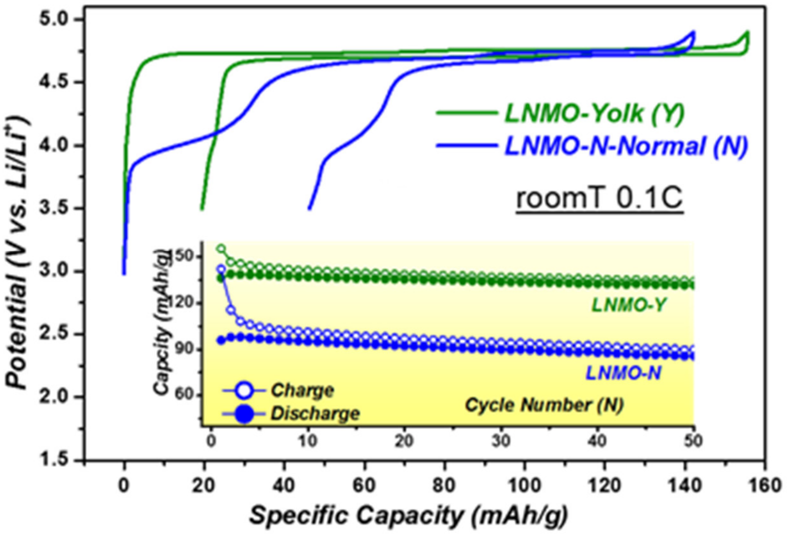

Figure 6. Galvanostatic charge/discharge curves of LNMO cathodes in half-cells assembled with $LiPF_6$/EC-DEC electrolyte system in room temperature (25°C). The current rate is 0.1 C (1C = 148 mAh/g).

The normal LNMO (blue traces) delivers an additionally Mn^{3+}-related plateau around 3.0 V vs. Li/Li^+, while yolk-structured LNMO (green traces) dominantly presents typical Ni-related plateau(s) around 4.7 V ($Ni^{2+}/Ni^{3+}/Ni^{4+}$).[62-63] In this case, the restrained-Mn^{3+} concentration in yolk-structured LNMO has been well proved by electrochemical performance. Although, both of the LNMO samples suffer from irreversible capacity loss at the upper Ni-related plateau (inevitable electrolyte decomposition in $LiPF_6$/carbonates), the disordered LNMO (Fd3m) presents additional Mn^{3+}-related capacity loss (Jahn-Teller effect).[61] Besides, the yolk-structured LNMO sample also exhibits relatively better coulombic efficiency and capacity retention rate. Notably, rigorously speaking, merely based on XRD characterization, the observation of ordered-phase-related peaks cannot demonstrate that the yolk-structured LNMO is a pure ordered structure. We speculate that the as-prepared yolk-structured LNMO is a mixture of the two phases, since there still present very trace part of Mn^{3+}-based plateau around 3.0 V.

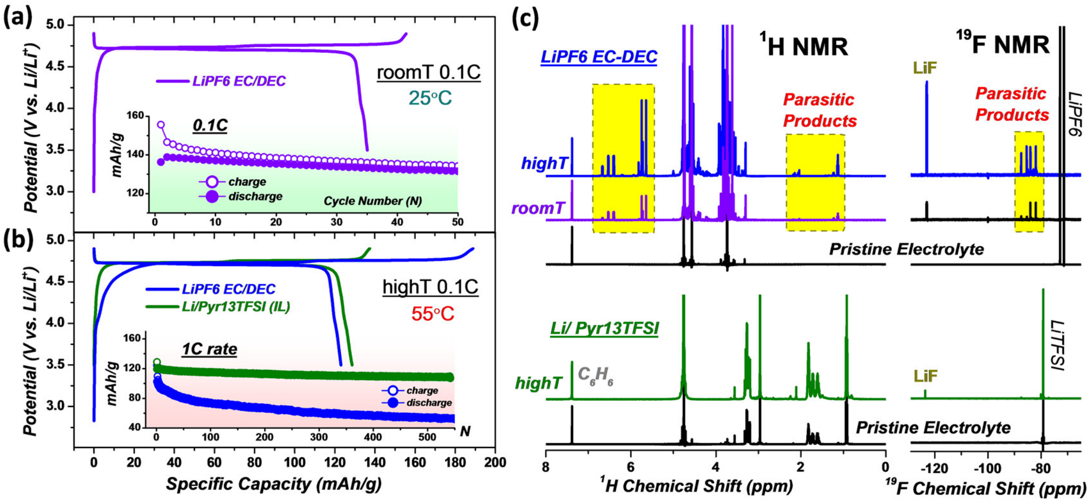

Figure 7. Electrochemical behaviors and NMR analysis of cathodic half-cell (5 V-class $LiNi_{0.5}Mn_{1.5}O_4$ (LNMO) || Li) assembled with different electrolytes at room/elevated temperature. Initial charge-discharge profiles collected: (a) at room T (25°C) in carbonate-based electrolyte ($LiPF_6$/EC-DEC); (b) at elevated T (55°C) in $LiPF_6$/EC-DEC (blue trace) and ionic liquid (IL)-based electrolyte ($LiTFSI/Pyr_{13}TFSI$, green trace). Cycle life of each cells are shown inset, in which IL-based electrolyte system demonstrates superior long term cycling

stability at elevated T. (c) ^{1}H and ^{19}F NMR spectra of D_2O-extracted components from cycled LNMO electrodes and electrolytes. The spectra of corresponding pristine electrolytes are shown on the bottom (black traces). By normalizing the peak of C_6H_6 inner standard, the degradation products are quantitatively estimated. The decomposition of carbonate-based electrolyte can be clearly observed, which is severely deteriorated at elevated T. While, IL perform high stability at harsh working environment (high working voltage and elevated T).

For the LNMO || Li half-cells assembled with conventional $LiPF_6$/carbonate-based (EC-DEC) electrolyte, relatively stable cycling performance can be obtained at room temperature (Figure 7a). The obvious irreversible capacity during initial several cycles can be rationally assigned to the oxidative decomposition of electrolyte. Once a stable cathodic-electrolyte-interface (CEI) film has been formed, the irreversible gap between charging/discharging would be healed upon subsequent cycles. However, turning to an elevated temperature (blue trace, Figure 7b), severe irreversible capacity can be observed (~67 mAh/g) during 1st cycle at 0.1 C rate, and related cell also suffers from rapid capacity deterioration at 1 C rate. Based on the NMR spectra collected after 50 cycles (Figure 7c), more parasitic products can be observed at elevated temperature, which indicates that both electrochemical and thermodynamic decomposition have been largely aggravated.[6, 20-21, 24, 64]

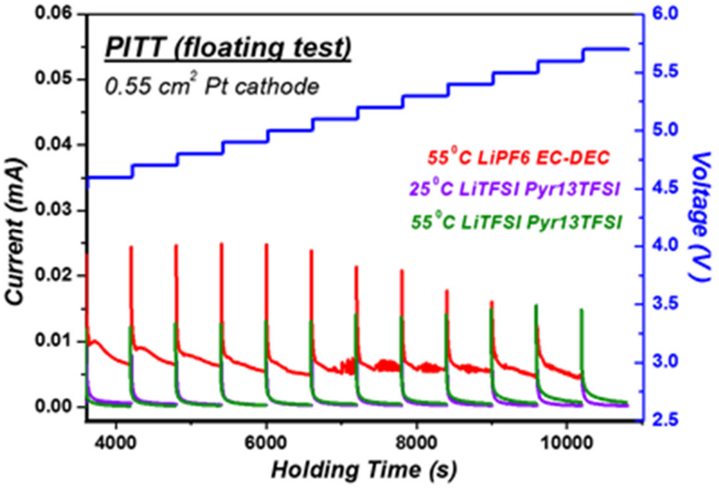

Figure 8. Electrochemical oxidative and thermal stability assessments of different electrolyte systems: typical $LiPF_6$/EC-DEC (carbonates) and ionic liquid-based LiTFSI/Pyr_{13}TFSI. The

specific current have been collected during constant potential intermittent titration (PITT, with 100 mV step). The floating current can be obviously observed in $LiPF_6$/EC-DEC electrolyte at temperature. While, in ionic liquid-based electrolyte, the current cannot be clearly observed at both room and elevated temperature conditions. In this case, the superior electrochemical oxidative and thermal stability of LiTFSI/Pyr_{13}TFSI electrolyte make it a very suitable candidate for the application of high-voltage cathode (5 V-class LNMO system) at elevated temperature (55°C).

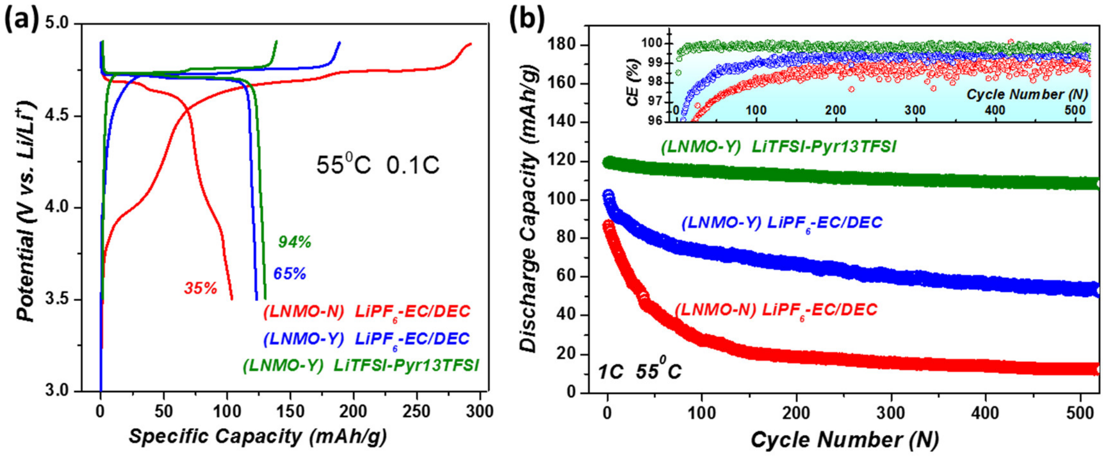

Figure 9. (a) Galvanostatic charge/discharge curves of LNMO half-cell (cycling at 0.1 C low current rate and elevated temperature) assembled with different electrode-electrolyte combinations: normal-LNMO with $LiPF_6$/EC-DEC (red traces); yolk-LNMO with $LiPF_6$/EC-DEC (blue traces); yolk-LNMO with LiTFSI/Pyr_{13}TFSI (green traces). (b) Discharge capacity hysteresis against cycle number harvested at high current rate (1 C rate). Corresponding coulombic efficiency (CE%) have also shown for clarity.

As a comparison, ionic liquid (IL)-based electrolyte (LiTFSI/Pyr_{13}TFSI) exhibits superior thermal stability (Figure 8), and holds a stable long-term cycle life for LNMO half-cell at elevated temperature (green trace, Figure 7b).[65-67] Both the trace amount of decomposition products (green trace, Figure 7c) and remarkably high coulombic efficiency (CE%, Figure 9-10) demonstrate the stability of IL-based electrolyte against the current harsh cathodic environment (high-voltage and high-temperature). As shown in Figure 9, compared with yolk-structured LNMO, normal-LNMO, with typically

Mn^{3+}-involved redox behavior, delivers serious initial capacity loss and presents rapid capacity deterioration during cycling at elevated temperature (55°C). More importantly, although replaced by modified yolk-LNMO (restrain Mn^{3+} concentration), the cell assembled with LiPF6/carbonates electrolyte (blue traces) still suffer from obvious initial capacity loss and capacity degradation. Once change the electrolyte into ionic liquid (green traces), less initial capacity loss and higher capacity retention rate can be achieved, which would be rationally ascribed to the superior oxidative and thermal stability of electrolyte. Besides, the CE% in ionic liquid electrolyte rapidly climbs up and well stabilized at a very high level. In a word, the electrolyte issue is the most important one during modification and optimization on high-voltage cathode employed Li-ion battery systems.

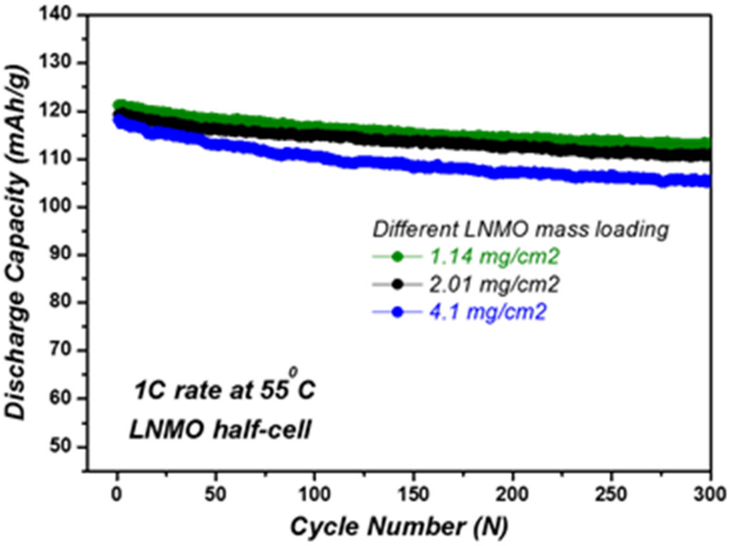

Figure 10. The electrochemical performance of LNMO cathode with different mass loading.

As shown in Figure 10, for the cycling performance, there presents not obvious difference between the cells assembled with 1.14 and 2.01 mg/cm^2 LNMO. Once the mass loading increase to 4.1 mg/cm^2, there presents a slight decrease of specific capacity for the LNMO cathode. In order to provide a relative fair electrochemical data, we chose the 2.0 mg/cm^2 mass loading as the optimal value, which would both take care of the cycle life/retention and practical issue (requiring the mass loading as large as possible).

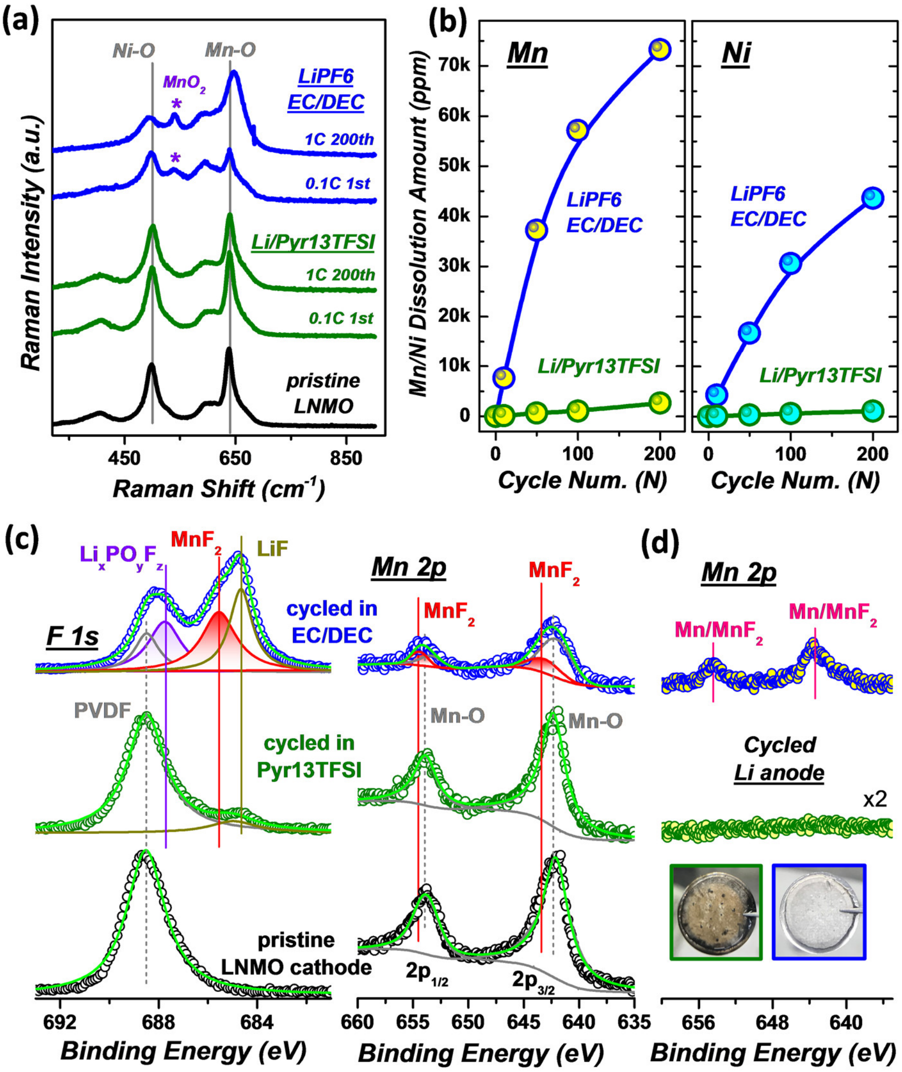

Figure 11. Spectroscopic analysis of the deterioration mechanism of LNMO || Li half-cell at elevated temperature. (a) Raman spectra of the cycled LNMO cathodes collected from different electrolyte systems. Compared with the well-preserved spectra harvested from IL-based electrolyte system (green traces), the peak distortion and new-produced MnO_2-related signals indicate the obvious structural deterioration of LNMO electrode cycled in typical $LiPF_6$/EC-DEC electrolyte (blue traces). (b) Mn and Ni dissolution amount collected from cycled cells assembled with different electrolytes. Notably, the information of both the dissolved (in electrolyte) and re-deposited (on Li anode) parts have been collected for ICP characterizations. Compared with the IL-based condition, the detrimental loss of transition-metal is substantially aggravated in $LiPF_6$/EC-DEC. (c) XPS spectral region for F 1s and Mn 2p collected from LNMO cathodes cycling in different electrolytes. The parasitic products derived from $LiPF_6$ degradation ($Li_xPO_yF_z$ and LiF) and HF corrosion (MnF_2) are accumulated

on LNMO cathode surface within $LiPF_6$/EC-DEC condition (upper blue dots), which are absence in IL-fabricated cell (middle green dots). (d) Mn 2p XPS spectra collected from corresponding Li foil anodes. Compared with the Mn-free Li foil surface harvested from IL-fabricated cell, the observation of Mn-related components on cycled Li anode surface further exemplify the migration and re-deposition of dissolved Mn from the LNMO cathode in $LiPF_6$/EC-DEC system. The photos of cycled Li anodes also visualize the transition-metal migration phenomenon in LNMO || Li half-cell.

Comprehensive analysis on degradation mechanism are extended in Figure 11. Compared with the Raman spectrum collected from pristine LNMO (black trace, Figure 11a), cathode do not present obvious change after cycled within IL-based electrolyte at elevated temperature. While, on the cathode obtained from $LiPF_6$/EC-DEC electrolyte system, newly-produced MnO_2 and distinct spectral distortion can be clearly observed (Figure 11a and Figure 12).[10]

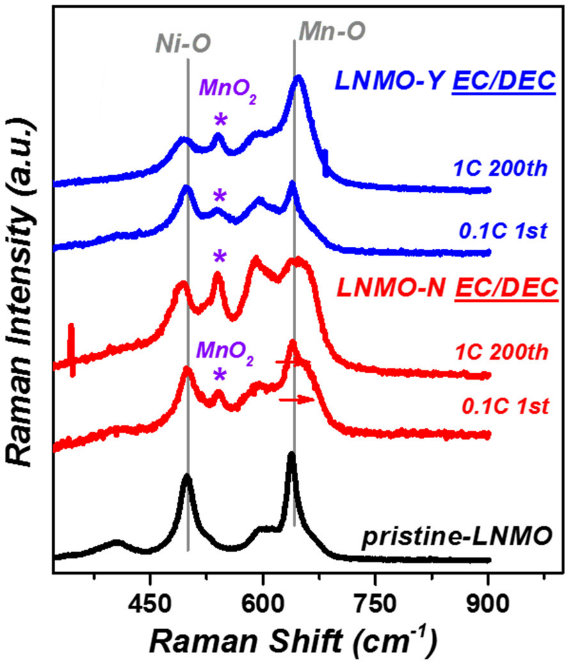

Figure 12. Raman spectra collected from the LNMO cathodes collected from corresponding half-cells cycled at elevated temperature (discharged states cycled in LiPF6/EC-DEC electrolyte system): normal-LNMO cathode (red traces); yolk-structured LNMO cathode (blue traces).

Compared with the LNMO cathodes obtained from LiTFS/Pyr13TFSI-related system (shown in Figure 2a, green traces), the cells cycled in $LiPF_6$/EC-DEC system suffer from serious structural distortion and new phase formation (MnO_2). Based on related reports,[10, 13] the reaction mechanism can be summarized as follows:

$$LiPF \rightarrow LiF + PF_5;\ PF_5 + H_2O \rightarrow OPF_3 + 2HF;\ OPF_3 + 3H_2O \rightarrow PO_4H_3 + HF$$

$$4LiNi_{0.5}Mn_{1.5}O_4 + 8H^+ \rightarrow MnO_2 + Mn^{2+} + Ni^{2+} + 4Li^+ + 4H_2O + 2Ni_{0.5}Mn_{1.5}O_4.$$

This can be attributed to the hydrofluoric acid (HF)-related chemical corrosion, which produced from decomposition of $LiPF_6$.[13] Simultaneously, the corrosion leads to pronounced Mn/Ni dissolution, which is well exemplified by the ICP results collected from cycled electrolyte and Li anode surface (blue dots, Figure 11b). Compared with the Mn/Ni dissolution amount record at room temperature (~0.25% of total LNMO cathode after 50 cycles, Figure 13), the huge amount of Mn/Ni loss (surpass 7% of total LNMO cathode after 200 cycles) derived from HF corrosion re-proves the poor thermal stability of $LiPF_6$.[13, 68]

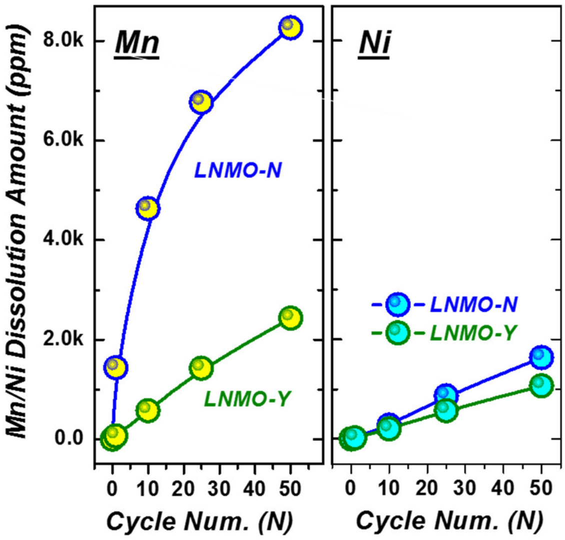

Figure 13. Metal dissolution (Mn and Ni) information collected during cycling at room temperature in LNMO-based half-cells (blue dots: normal-LNMO; green dots: yolk-structured LNMO) assembled with $LiPF_6$/EC-DEC electrolyte.

Compared with the ICP-OES results collected at elevated temperature (Figure 11b), the metal dissolution has been significantly mitigated in moderate room temperature condition. In yolk-structured LNMO, there present not obvious difference between dissolution amounts of Ni and Mn, which also indicate that the loss of active material may be ascribed to the corrosion of HF (derived from $LiPF_6$ decomposition).[13, 16, 20] However, due to the higher Mn^{3+} concentration within the disordered normal-LNMO cathode, the Mn-dissolution delivers more serious than Ni. The difference between the two LNMO samples exemplify the optimization of LNMO cathode by morphology and annealing-condition modifications. Moreover, the accumulation of both decomposition products and dissolved metal-ion can be clearly illustrated by XPS spectra harvested from cycled LNMO cathodes (Figure 11c). Consistent with the information collected from electrolyte and anode, the characterization peaks of LiF, MnF_2 and $Li_xPO_yF_z$ components can be clearly observed on the surface of LNMO cathodes cycled in $LiPF_6$/EC-DEC system.[17, 69]

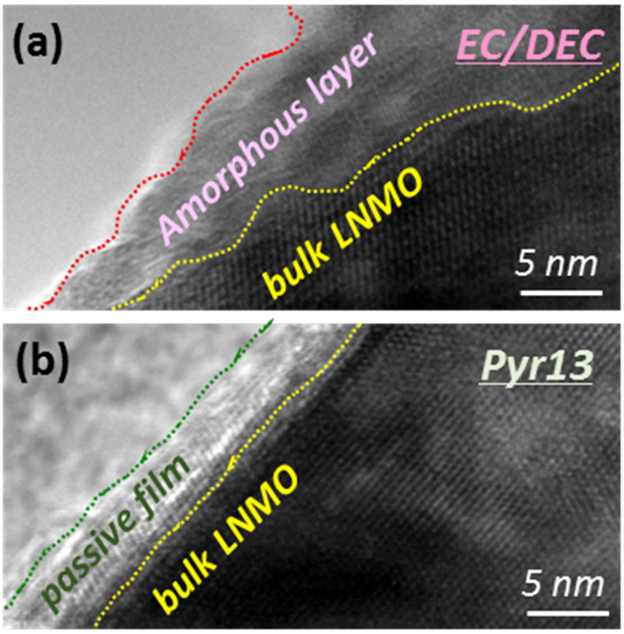

Figure 14. HR-TEM images of LNMO cathode cycled in different electrolytes at elevated temperature (after 1st charge/discharge cycle at 0.1 C rate): (a) typical $LiPF_6$/EC-DEC electrolyte; (b) LiTFSI/Pyr_{13}TFSI ionic liquid-based electrolyte.

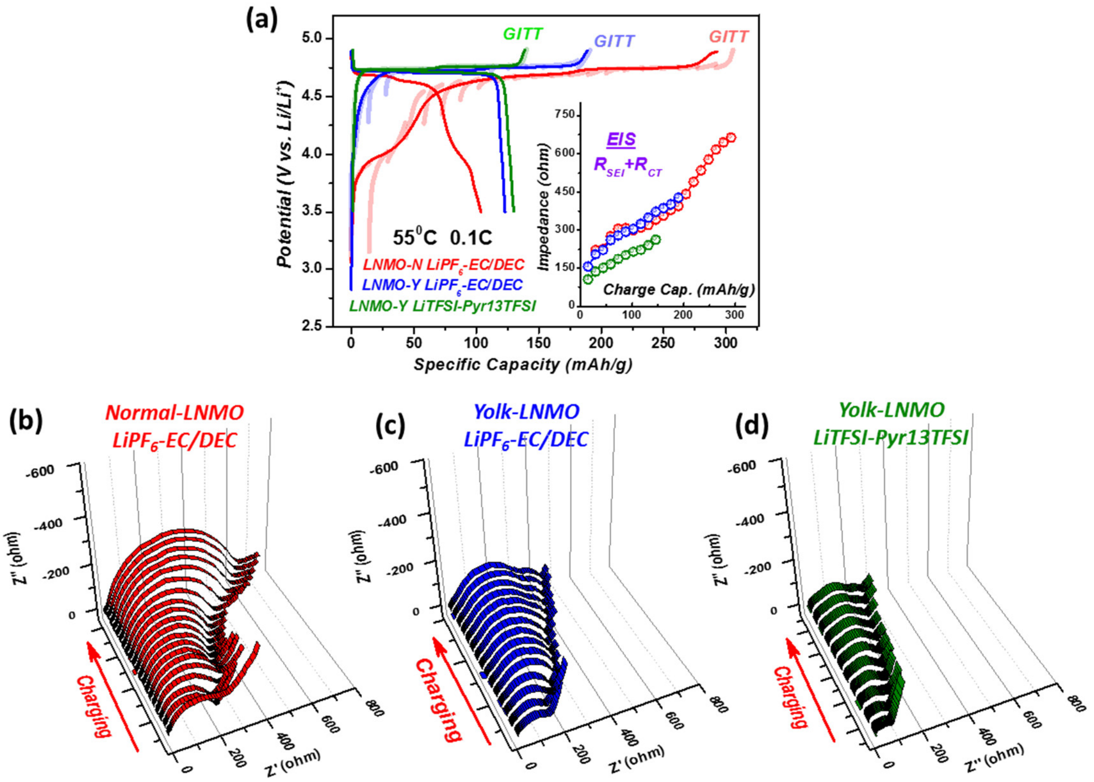

Figure 15. Corresponding EIS results collected during GITT treatment on the cells assembled with different electrode/electrolyte combinations at elevated temperature: normal-LNMO with $LiPF_6$/EC-DEC (red traces); yolk-LNMO with $LiPF_6$/EC-DEC (blue traces); yolk-LNMO with LiTFSI/Pyr_{13}TFSI (green traces). The impedance evolution (R_{SEI}+R_{CT}) of aging cells (during GITT charging) are summarized inset for clarity.

Compared with the ionic liquid electrolyte (green traces), the Nyquist plot clearly demonstrate that the cells fabricated with $LiPF_6$/EC-DEC electrolyte (red and blue traces) deliver higher resistance. This is also well consistent with the spectroscopy (Raman, XPS, ICP-OES) and image (SEM) evidences, which prove the serious degradation of electrode and electrolyte in $LiPF_6$/EC-DEC condition.

Compared with the homogeneous thin CEI film formed in Li/Pyr_{13}TFSI condition, there presents thick heterogeneous layer deposited on the LNMO cathode cycled in $LiPF_6$/EC-DEC electrolyte. The components of the thick CEI film (herein, can be regarded as a deposition of parasitic reaction products) have been further proved by XPS (Figure 11c) and Raman (Figure 11a) analysis in the main text: MnO_2, MnF_2, LiF, and $Li_xPO_yF_z$, etc. The thicker surface deposited film would inevitably lead to higher surface resistance, which further proved by the EIS result revealed in the following sections. Furthermore, the continuously growing of inhomogeneous CEI film on cathode surface inevitably lead to the increasing of resistance impedance, which also exacerbates the capacity degeneration (Figure 14-17).[20] In sharp contrast, trace amount of metal loss and homogeneous LiF-dominated CEI film can be obtained in IL-based electrolyte system.

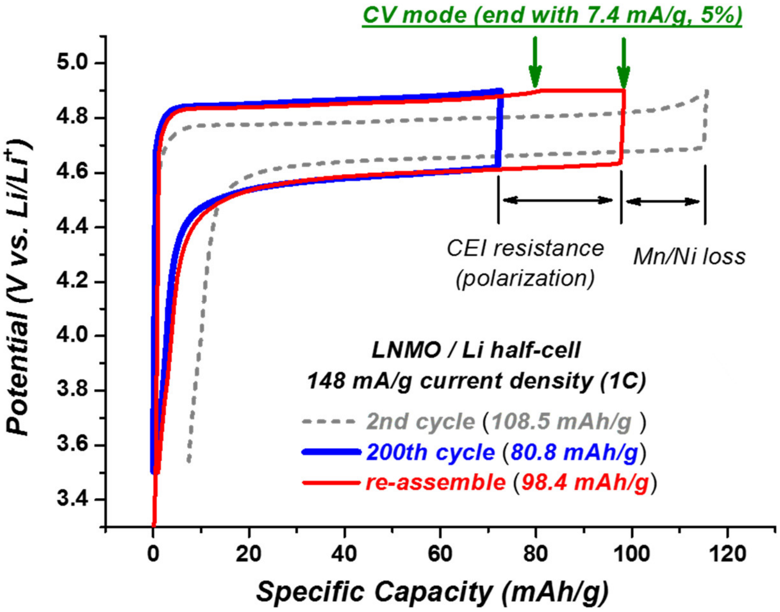

Figure 16. An additional electrochemical treatment on the cycled LNMO || Li half-cell (1 C rate at elevated temperature in $LiPF_6$/EC-DEC electrolyte). The final target is to further analysis the influence of both resistance and metal-dissolution towards capacity loss. After 200 cycles (blue trace), the LNMO cathode was extracted and re-assembled into a new half-cell. After galvanostatic charging (CC mode) to the cut-off voltage (4.9 V vs. Li/Li^+), the cell was continuously keeping at 4.9 V (CV mode) until the current density drop to 5% (7.4 mA/g) of initial charging current rate (1C, 148 mA/g). Then the cell was discharged to 2.0 V.

Herein, the loss of capacity can be mainly ascribed to two reasons: 1) Ni/Mn dissolution (proved by GITT); 2) increasing of resistance (proved by EIS). After 200 cycles, the discharge capacity drops to 80.8 mAh/g (~74.5% retention), however, based on ICP-OES, the amount of Ni/Mn loss accounts for nearly 7.5% of total active material. In this case, the increasing of resistance can be regarded as another importance factor, which leads to the capacity deterioration. In this case, after holding at 4.9 V during additional CV mode (red traces), the capacity loss assigned to resistance would be recovered, and corresponding additional amount of capacity can be obtained during the subsequent discharging process.

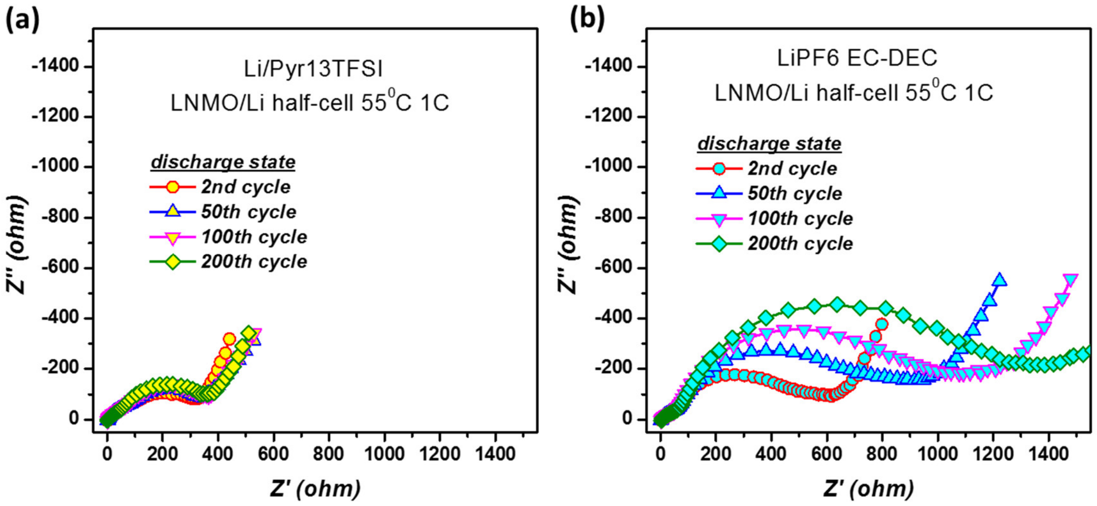

Figure 17. Nyquist plot showing the impedance evolution of discharged LNMO || Li half-cells cycled within different electrolyte conditions (at elevated temperature): (a) LiTFSI/Pyr$_{13}$TFSI; (b) LiPF$_6$/EC-DEC.

The stabilized resistance observed in ionic liquid electrolyte indicate the formation of stable CEI film on the LNMO cathode. While, in LiPF$_6$/carbonates, the increasing resistance during cycling exhibits well coincide with the continuous accumulation of parasitic products derived from related electrolyte decomposition.

Besides, different from the clean Li surface collected from IL-based system, the deposition of dissolved metal-ion and deposition products can also be clearly observed on the Li foil anode surface after cycled in LiPF$_6$/EC-DEC (Figure 11d and Figure 18-19). In a practical full-cell system, the dissolution-crossover-deposition of metal-ions (Mn^{2+} and Ni^{2+}) would reduce the active-Li$^+$ within anode (react with LiC$_6$ on Li-intercalated graphite anode). The consumption of the limited active-Li$^+$ reveals to be very harmful for full-cell operation, which is often neglected in half-cell system.[4, 6, 13] As a comparison, such a detrimental chemical shuttling can be effectively restrained by the employment of IL-based electrolyte. Moreover, electrolyte decomposition-induced gas evolution and electrode exfoliation would also be controlled at elevated temperature (Figure 20-21). Consequently, owing to its high cathodic compatibility and stability, LiTFSI/Pyr$_{13}$TFSI IL-based electrolyte can be employed as a superior candidate for high-voltage cathodic reaction, especially at elevated temperature.

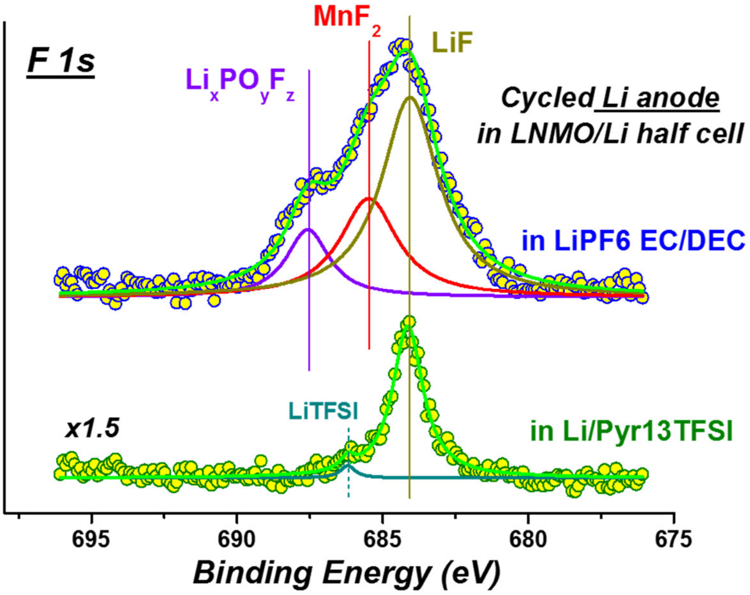

Figure 18. XPS spectra (F 1s region) collected from the cycled Li anode harvested form the LNMO || Li half-cell. Similar with the related Mn 2p region revealed in Figure 11d, the deposition of electrolyte decomposition products (LiF, MnF_2, $Li_xPO_yF_z$, etc.) can be clearly observed on the Li anode cycled in $LiPF_6$/carbonates electrolyte. While, within the cell assembled with ionic liquid electrolyte, merely trace amount of LiF can be detected.

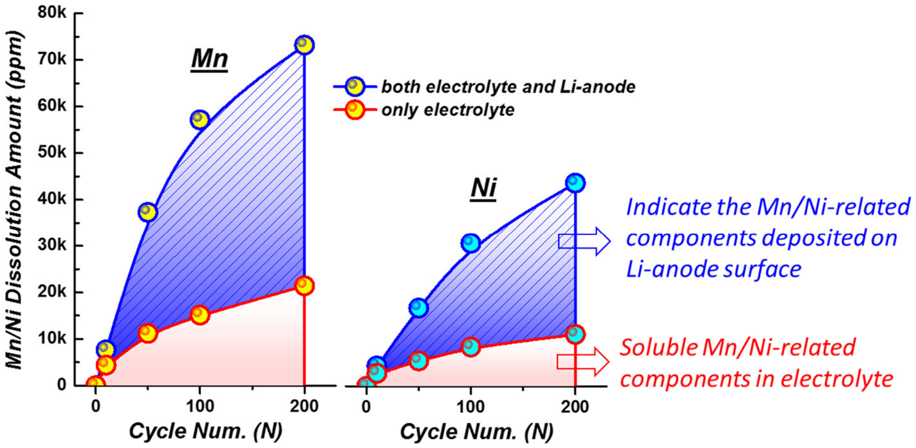

Figure 19. ICP-OES results collected from the cycled LNMO Li half-cells. The results can be employed to quantitatively analysis the amount of Ni/Mn dissolution during cycling.

Herein, an important issues should be clarified for the extract process. In order to collect the total amount of dissolved metal-ions from the LNMO cathode, both the ones dissolved in cycled electrolyte and the deposition part onto the Li anode side should be carefully extracted for ICP test. In this case, as detailed interpreted in Experimental Section, the dissolved part (in electrolyte) has been harvested from separator by DMC-rinsing (highlighted by red dots). While the total amount (electrolyte dissolved + anode deposited) of lost Ni/Mn can be obtained by a DMC+acid-rinsing for both separator and Li anode (marked by blue dots). In this case, we can prove that large amount of dissolved Ni/Mn suffer from a "dissolution-migration-deposition" process, and finally deposition on anode surface. This shuttling effect would be very detrimental for anode, especially for half-cell system assembled with limited amount of active-Li^+ stored in cathode materials.[13-14, 70]

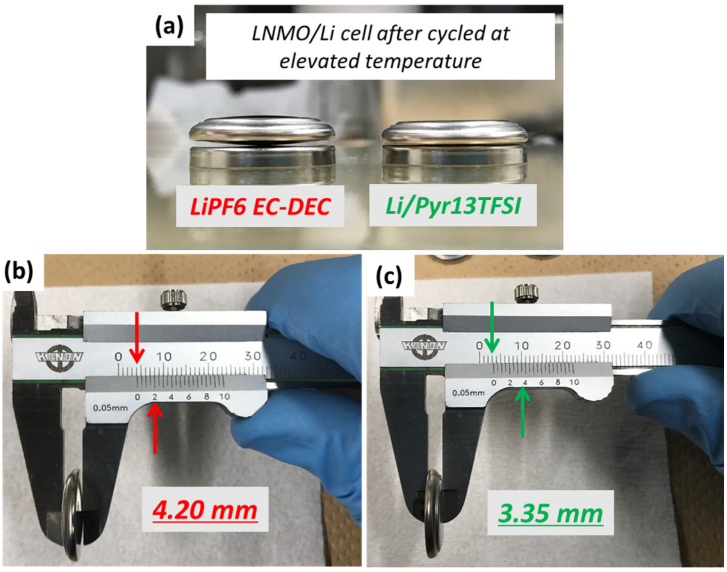

Figure 20. The volume variation and photos of the LNMO || Li coin-cells after cycling at elevated temperature. The cells are assembled with different electrolyte: $LiPF_6$/EC-DEC (left) and LiTFSI/Pyr_{13}TFSI (right), respectively.

Obviously, the cell assembled with conventional $LiPF_6$/carbonates electrolytes suffers from seriously gas inflation. While the cell assembled with ionic liquid do not present obvious volume change after 200 cycles. The evolution of gas should be attributed to the decomposition of electrolyte and related harmful influences. The mechanism of gas releasement can be summarized by previous classic reports:[13, 15]

$C_3H_4O_3 + 2Li^+ + 2e^- \rightarrow Li_2CO_3 + C_2H_4$;

$2C_3H_4O_3 + 2Li^+ + 2e^- \rightarrow (CH_2OCO_2Li)_2 + C_2H_4$;

$C_4H_8O_3 \rightarrow CH_3CH_2OCH_3+ + 2e^- + CO_2$;

DEC → $EtOH + CO_2 + C_2H_4$ (catalyzed by produced MnO_2 catalyst);

DEC + $PF_5 \rightarrow C_2H_5OCOOPF_4 + C_2H_4 + HF$; (derived from $LiPF_6$ decomposition)

$C_2H_5OCOOPF_4 \rightarrow PF_3O + CO_2 + C_2H_4 + HF$;

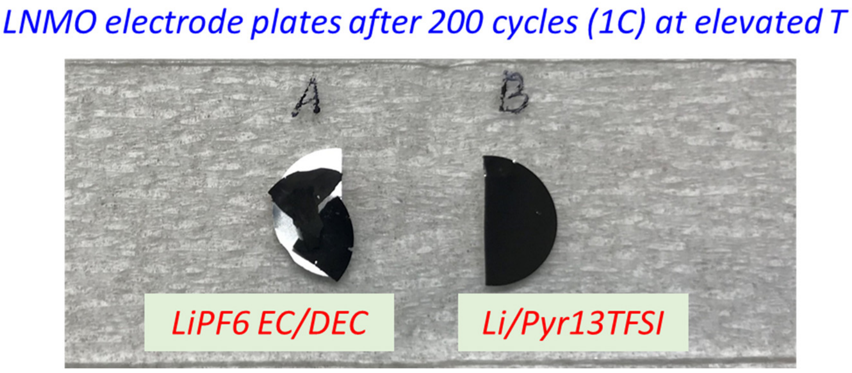
LNMO electrode plates after 200 cycles (1C) at elevated T

Figure 21. Photographs of cycled LNMO cathode plateaus (cut into half pieces) harvested from the LNMO Li half-cell after 200 cycles (1 C rate) at elevated temperature within different electrolyte conditions: $LiPF_6$/EC-DEC (left) and LiTFSI/Pyr_{13}TFSI (right), respectively.

After cycling in typical $LiPF_6$/carbonates electrolyte system, there presents obvious peel off phenomenon between LNMO layer and Al-foil current collector. The loss of binder adhesion would be rationally ascribed to several probable reasons: HF-related attack towards Al-foil current collector; Mn/Ni loss leads to the poor interface contact; etc.[4, 6, 20-21] Undoubtedly, the delamination of current collector and LNMO active material would lead to poor electrical contact, resulting in severe increasing of interface electrical resistance and polarization. This is also well fit with the related EIS results revealed above.

3.2.2 Choosing a competent anolyte for reversible Li-GIC at elevated temperature

Naturally, LiTFSI/Pyr_{13}TFSI IL-based electrolyte could be directly introduced into a LNMO || graphite full-cell system, however, the reversible cycling cannot simply be achieved as predicted, which is unexpectedly mismatch with the excellent cycliability in corresponding LNMO || Li half-cell. The main problem focus on the huge irreversible capacity loss (~85 mAh/g) during the 1^{st} cycle at both room and elevated temperatures (Figure 22a and Figure 23). Further electrochemical characterization (Figure 24) and half-cell performance eliminate the suspicion of LNMO cathode, which indicates the irreversible capacity may be ascribed to the improper graphite-intercalation-chemistry (GIC) on the anode.

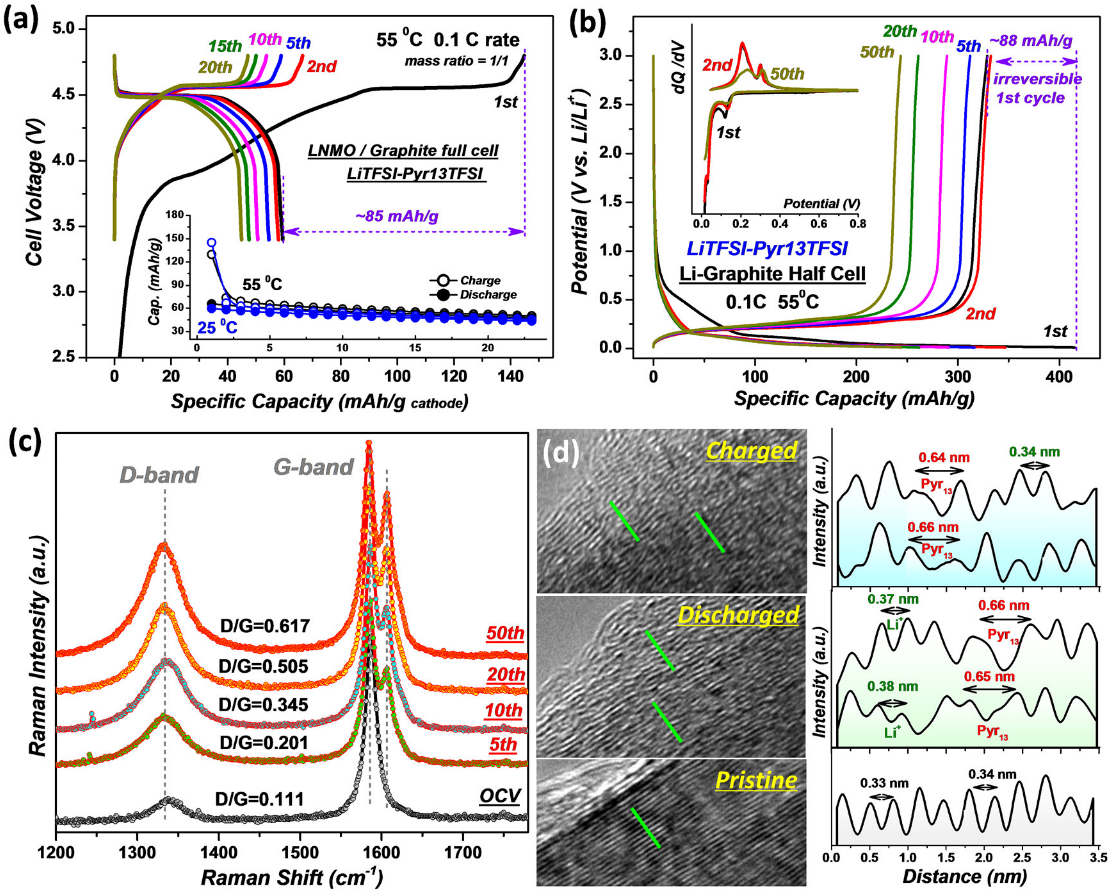

Figure 22. The failure mechanism of IL-fabricated LNMO || graphite full-cell under elevated temperature: an irreversible graphite-intercalation-chemistry (GIC) on anode side. (a) Voltage profiles of the full-cell assembled with IL-based (LiTFSI/Pyr_{13}TFSI) electrolyte cycling at 55°C. Inset presents the corresponding charge/discharge capacity

hysteresis against cycle number harvested at 25°C and 55°C, respectively. A serious irreversible capacity loss can be observed during the 1st cycle. (b) Voltage profiles of the graphite || Li half-cell assembled with LiTFSI/Pyr$_{13}$TFSI electrolyte cycling at 55°C. Similar initial irreversible capacity loss can be observed. The distortion of dQ/dV curves are also revealed inset. (c) Raman spectra of discharged (de-intercalated state) graphite || Li half-cells during cycling. The exacerbated splitting of G-band and growing trend of G-band indicate the irreversible residual of intercalated compound and disordered deterioration of graphitic layer. (d) HR-TEM images and corresponding lattice distances of cycled graphite extracted from graphite || Li half-cells. The abnormal large expansion of graphitic lattice distances (~0.65 nm) observed at discharged (intercalated) state indicate the co-intercalation of IL (Pyr$_{13}^+$ cation), which cannot reversibly de-intercalate after charging. In this case, the irreversible co-intercalation of IL within the graphite anode leads to the irreversible capacity loss of the LNMO || graphite full-cell assembled with IL-based electrolyte.

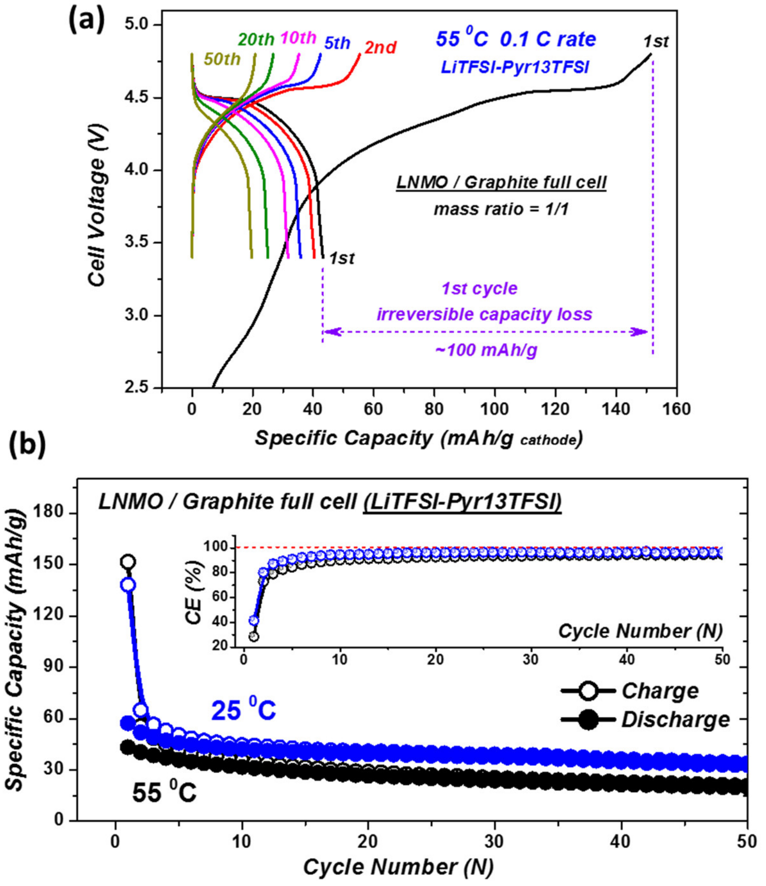

Figure 23. Typical galvanostatic charge/discharge curves (a) and corresponding charge/discharge capacity hysteresis against cycle number (b) harvested from the cell assembled with normal-LNMO (disordered) || graphite full-cells. Similar with the one observed in yolk-structured LNMO-assembled cell (Figure 3a), both of the full-cells fabricated by LiTFSI/Pyr$_{13}$TFSI electrolyte suffer from serious initial capacity loss at room/elevated temperature. In this case, changing the LNMO cathode cannot restrain the related capacity loss, and the core issue should be focus on the anode side (irreversible Pyr$_{13}^{+}$-related co-intercalation into graphite anode revealed in Figure 22).

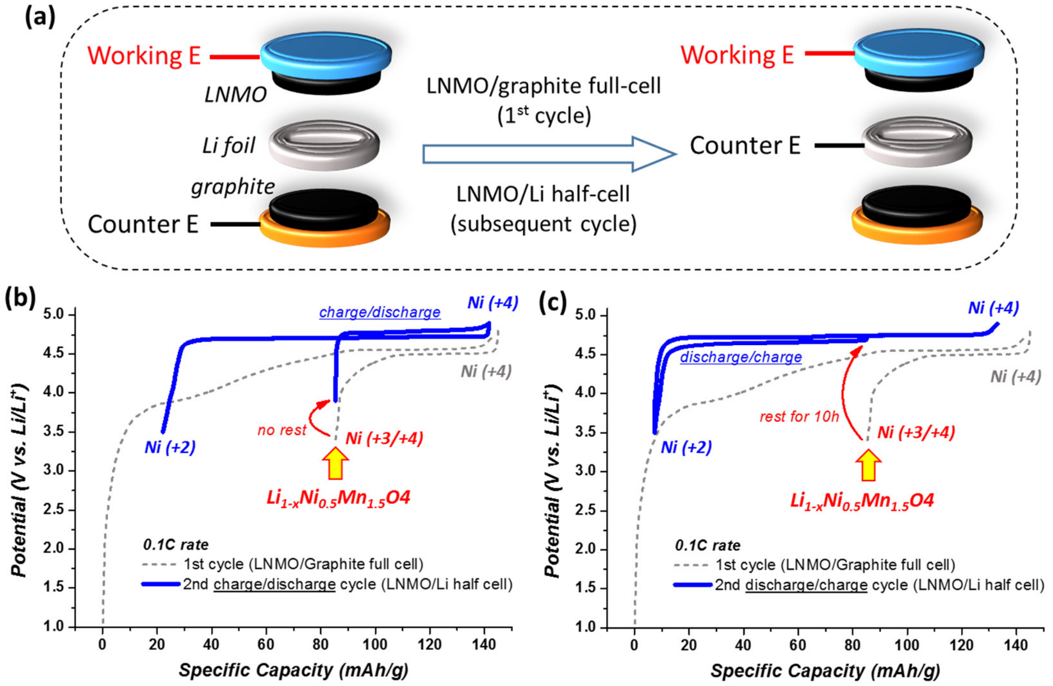

Figure 24. Additional electrochemical treatment to clarify the reason for initial capacity loss observed in LNMO graphite full-cell assembled with LiTFSI/Pyr$_{13}$TFSI electrolyte. (a) Illustration of the specific-designed cell structure. Assembled with a three-electrodes cell, during 1st full-cell cycling, the cell was operated by a dual-electrodes mode (LNMO/graphite). Then, during the subsequent cycle, the graphite anode was abandoned (disconnected), and another Li foil was connected as a newly-assembled LNMO || Li half-cell system. This design can be employed to analysis the state of LNMO cathode during the 1st full-cell cycle. (b) 2nd charge/discharge and (c) 2nd discharge/charge curves of the LNMO || Li half-cell.

As a results, after the 1st full-cell cycling, the LNMO cathode cannot be fully recovered to its original state (Li-intercalated state), which indicates that there is not enough active-Li^+ being provided to LNMO cathode during 1st discharging process. This is also well consistent with the irreversible Li-GIC process (Pyr_{13}^+-related irreversible co-intercalation) observed on graphite anode in LiTFSI/Pyr_{13}TFSI electrolyte. The initial capacity loss in full-cell can be ascribed to a Li-GIC anode-related issue (not LNMO).

In order to unravelling the anodic electrochemistry, Li-GIC process is separately investigated in graphite || Li half-cell system. In LiTFSI/Pyr_{13}TFSI electrolyte system, distinct discharge/charge capacity gap during initial cycle and subsequent capacity deterioration clearly indicate an irreversible GIC process (Figure 22b), which also well coincide with the severe initial capacity loss revealed in full-cell system.[38, 42] Figure 22c presents the Raman spectra collected from the cycled graphite || Li half-cells. Typically, during cycling, the splitting/recovering of G-band (a sharp band around 1580 cm^{-1}, crystalline graphite E_{2g} mode) can be ascribed to the reversible formation/decomposition of stage intercalation compounds.[71-72] However, the residual splitting feature observed on discharged graphite electrodes (Li^+ de-intercalated state) strongly indicate irreversible de-intercalation processes, after which there are certain amount of cation residues trapped within the graphite matrix. Besides, the growing trend of D-band (a broad band around 1345 cm^{-1}, disordered finite crystalline A_{1g} mode) during cycling provides clear indication for the aggravated formation of irreversible damage/defects within graphite structure.[73] More visual evidence is illustrated by the distortion of lattice fringe shown in HR-TEM images (Figure 22d). Compared with the well-ordered lattice fringe within pristine graphite electrode (~0.33 nm interlayer distance), there deliver two kinds of expanded interlayer distances within the discharged graphene layers (cation intercalated state): ~0.37 nm (a traditional Li^+ intercalated feature) and ~0.65 nm (an abnormally large distance expanded by huge cation in IL, Pyr_{13}^+).[74] After charging, although Li-ions can successfully de-intercalate, the co-intercalated Pyr_{13}^+ cannot fluently get out of the interlayers. Furthermore, the co-intercalation of huge cation would inevitably induce the destruction of ordered interlayer structure and bulk phase exfoliation (Figure 25).[75-76]

The HR-TEM results are well consistent with the Raman observations, which clearly demonstrate the harmful Pyr_{13}^+ co-intercalation. Turning back to the full-cell system, because of the limited active-Li^+ source derived from LNMO cathode, the co-intercalation of Pyr_{13}^+ in graphite anode would directly lead to the loss of active-Li^+ (de-intercalated from cathode) into electrolyte. What was worse, due to the irreversible de-intercalation of Pyr_{13}^+ (from graphite anode), this portion of active-Li^+ cannot return back to the LNMO surface, which degenerate into inert-Li^+. In another word, the irreversible trapping amount of co-intercalated Pyr_{13}^+ directly determines the irreversible capacity during charging/discharging in LNMO graphite full-cell assembled with LiTFSI-Pyr_{13}TFSI electrolyte. In this case, unfortunately, although owing to a high compatibility with high-voltage cathodic reaction, LiTFSI-Pyr_{13}TFSI cannot be employed for the LNMO || graphite full-cell operation due to the irreversible anodic behavior.

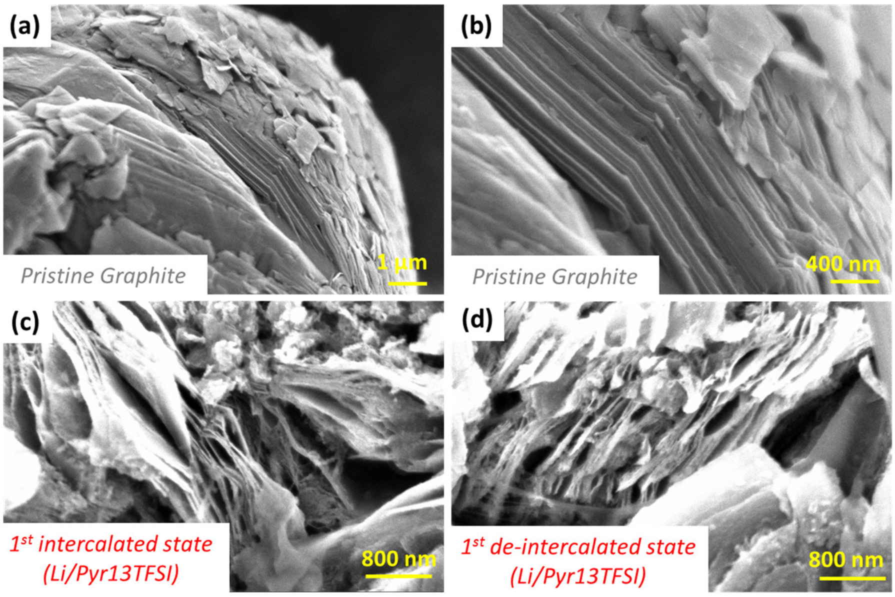

Figure 25. SEM images of (a and b) pristine graphite particle; (c and d) graphite electrodes collected from graphite || Li half-cells assembled with LiTFSI/Pyr_{13}TFSI electrolyte: after discharging (c) and charging (d), respectively.

Serious irreversible exfoliation and layered swelling can be clearly observed during Li-GIC in LiTFSI/Pyr$_{13}$TFSI electrolyte. This morphological degradation presents well coincide with the structural collapse unraveled by Raman and HR-TEM results shown in Figure 22. The co-intercalation of Pyr$_{13}^{+}$ would inevitably exacerbate the interlayer stress and lead to the structural distortion.

Then, the following target is finding a compatible electrolyte system for reversible Li-GIC process, and can be qualified as an anolyte candidate for the hybrid-electrolytes design strategy (introduce in the next section). Benefitting from its aggregated solvent structure, super-concentrated electrolytes have attracted considerable research attention to data, due to their high oxidative/reductive stability, etc.[7, 9, 77-79] Herein, inspired by its specific solvate ionic liquid structure, equimolar LiTFSI/G$_3$ (DEGDME) complex, an ether-based electrolyte has been introduced. Different from the diluted electrolyte composed by solvent-separated-ion-pair (SSIP), this free-style solvation state has been replaced by an aggregated contact-ion-pair (CIP) mode in equimolar LiTFSI/G$_3$ complex.[77, 80-81]

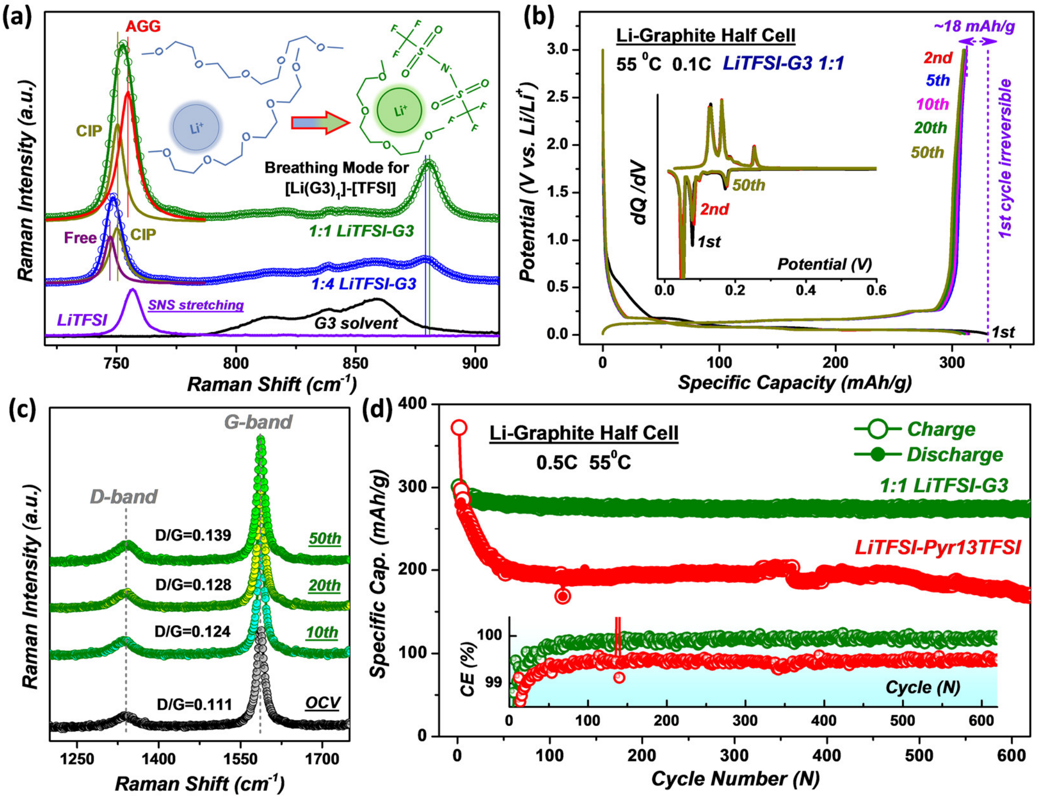

Figure 26. Reversible Li-GIC behavior in highly-solvated LiTFSI/G_3 equimolar complex electrolyte at elevated temperature. (a) Raman spectra of varying LiTFSI/G_3 solutions. The SNS stretch region in $TFSI^-$ are fitted by Gaussian-Lorentzian distribution functions. Different from the typical diluted electrolyte solution (1:4 mole ratio, blue trace), Li^+ are fully sheathed by equimolar amount of G_3 molecule with 1:1 mole ratio (green trace). Solvated $[Li(G_3)]^+$ and $TFSI^-$ are completely aggregated (AGG) within a contact-ion-pair (CIP) fluid network. (b) Voltage profiles of the graphite || Li half-cell fabricated with LiTFSI/G_3 equimolar complex electrolyte cycling at 55°C. The well-preserved galvanostatic and corresponding dQ/dV (inset) curves indicate a good reversibility during Li-GIC. (c) Raman spectra of discharged (de-intercalated state) graphite electrodes. The pristine graphitic structure has been well-maintained during cycling. (d) Charge/discharge capacity hysteresis against cycle number collected from graphite || Li half-cell assembled with different electrolytes: equimolar LiTFSI/G_3 (green trace) and LiTFSI/$Pyr_{13}TFSI$ (red trace). Corresponding coulombic efficiency (CE%) are inset for clarity. Without the severely irreversible initial capacity loss, superior long term cycling stability and higher CE% can be achieved in the newly-introduced equimolar LiTFSI/G_3 electrolyte system.

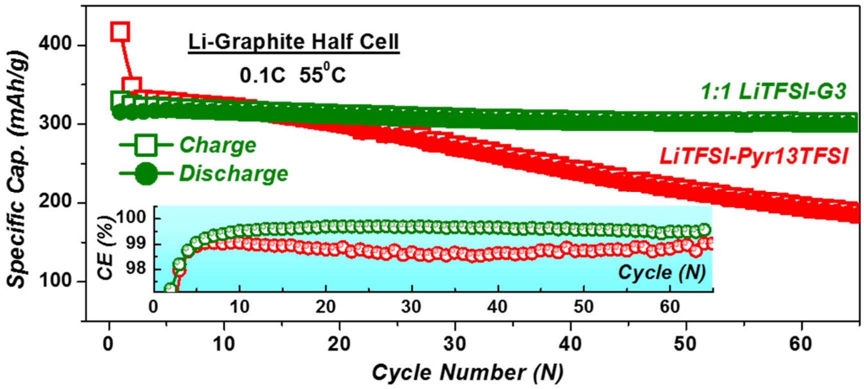

Figure 27. Discharge/charge capacity hysteresis against cycle number harvested from the graphite || Li half-cell assembled with different electrolytes (0.1 C at elevated temperature, 1C = 372 mA/g): LiTFSI/$Pyr_{13}TFSI$ (red traces) and equimolar LiTFSI/G_3 complex (green traces), respectively.

Illustrated by Raman spectroscopy (Figure 26a), the free mode of $TFSI^-$ has been totally restrained, while the interaction between Li^+ and glyme solvent molecule has been largely enhanced. As a result, the evolution of solvent structure essentially changed the de-solvation energy of electrolyte.[81] Therefore, for Li-GIC process, the typical solvent co-intercalation would be suppressed at room temperature. In this study, the graphite || Li half-cell fabricated with this equimolar LiTFSI/G_3 electrolyte is conducted at elevated temperature (Figure 26b).

Encouragingly, tiny initial irreversible capacity loss and superior high CE% can be achieved at 0.1 C rate during Li-GIC (Figure 27). Both the galvanostatic and dQ/dV curves exhibit traditional feature of reversible pure Li^+ de-/intercalation, which can be stably sustained after 50 cycles. Corresponding Raman spectra collected after cycling (de-intercalated states) also prove the structure stability of graphite electrodes cycled in equimolar LiTFSI/G_3 electrolyte (Figure 26c). Moreover, both the reversible variation of lattice fringe and bulk structural integrity are visually demonstrated by HR-TEM and SEM images (Figure 28-29).

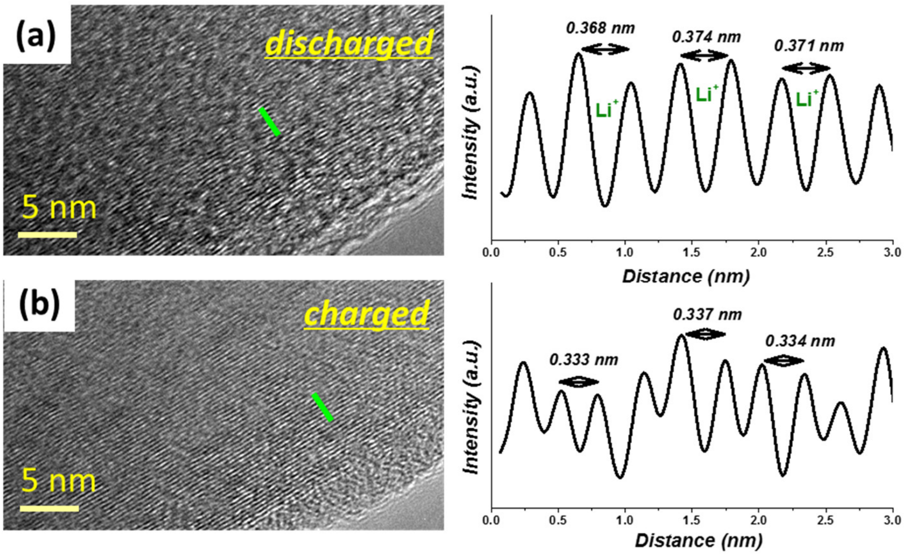

Figure 28. HR-TEM images and corresponding lattice distances of cycled graphite extracted from graphite || Li half-cells assembled with equimolar LiTFSI/G_3 complex electrolyte: (a) after discharging (Li^+ intercalated state); (b) after charging (Li^+ de-intercalated state). The lattice distance around 0.37 nm can be assigned to the typical pure Li^+ intercalated state within graphite layer. The lattice distance basically recover back to its original state (around 0.33 nm) after

charging, which indicates that a reversible Li-GIC process has been achieved in equimolar LiTFSI/G_3 complex electrolyte at elevated temperature.

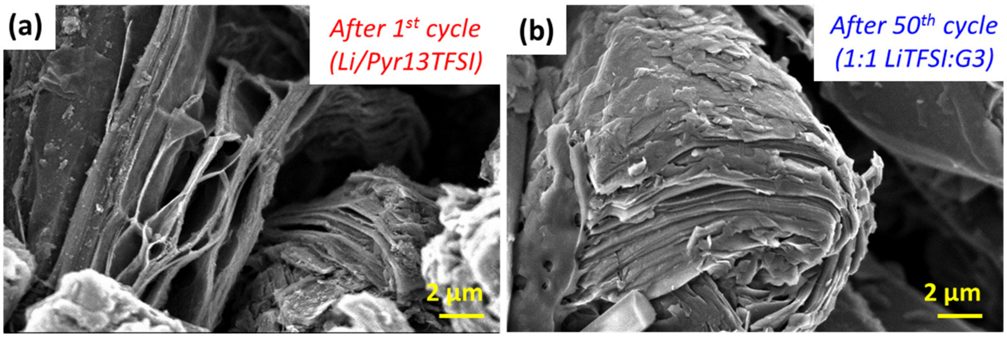

Figure 29. SEM images of cycled graphite electrodes harvested from graphite Li half-cell conducted at elevated temperature and 0.1 C current rate: (a) after the 1st cycle in LiTFSI/Pyr_{13}TFSI electrolyte; (b) after 50 cycles in equimolar LiTFSI/G_3 electrolyte. Different from the serious structural distortion observed after initial cycle in ionic liquid Li-GIC condition, the graphite electrode keeps relatively good condition after 50 cycles in the super-concentrated equimolar LiTFSI/G_3 electrolyte at 55°C, which can be ascribed to the reversible Li-GIC process in this newly-introduced electrolyte system.

Furthermore, comparing with the graphite || Li half-cell performance observed in IL-based electrolyte, not only irreversible initial capacity loss has been controlled, but also outstanding long-term cycling stability can be obtained in equimolar LiTFSI/G_3 electrolyte at elevated temperature cycled with 0.5 C rate. In this case, a suitable anodic electrolyte for high reversible Li-GIC (especially at elevated temperature) has been obtained.

3.2.3 Introduction of MOF-based separator for synergistical hybrid-electrolytes design.

After collecting each of their appropriate electrolyte systems for cathodic/anodic electrochemical processes, the final step is synergistically combining them together into a full-cell system by the introduction of hybrid-electrolytes design strategy. Traditionally, the typical concept of hybrid-electrolytes system indicates an organic/

aqueous combination.[82-83] Separated by a Li-ion super-ionic conductor glass film (LISICON), lithium anode can be assembled within organic anolyte providing the most negative potential (-0.34 V vs. NHE), while varying aqueous electrochemical reaction can be operated in catholyte systems ($NiOOH/Ni(OH)_2$ or O_2/OH^-electro-couples, etc.).[84-86]

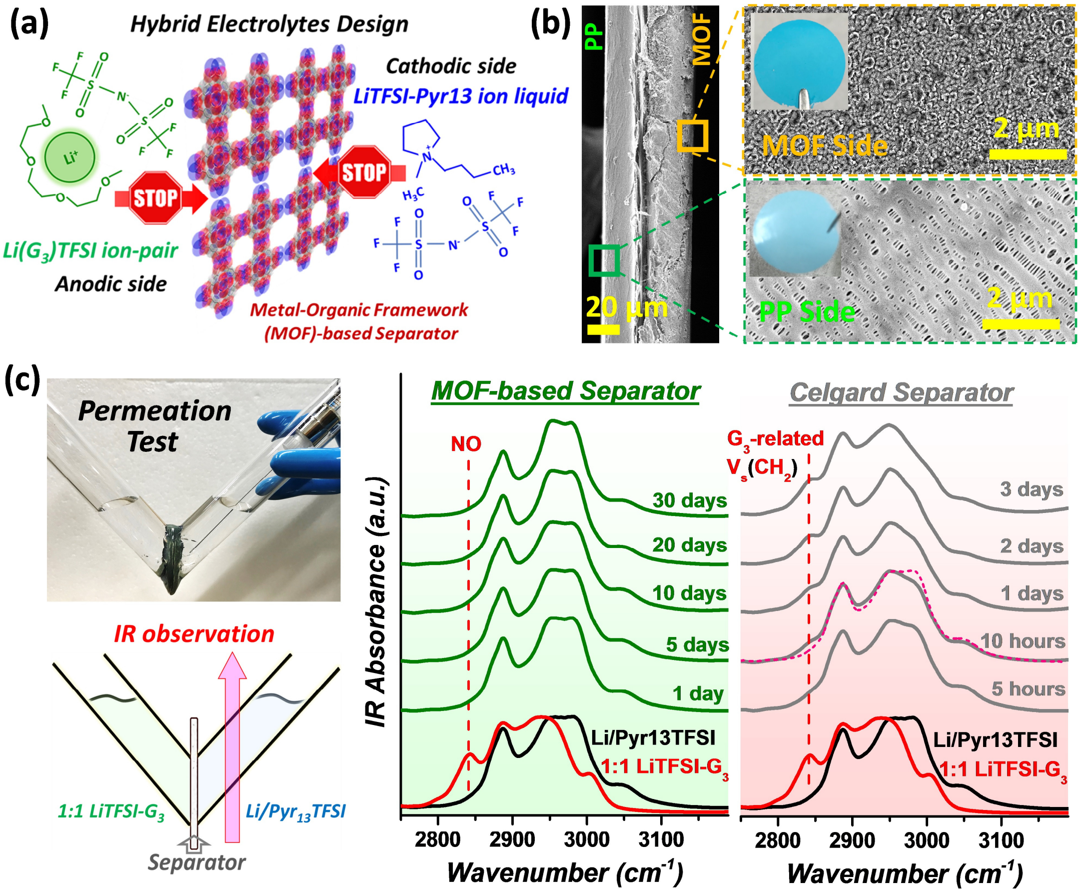

Figure 30. Design of hybrid-electrolytes strategy for 5 V-class cathode || graphite anode full-cell and corresponding separator introduction. (a) Schematic illustration of hybrid-electrolytes strategy. The design target is taking full advantages of each electrolyte systems by assembling them into a single full-cell, and simultaneously avoiding their shortcomings by separately trapping them into their adept spaces. We design a MOF-based separator, which acts as a sieve to inhibit the shuttling of each specific electrolytes. In this case, benefit from its remarkable oxidative stability, LiTFSI-Pyr_{13}TFSI would guarantee the reversibility of 5 V-class cathode as catholyte, while its detrimentally irreversible co-intercalation in graphite anode would be effectively prevented. For the anolyte, LiTFSI/G_3 equimolar complex is employed to

achieve highly reversible Li-GIC process at elevated temperature. (b) SEM images of the MOF-based separator. The sectional, frontal and back sides of the separator are shown for clarity. (c) Permeation tests conducted on MOF-based separator and conventional Celgard separator to assess the isolation effect towards the dual electrolytes. The specific separator is fabricated in the middle of a homemade V-type device, with each of its chambers filled with different electrolytes. By extracting trace amount of solution after certain aging times, the time-dependent FTIR results demonstrate no obvious shuttling can be observed in MOF-based separator assemble device after 30 days aging, while Celgard separator cannot inhibit the permeation.

Herein, inspired by this win-win strategy, we further improve it into a dual-organic hybrid-electrolytes design strategy for high-voltage Li-ion full-cell (Figure 30a). On the cathodic side, LiTFSI/Pyr_{13}TFSI IL-based electrolyte can provide high stability against oxidative attack at high voltage, without worrying about irreversible co-intercalation on graphite anode. Simultaneously, equimolar LiTFSI/G_3 electrolyte can hold reversible Li-GIC process on anodic side. Moreover, the superior thermal stability of both electrolytes have been proved in each of their corresponding half-cell system.

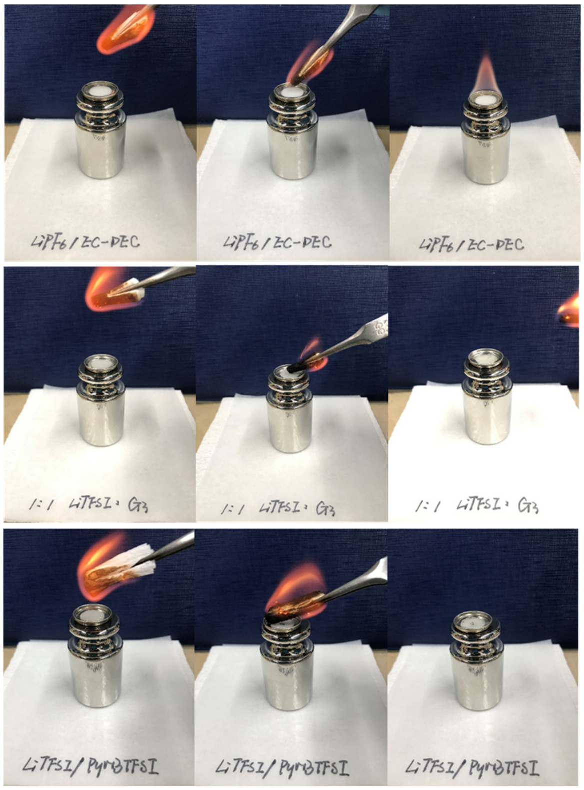

Figure 31. Flammability tests of the different electrolyte systems: typical LiPF6/EC-DEC (carbonates); equimolar LiTFSI/G_3 complex; LiTFSI/$Pyr_{13}TFSI$ ionic liquid-based electrolyte (from top to bottom). Compared with the conventional carbonate-based electrolyte, both of the employed electrolytes for hybrid-electrolytes design strategy present superior noninflammability.

Additionally, the non-inflammable nature of both selected electrolyte systems can effectively mitigate the potential safety risk of Li-ion cell architecture (Figure 31), a critical issue for practical application. Most importantly, owing to the narrow pore size window within the specific 3-D channel structure, metal-organic-framework (MOF)-based separator can be employed to separate the dual electrolyte systems, which would act as a sieve to inhibit their inter-crossover.

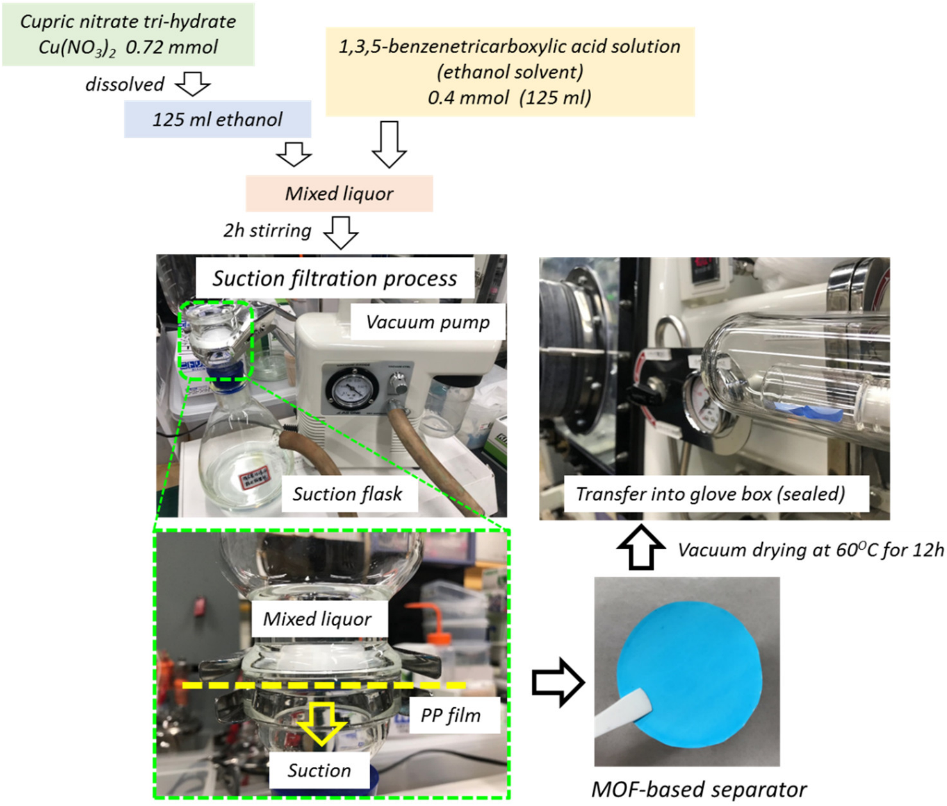

Figure 32. Fabrication process of the MOF-based separator.

Herein, we fabricate the MOF-based separator by $Cu_3(BTC)_2$ (HKUST-1, MOF), because its network structure is composed by ordered micropores with merely 6.9-9.0Å size window,[87-88] which is smaller than $Pyr_{13}TFSI$ molecule and $[Li(G_3)_1][TFSI]$ ion-pair. After the MOF particles in-situ growing onto a piece of as-prepared commercial PP separator, the void space between the MOF particles boundary would be filled with polymer (by solution filtering, Figure 32). Finally, a compactly fabricated MOF-based separator can be obtained, with a MOF-layer (thickness, ~30 nm) tightly adhered onto the PP-layer (Figure 30b).

The key role of the separator in hybrid-electrolytes strategy is definitely preventing inter-crossover of each electrolytes. We employ a homemade V-type device to simulate the related cell environment, within which the separator is assembled between the pair of electrolyte-filled chambers (Figure 30c). After injecting equi-volume of targeted electrolytes into each chamber, trace amount of electrolyte solution is extracted out for FTIR measurement after certain aging time. As a result, merely after 10 hours aging, a distinct shuttling crossover phenomenon can be observed in the device assembled with conventional Celgard separator (right red-filled block, Figure 30c). As a comparison, no obvious crossover can be detected after 30 days aging in the device assembled with as-prepared MOF-based separator (middle green-filled block, Figure 30c), which proved to be competent for hybrid-electrolytes design strategy.

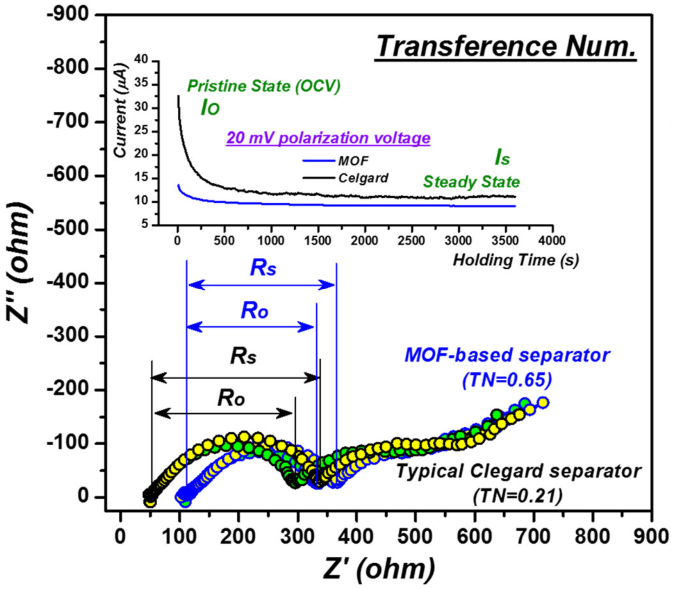

Figure 33. The transference numbers (TNs) of Li-ion observed in dual-electrolyte systems assembled by the different separators: typical Clegard separator (black traces) and MOF-based separator (blue traces).

The Li^+ transference numbers are tested by a potentiostatic polarization method in Li|Li sysmmetric coin cells. The potentiostatic polarization processes are performed with a constant potential at 20 mV for 3600s to record the current at pristine (OCV) and steady states, respectively. EIS before and after the potentiostatic polarization are also collected. The Li+ transference number is calculated according to the folloing equation. $t_{Li+} = I_s(V-I_0R_0) / I_0(V-I_sR_s)$. In which t_{Li+} stands for the Li+ transference number, I_0 and I_s present for the current obtained at initial and steady. R_0 and R_s present for the resistance before and after the potentiostatic polarization, V is the potentiostatic potential.

As a result, the Li-ion TN obtained in MOF-based spearator assembled cell (~0.65) is much higher than the one observed in Clegard separator fabricated cell (~0.21). In another word, once the crossover/diffusion of electrolytes is prevented (Li-ion can fluently diffuse) by the MOF-based separator, the transference of Li-ion would become more prepondrant. In summary, the differnece on Li-ion TN provide another evidence (from an electrochemical point of view) to proof the MOF-based separator can efficiently restrain the crossover of each electrolyte systems.

3.2.4 Superior cycling performance of LNMO || Graphite full-cell at elevated temperature.

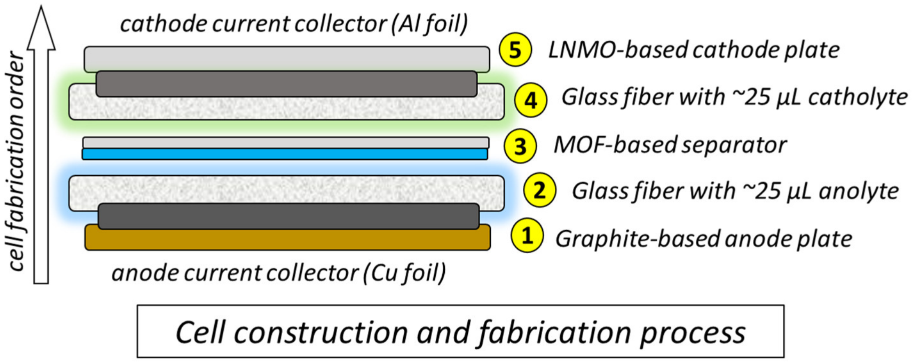

Figure 34. Schematic diagram of the full-cell (hybrid-electrolytes design strategy) fabrication process.

5 V-class LNMO graphite full-cell has been fabricated followed by the hybrid-electrolytes cell architecture strategy (Figure 34-35).

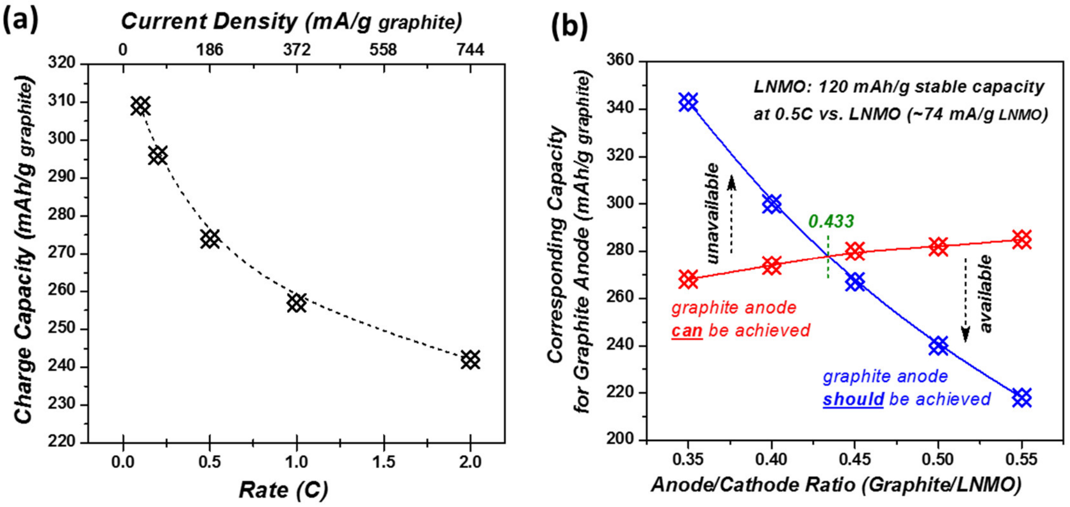

Figure 35. Detailed discussion on anode/cathode ratio within full-cell systems.

In detail, once the current density of full-cell system has been confirmed (0.5 C vs. LNMO cathode, 74 mA/g vs LNMO cathode), the selection and optimization of graphite/LNMO ratio in full-cell system depends on the practical capacities, which both electrodes can be achieved. For LNMO cathode, at a current density of 74 mA/g (vs. LNMO), the capacity of cathode can reach ~120 mAh/g. As for the graphite anode, the practical reversible specific capacities change from 310 mAh/g (0.1 C rate) to 240 mAh/g (2.0 C rate). In this case, there should be enough capacity for graphite in the full cell system, and this is the primary condition for the optimization of graphite/LNMO ratio in full-cell system. In figure b, with the varying of graphite/LNMO ratio, the red trace exhibits the specific capacity, which the graphite anode can be achieved (calculated from the cathode current density and the capacity fitting curves shown in figure 35a). While, the blue trace presents for the capacity, which the graphite anode should be achieved (calculated from the cathode capacity and cathode/anode ratios). If the y-axis value on the blue trace surpass the one present on the red trace, there would be not enough space on the graphite anode to accept the Li-ion from the LNMO cathode. In another word, the minimum value of the graphite/LNMO ratio would be 0.433. In this case, the current anode/cathode ratio (graphite/LNMO=0.5) would be an optimized and convincing value.

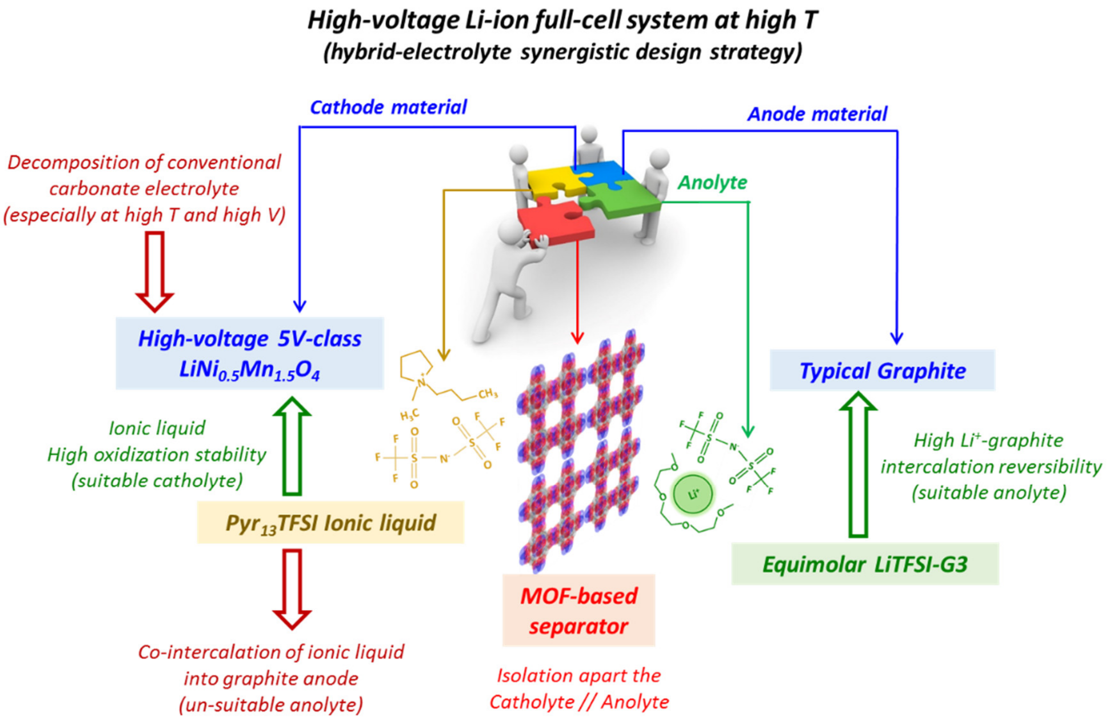

Figure 36. Schematic diagram for summarizing the multi-factors and synergistic design route within this hybrid-electrolytes composed high voltage Li-ion full-cell system.

The multi-factors and synergistic design route have also been introduced in other Li-ion battery systems (Figure 36).[89-90]

1) The initial motivation and target of this study: achieving a high-voltage Li-ion full-cell system, which can present long-term cycling stability at harsh (high temperature) environment.

2) The selection of cathode and catholyte: $LiNi_{0.5}Mn_{1.5}O_4$ is selected for the cathode material, due to its high voltage plateau (~4.7 V vs. Li/Li^+ plateau) and suitable specific capacity (148 mAh/g). Conventional LiPF6-EC/DEC electrolyte cannot meet the high polarization voltage for LNMO cathode, especially at high temperature. In this case, owing to its superior stability characterization, ionic liquid present to be the most suitable candidate as catholyte for high voltage and elevated temperature atmosphere.

3) The selection of anode and anolyte: Graphite is employed as the anode material, due to its high specific capacity and low voltage plateau. However, the ionic liquid would co-intercalate into the graphite anode, which cannot be employed as a suitable anolyte.

4) The hybrid-electrolytes design strategy: This contradiction drives the selection of electrolyte system into a deadlock. For one hand, ionic liquid is the most promising candidate for LNMO cathode. While, for another hand, ionic liquid would lead to huge irreversible capacity loss on graphite anode. However, if we can build a pair of independent spaces for each of the electrode reactions, the ionic liquid (catholyte) would not influence the graphite anode anymore.

5) The employment of MOF-based separator: Followed by the above-mentioned hybrid-electrolytes design strategy, we want to find a suitable separator, which can work as a sieve to completely restrain the inter-crossover of each electrolyte system (catholyte and anolyte). Benefit from the small pore window within the MOF framework, the Pyr13+ in ionic liquid catholyte cannot shuttle through the MOF-based separator. For the anolyte, we find equimolar LiTFSI:G3 electrolyte, in which the big solvated $[Li(G3)]^+$ cannot go across the window in the MOF framework (without further de-solvated process).

Finally, with the employment of 5V-class $LiNi_{0.5}Mn_{1.5}O_4$ spinel cathode, graphite anode, LiTFSI-Pyr_{13}TFSI catholyte, equimolar LiTFSI/G_3 anolyte and MOF-based separator, the synergistic hybrid-electrolytes design strategy realizes the initial motivation of this study: long cycling stability of high-voltage Li-ion full cell at high temperature.

At relatively low current rate, the Li-ion full-cell delivers an excellent cyclability at both room and elevated temperatures (Figure 37b), providing a stable high output voltage (beyond 4.5 V). Moreover, the initial capacity loss has been efficiently controlled (~10.5 mAh/g), and the subsequent cycles present very high average CE% (~99.6%). The rate capability at elevated temperature are also demonstrated (Figure

37c). Because of the sluggish Li$^+$ diffusion kinetics in ionic liquid and super-concentrated electrolytes, the specific capacity drops below 100 mAh/g at 2.0 C rate. However, once the current rate reversed back to 0.5 C, the capacity of the cell can be totally recovered, which still can provide an energy density of ~530 Wh/kg. Most encouragingly, after a low rate activation (0.2 C, 10 cycles), the hybrid-electrolytes-assembled full-cell delivers an ultra-stable long cycling stability at elevated temperature (Figure 37d). The full-cell holds an outstanding capacity retention of 83.3% after 1000 cycles at 0.5 C rate, and still presents a discharge capacity of 104 mAh/g during the 1000th cycle with an extremely high CE% (beyond 99.7%).

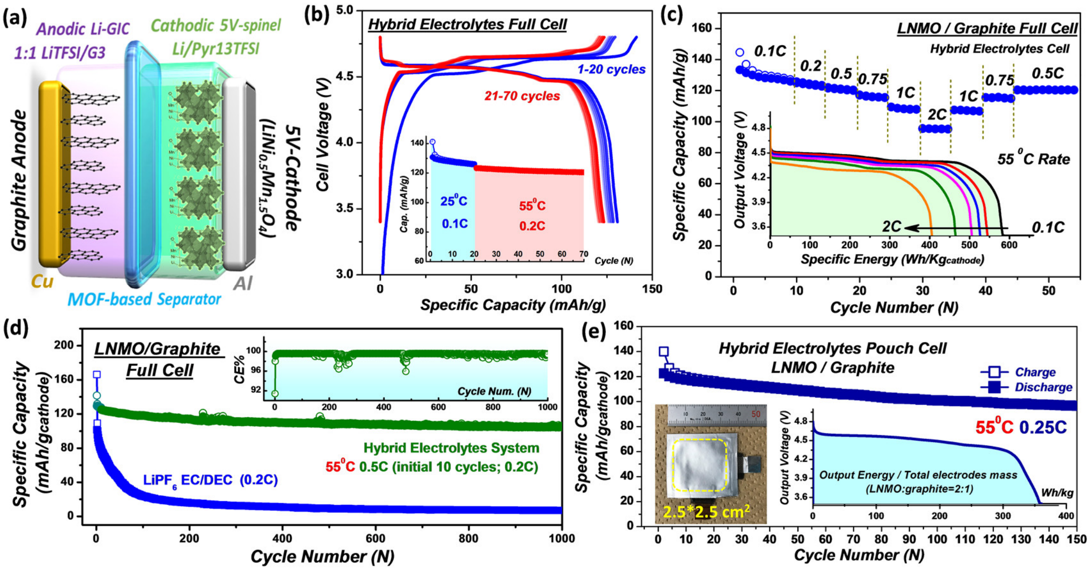

Figure 37. Elevated temperature electrochemical performance of high-voltage Li-ion full-cell assembled with hybrid-electrolytes design. (a) Schematic illustration of the hybrid-electrolytes full-cell structure. Anode: graphite; Anolyte: equimolar LiTFSI/G$_3$; Separator: MOF-based separator; Catholyte: LiTFSI-Pyr$_{13}$TFSI; Cathode: 5 V-class LiNi$_{0.5}$Mn$_{1.5}$O$_4$ spinel. (b) Voltage profiles and corresponding charge/discharge capacity hysteresis again cycle number. Cell voltage range: 3.4-4.8 V. Specific current rate: 0.1 C (1C=148 mA/g) for initial 1-20 cycles at room T (25°C); 0.2 C for subsequent 21-70 cycles at elevated T (55°C). (c) Rate performance. Corresponding output voltage against energy density (Wh/kg) curves are inset for clarity. (d) Long-term cycling performance. Charge/discharge capacity and coulombic efficiency (CE%, inset) against cycle number at 0.5 C rate (0.2 C for initial 10 cycle). High CE% (>99.5%) and

outstanding capacity retention rate (83.8% over 1000 cycles) can be achieved in hybrid-electrolytes full-cell at 55°C. Cycle life of typical $LiPF_6$/EC-DEC system is shown for comparison (blue trace). (e) Cycle life of pouch cell assembled with hybrid-electrolyte design. The photo and energy density profile of the pouch cell are shown inset. Note that, for both coin and pouch cell, the mass ratio between LNMO cathode / graphite anode are fixed at 2:1.

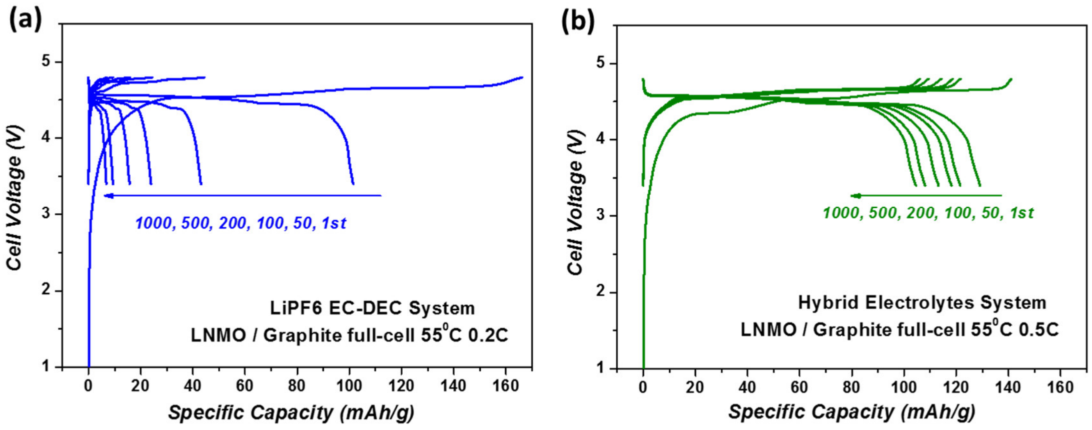

Figure 38. Typical galvanostatic charge/discharge curves of the LNMO graphite full-cell system collected during long-term cycling at elevated temperature: (a) typical $LiPF_6$/EC-DEC electrolyte; (b) hybrid-electrolytes system (catholyte: LiTFSI/Pyr_{13}TFSI; anolyte: equimolar LiTFSI/G_3).

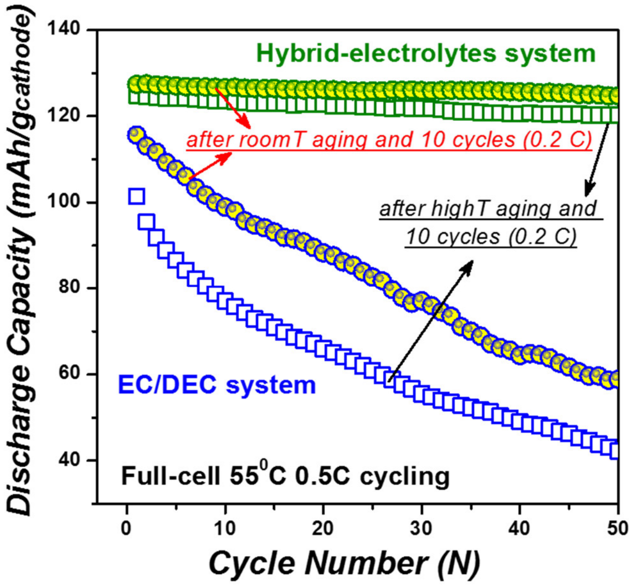

Figure 39. The elevated temperature (55°C) electrochemical performance of the full-cell systems assembled with $LiPF_6$-EC/DEC electrolyte (blue traces) and hybrid electrolytes system

(green traces). As a comparison, the pre-aging and pre-cycling (0.2 C rate) processes are conducted in both room temperature (25°C) and high temperature (55°C), respectively. As a result, although the room temperature pretreatment processes can, to some extent, relief the rapid degradation within EC/DEC cell system, the obvious decomposition and cell failure still cannot be restrained, especially compared with the cells fabricated by hybrid electrolytes system.

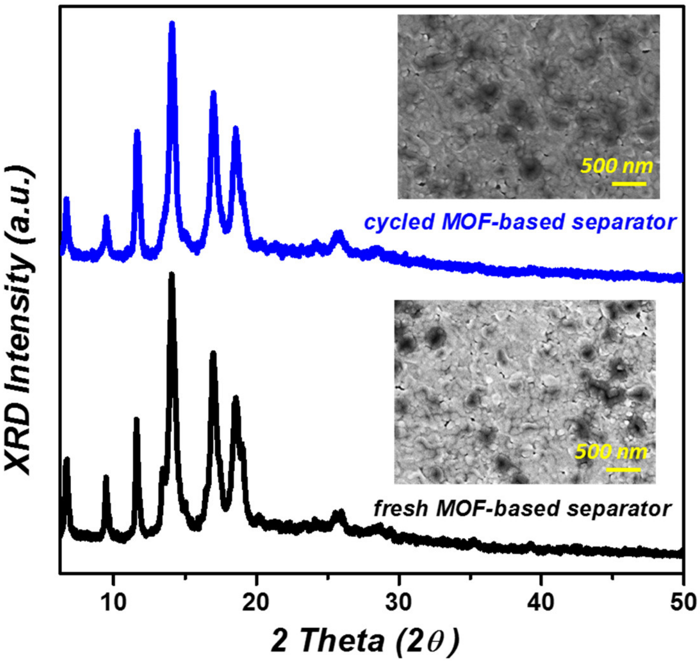

Figure 40. XRD pattern and SEM image of the MOF-based separator collected from the coin-type full-cell after 1000 cycles at elevated temperature. Compared with the pattern and image collected from pristine state, the cycled MOF-based separator do not suffer from obvious structural change, nor morphological degradation after long-term cycling, which indicates a superior stability and feasibility for hybrid-electrolytes design strategy in LNMO || graphite full-cell system.

Besides, MOF-based separate do not present obvious structure degradation after long-term cycling at elevated temperature (Figure 40). As a comparison, the full-cell assembled with typical $LiPF_6$/EC-DEC electrolyte suffers from serious initial capacity loss and rapid capacity deterioration (merely 15 mAh/g after 200 cycles). This rapid degeneration can be attributed to the electrolyte decomposition and dissolution-crossover-deposition induced anodic passivation (Figure 41), which have been systematically explained during half-cell discussion.

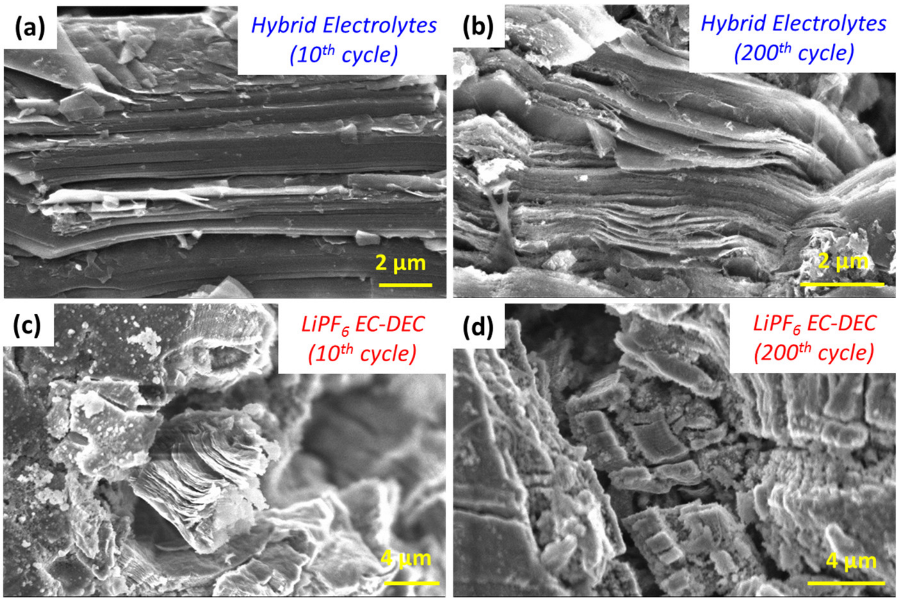

Figure 41. SEM images of cycled graphite anodes harvested from LNMO || graphite full-cell conducted at elevated temperature. The details of the electrochemical treatments are shown in Figure 30d.

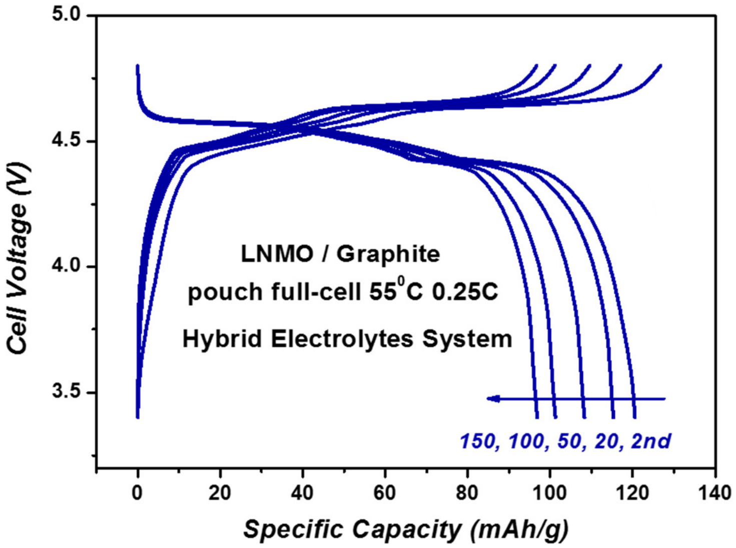

Figure 42. Typical galvanostatic charge/discharge curves of the LNMO || graphite pouch-type full-cell system collected at elevated temperature. The pouch cell was also fabricated followed by a hybrid-electrolytes design strategy (catholyte: LiTFSI/Pyr$_{13}$TFSI; anolyte: equimolar LiTFSI/G$_3$).

The graphite anodes present very different states after cycling in different electrolyte environments. In typical $LiPF_6$/EC-DEC system, the graphite anode suffer from serious distortion and surface passivation, which is remarkably restrained in hybrid-electrolytes-assembled condition. The degradation of anode is very harmful for the hull-cell system, which can be rationally ascribed to the dissolution-migration-deposition of dissolved metal-ions and related aggravated electrolyte decomposition/reduction, etc.

Additionally, the hybrid-electrolyte cell architecture can also be extended to a larger pouch cell device (Figure 37e and Figure 42), which also exhibits superior cyclability at elevated temperature.

3.3 Conclusion

In order to successfully achieve the practical application of high-voltage Li-ion full-cell, especially at harsher high temperature environment, electrolyte modification is a crucial but critical issue. Employment of improper electrolyte system would lead to detrimental influence towards electrochemical behaviors on both electrodes. However, it is extremely difficult for a single electrolyte systems to simultaneously satisfy several rigorous demands, for example: oxidative/reductive stabilities, compatibility and reversibility for anodic reaction, thermal stability, etc. In this study, we try to alleviate the difficulty for electrolyte optimization, and disperse the pressure into separated cathodic/anodic-reaction environments. Followed by this core principle, we introduce a hybrid-electrolytes cell architecture design strategy. A MOF-based separator is employed to separate the full-cell into pair of relatively independent electrolyte environments, while only Li^+ can fluently transport the MOF-derived sieve. LiTFSI/Pyr_{13}TFSI ionic liquid-based electrolyte is rationally employed as catholyte, due to its superior oxidative and thermal stabilities. Meanwhile, without bringing harmful influence of Pyr_{13}TFSI into the graphite-related anodic electrochemistry, we introduce another independent anolyte system, equimolar LiTFSI/G_3 complex, which reveals pronounced improvement for irreversible Li^+ de-/intercalation on graphite anode. As a result, fabricated with this hybrid-electrolytes strategy, a 5 V-class $LiNi_{0.5}Mn_{1.5}O_4$ || graphite full-cell delivers ultra-high long-term cyclability and superior capacity retention rate at elevated temperature (83.8% after 1000 cycles). The achievement of outstanding electrochemical performance at harsh cell working condition (high-voltage and elevated-temperature) strongly prove the practical availability of the newly-introduced cell architecture. Finally, not just limited within LNMO || graphite full-cell system, we hope this feasible design strategy can be further developed as a universal design principle, promoting the practical application of high-voltage Li-ion full cells.

Chapter 4

Hybrid Electrolytes Design (HED) for Graphite | Graphite Dual-Carbon High-Voltage Li-ion Battery

Chapter 4. Hybrid Electrolytes Design (HED) for Graphite | Graphite Dual-Carbon High-Voltage Li-ion Battery

4.1 Introduction

Very recently, due to the high electrochemical intercalation potentials (over 4.7 V vs. Li/Li$^+$), anionic Graphite-Intercalation-Chemistry (GIC) behaviors have received remarkable attention for designing novel energy storage devices, for example: dual-ion batteries. Meanwhile, combine with the low GIC potential for Li$^+$ cation (~0.2 V vs. Li/Li$^+$, as a classical/practical anode for commercial Li-ion batteries), a dual-graphite battery can be achieved by the redox potential gap between the pair of amphoteric GIC processes. The most outstanding advantages of dual-graphite energy storage devices can be summarized as: (i) high output voltage; (ii) environmental safety; (iii) cost benefits.

However, several inherent defects have been gradually revealed, especially the electrolyte issues. Typical commercial electrolytes for Li-ion battery cannot bear the high oxidation potential on cathode, while other high oxidative-stability electrolyte systems (ionic liquid, etc.) would lead to irreversible capacity loss on anode. Thus, single electrolyte system cannot simultaneously meet the requirements on both graphite ectrodes, which would inevitably restrain the improvement of its cycling performance.

In this work, we rationally introduce a specific organic/organic hybrid electrolytes design strategy into the dual-graphite battery system, in which a Nafion-based separator segregates two different electrolyte systems into each of their suitable GIC environments. On the cathodic side, outstanding oxidative stability of ionic liquid electrolyte enables the high reversibility of anion-GIC process. Simultaneously, on the anodic side, specific aggregated ion-pair structure within a super-concentrated ether-based electrolyte insures the highly reversible cation-GIC process. Moreover, the full-cell has been assembled with balanced capacity-equivalent mass loading proportion between cathode and anode, while this very important practical issue has also been firstly highlighted to the forefront in dual-graphite/ion cell systems. The hybrid electrolytes strategy in dual-graphite cell synergistically combines the advantages of each electrolyte systems, displaying a promising high CE (around 99.7%) and superior long-term cycling stability (over 3000 cycles at 100 mA/g current density). In addition, spectroscopic investigations (in-situ Raman, HR-TEM, XPS, NMR, etc.) have been systematically conducted to clearly reveal degradation mechanism of cation-GIC in ionic liquid electrolyte system, and elucidate the influence of different electrolyte features on the mechanism of Li^+ intercalation (Li-GIC) processes.

In summary, for the dual-graphite battery system, after systematically elucidating the degradation mechanism by comprehensive spectroscopic investigations, we specifically introduce a hybrid electrolytes design strategy and successfully overcome the corresponding inherent defects in each of the separated electrolyte systems. The outstanding electrochemical performance not only proves the rationality of our design, but also regains the confidence for the development of more practical/commercial dual-graphite (dual-ion) battery systems with high output voltage, low-cost graphite electrodes, long cycle life and safety superiorities over traditional Li-ion battery systems.

4.2 Results and Discussion

4.2.1 Electrochemical performance of GIC processes in IL-based electrolyte.

The ideal working (charging) mechanism of a dual-graphite cell is illustrated schematically in Figure 1a for a typical Li-contained electrolyte system (LiTFSI as cation & anion donor sources). In this cell, the electrolyte not only act as a charge carrier (in conventional Li-ion batteries), but also be regarded as the source for GIC guests.[27] Theoretically, Li^+ intercalates into the graphite anode (Li-GIC), and $TFSI^-$ intercalates into graphite anode simultaneously during charging. The corresponding de-intercalation processes should irreversibly conduct during subsequent discharge process, composing a cycle in typical dual-graphite cell. As introduced before, compared with other organic solvents (Figure 2), Li-contained IL (LiTFSI-Pyr$_{13}$TFSI) has been predominantly employed as the electrolyte due to its superior stability towards oxidative decomposition upon anion-GIC.

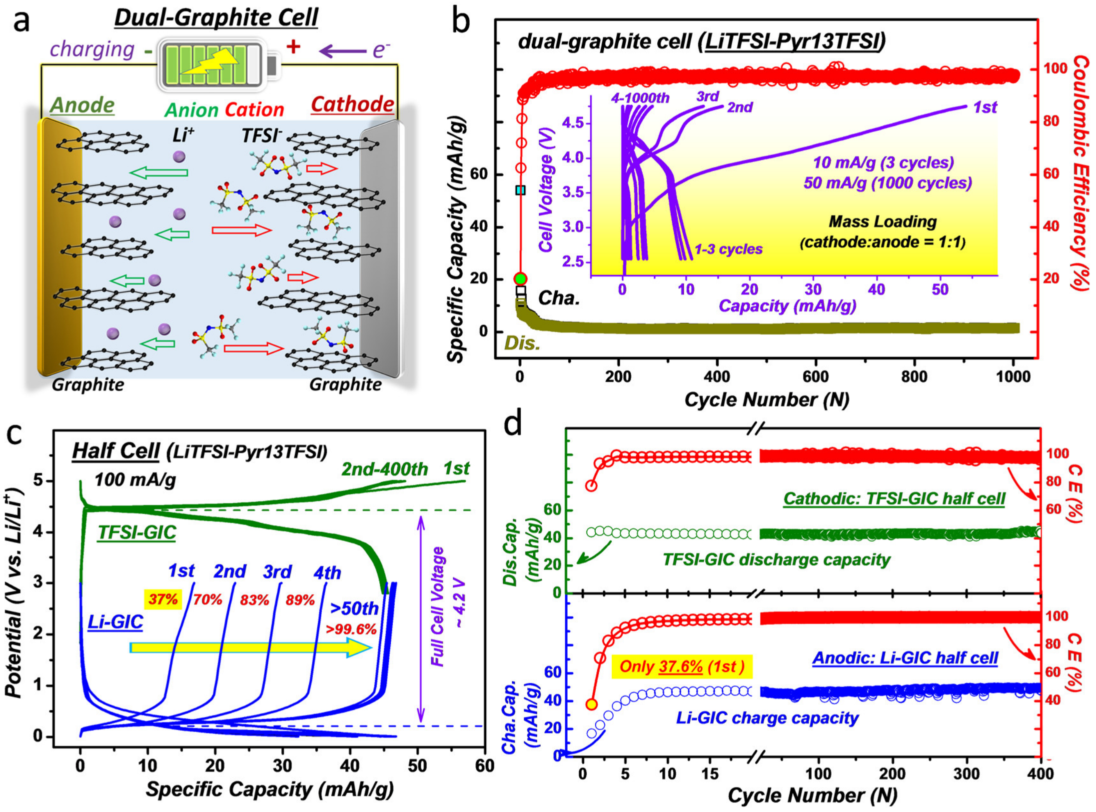

Figure 1. Electrochemical characterizations of dual-graphite full-cell and corresponding cathodic/anodic half-cells assembled with LiTFSI-Pyr$_{13}$TFSI based ionic liquid (IL) electrolyte. (**a**) Schematic illustration of a typical dual-graphite full cell wherein cation (Li^+) and anion ($TFSI^-$) simultaneously intercalate into graphitic layered structures within the anode and cathode upon charging, respectively. (**b**) Cycling behavior of the dual-graphite full-cell assembled with capacity-equivalent cathode/anode mass loading proportion. Insets present the voltage profiles. During the initial several cycles, the seriously irreversible capacity loss leads to the rapid degradation of the full-cell. (**c**) Voltage profiles of graphite-Li half cells. The potential gap between the pair of cathodic (green traces) and anodic (blue traces) Graphite-Intercalation-Chemistry (GIC) processes contributes the cell voltage of the dual-graphite full-cell. (**d**) Discharge/charge capacity hysteresis against cycle number harvested from each of the

half-cells. Although the superior oxidative stability of IL guarantees the reversibility of TFSI-GIC process (cathodic half-cell), the extremely low coulombic efficiencies revealed during initial Li-GIC cycles (anodic half-cell) inevitably lead to the irreversible capacity loss in the dual-graphite full-cell. The employment of IL electrolyte reveals to be a double-edge sword for dual-graphite cell.

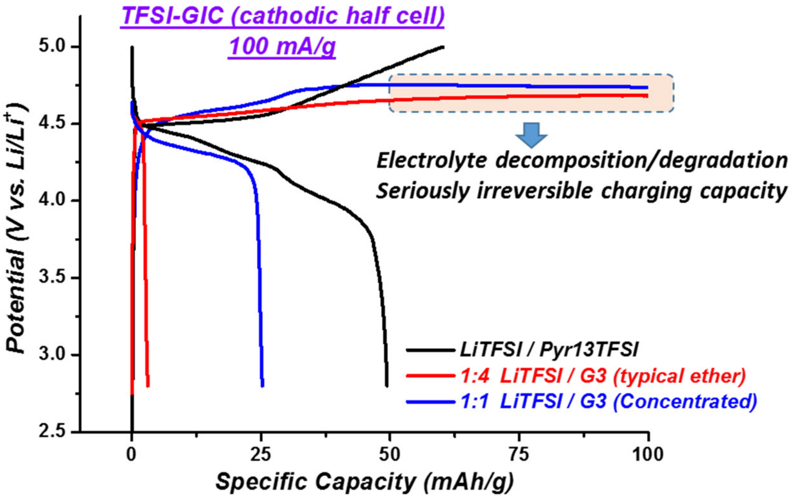

Figure 2. Galvanostatic curves of anion-GIC process observed in varying electrolyte systems. Typical dilute ether-based electrolyte (1:4 LiTFSI-G_3, red trace); super-concentrated ether-based electrolyte (1:1 LiTFSI-G_3, blue trace); IL-based electrolyte system (1.5 M LiTFSI-$Pyr_{13}TFSI$, black trace).

For anionic GIC process (half-cell), the electrochemically anionic intercalation process requires very high working potential (surpass 4.5 V vs. Li/Li^+). Typical organic electrolyte system (EC-DEC, EC-DMC, ether-based, etc.) cannot endure such a polarized potential, and inevitably suffer from oxidative decomposition. As a result, the charge/discharge processes present obviously irreversible capacity loss. Although the super-concentrated electrolyte system can, to some extent, restrain the oxidative decomposition (compared with the dilute system, red trace), the irreversible phenomenon cannot be efficiently controlled (blue trace). While the advantage of IL-based electrolyte system has been distinctly revealed, in which the irreversible electrolyte decomposition has been effectively limited.

However, in the dual-graphite full cell (Figure 1b) assembled with balanced capacity-equivalent mass loading proportion, the reversible cycling cannot be achieved as predicted. A large irreversible capacity loss (~40 mAh/g) can be observed during the 1st charging process, resulting in an extremely low initial CE (merely ~ 20%). Moreover, tuning the specific capacity-dependent mass loading ratio of graphite electrodes cannot essentially restrain the capacity loss Figure 3). Obviously, the severely irreversible degradation seriously limits the practical application of IL-based dual-graphite technology.

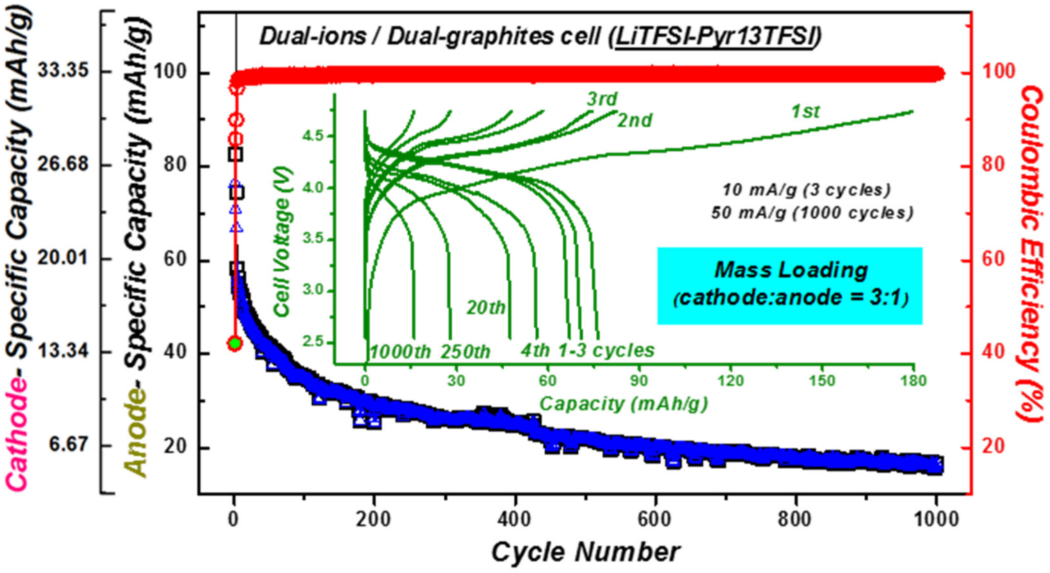

Figure 3. Cycling behavior of the dual-graphite full-cell assembled with pure LiTFSI-Pyr$_{13}$TFSI electrolyte (cathodic/anodic mass loading, 3:1). Compared with the dual-graphite cell present in Figure 1b, the mass loading herein has been changed into 3:1. However, based on the inserted voltage profiles, the serious irreversible discharge capacity during initial cycle still remains to be the un-solved problem.

In this case, modifying the mass loading ratio cannot essentially solve the problem of the IL-based dual-graphite cell. After deeply unraveling the corresponding degradation mechanism in Figure 2 (irreversible co-intercalation upon anodic anion-GIC process in IL), the phenomenon present herein can be easily comprehended. Although the mass loading on the cathode (TFSI-GIC host) has been extended, the irreversible capacity loss remains to be unchanged. In this case, after the initial charging, lot of TFSI$^-$ still trapped inside the graphite cathode, which cannot reversibly de-intercalate out during the subsequent discharging process. In a word, without solve the problem(s) during anion-GIC, the change of mass loading ratio cannot essentially improved the cell performance.

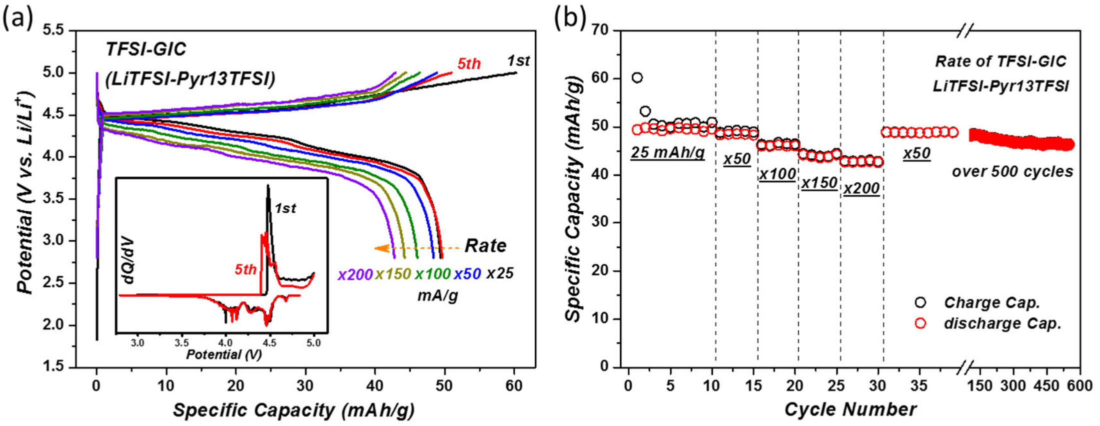

Figure 4. Rate performance of dual-ion half-cell (TFSI-GIC process) assembled with IL-based electrolyte (1.5 M LiTFSI-Pyr$_{13}$TFSI). (a) Voltage profiles of galvanostatic curves observed at various current rates (5.0 V vs. Li/Li$^+$ upper cut-off voltage). (b) Discharge/charge capacity hysteresis against cycle number harvested from the cell.

The dual-ion half-cell (graphite/Li, TFSI-GIC) presents good rate performance. Particularly, after turning back to 50 mA/g current density, the corresponding cell can still exhibit very stable cycling performance (over 500 cycles). Notably, based on very classic explanation proposed by M .Winter and co-workers, the low coulombic efficiency (CE) during the initial cycle can be assigned to a kinetic/dynamic hindrance during the 1st TFSI- (anion) intercalation process between the graphene sheets, which would disappear after few cycles until the graphite particles are completely wetted.[38, 91]

In order to revealing the crucial drawback, anion- and cation-GIC processes are separately investigated in corresponding metallic Li/graphite half cells (Figure 1c and 1d, Figure 4). For the TFSI (anion)-GIC process (green traces, Figure 1c), the initial capacity loss is only about 11 mAh/g, and the subsequent cycling exhibits an excellent stable performance over 400 cycles at 100 mA/g current density (Figure 1d). The stable reversible TFSI-GIC capacity is mainly attributed to the superior oxidative stability of $Pyr_{13}TFSI$ electrolyte, which is also well consistent with the motivation on the employment of IL electrolyte in dual-graphite system. However, turning to the Li-GIC process in anodic half cell (blue traces, Figure 1c), although the capacity can be stably preserved during the subsequent hundreds of cycles with a high CE, the charge capacity loss within the initial several cycles (especially merely 37.6% CE during the 1st cycle) indicates an irreversible de/intercalation behavior. However, this phenomenon is essentially different from the 1st cycle CE loss consumed by SEI-formation during typical Li-GIC (observed in EC-DMC related environments), in which the discharge capacity should not keep constant, nor the charge capacity present an obvious increasing trend (Figure 5).[28]

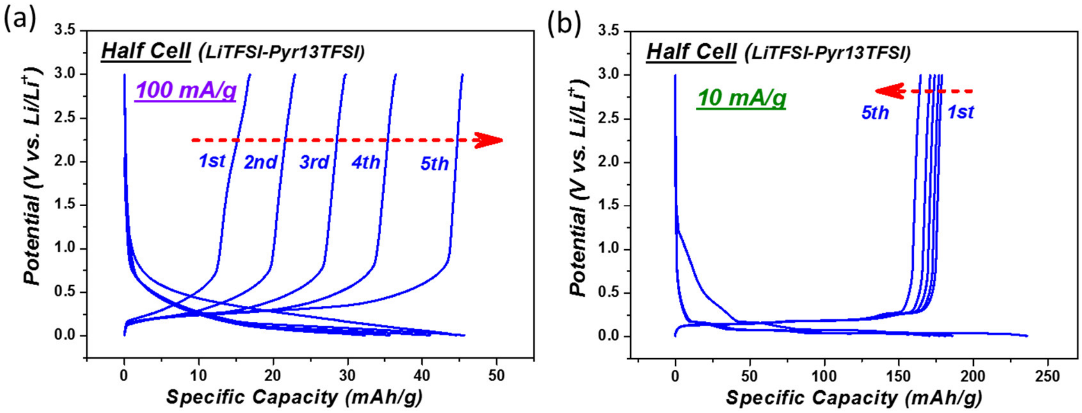

Figure 5. Voltage profiles of graphite-Li half cells (cation-GIC) assembled with $LiTFSI/Pyr_{13}TFSI$ IL-based electrolyte cycling at different current density rates: (a) high rate 100 mA/g; (b) low rate 10 mA/g.

The most obvious difference between the two rates presents on the variation trends of charge capacity (corresponding Li de-intercalation process). At 100 mA/g (high rate), the charge capacities increase, while, on the contrary, the charge capacities decrease at 10 mA/g (low rate). Compared with the typical SEI-formation mechanism observed in carbonated-based electrolyte system (EC/DMC, etc.), the increasing charge capacities are quite abnormal. In IL-based electrolyte, due to the dynamics reason, the intercalation of Li^+ present very sluggish. Especially at high current rate, the intercalation capacity (merely around 50 mAh/g) present far from theoretical value (372 mAh/g, LiC_6) at 0.01 V cut-off voltage. In another word, take into the irreversible Pyr_{13}^+ co-intercalation, there is still enough space (active site within graphite layer) for cation intercalation during 2nd discharging. However, due to the gradually obstructed layer space (filled by irreversible Pyr_{13}^+), the intercalation of Pyr_{13}^+ become more and more difficult than smaller Li^+. The reversible Li- intercalation gradually become dominate, and the related coulombic efficiency finally reaches nearly 99.8% after 20 cycles (Figure 1d). However, at low current rate (10 mA/g), the discharge capacity increase to 240 mAh/g, and the irreversible Pyr_{13}^+ co-intercalation reaches its limitation during the very initial several cycles. As a result, the Li-intercalation quickly become dominate, and the abnormal increasing trend of charge capacity cannot be observed at low current rate. Notably, no matter how quickly the pure/irreversible Li-intercalation become dominate, the irreversible co-intercalation of Pyr_{13}^+ still occupy the limited active layer spaces within graphite, which is essentially harmful in the full cell.

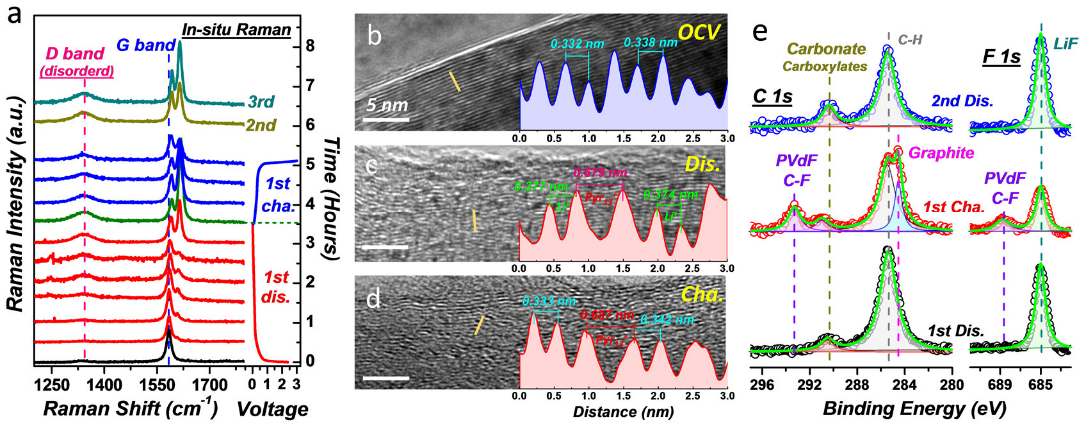

Figure 6. Investigation on the mechanism of irreversible capacity loss observed in IL (LiTFSI-Pyr_{13}TFSI) electrolyte during Li-GIC. (**a**) Time dependent in-situ Raman spectra collected from graphite-Li half-cell during Li-GIC process (current density, 30 mA/g). Both of the unrecoverable variation trends of G-band and residue disordered feature (newly-produced D-band) indicate an irreversible change of graphitic structure during Li^+ intercalation. (**b-d**) HR-TEM images of graphite electrodes with each of their corresponding lattice distances: (**b**) pristine state; (**c**) after discharge (intercalated state) and (**d**) after charge (de-intercalated state). HR-TEM analysis exemplifies that the co-intercalation of IL (Pyr_{13}^+ cation) leads to large

expansion of graphitic lattice distance, which cannot fully recover due to the residual Pyr_{13}^+ after charge process. (**e**) XPS spectra (C 1s and F 1s) of cycled graphite electrodes harvested after 1st discharge (black trace), 1st charge (red trace) and 2nd discharge (blue trace) processes, respectively. After 1st charge process, the re-exposure of graphite electrode (newly-observed graphite and PVdF-related peak) indicates that the de-intercalation process damage the SEI film formed during 1st discharging. Therefore, in IL electrolyte, the irreversible capacity loss during Li-GIC can be rationally assigned to the irreversible co-intercalation of large organic cation (Pyr_{13}^+), which can also inevitably result in exfoliation of graphite layer and instability of SEI surface film.

This abnormal behavior indicates some trapped cations may not able to de-intercalate during charging. Subsequently, due to the discharge capacity is far more below the theoretical Li-GIC limitation (372 mAh/g for LiC_6 compound),[92] Li^+ can continuously intercalates into residual free site in graphite layer during the following discharge process. The final stable state is determined by a complicated SEI-formation/saturation and IL co-intercalation processes, which would be exemplified in the subsequent section (Figure 6).

Notably, in the Li-GIC based graphite/Li half-cell, the irreversible de-intercalation during 1st cycle would not essentially influence the 2nd discharge capacity, since Li^+ would be sustainably supplied from excessive metallic Li foil and there is plenty of spaces between graphite layers for cationic intercalation. Differently, in dual-graphite full-cell, the irreversible cation de-intercalation during on anode would directly lead to the similar irreversible de-intercalation of $TFSI^-$ anion on cathode, resulting in some $TFSI^-$ residue trapped inside discharged cathode. However, during the 2nd charging, owning to the limited TFSI-GIC capacity (~50 mAh/g limitation for TFSI-GIC in pure IL),[36] the capacity of TFSI-intercalation would be restrained by the residual $TFSI^-$ after 1st cycle. In another word, the amount of re-intercalated $TFSI^-$ during 2nd charging process wholly depends on the spaces released during the 1st discharging process. Thus, it can also explain why the 2nd charging capacity presents very close to the 1st discharging capacity in dual-graphite full cell (Figure 1b and Figure 3). As a result, the cell assembled with balanced capacity-equivalent cathode/anode loading proportion would rapidly failed due to the irreversible filling with un-deintercalated anion on cathode side. Moreover, in order to make preparatory space to remedy the irreversible de/intercalation, rigidly fabricating excessive cathode would break the balance of the capacity-equivalent loading proportion principle, and bring no help for essentially solving this practical issue. Also, to the best of our knowledge, this is the first time that this very practical issue has been revealed as a criterion. Consequently, the large irreversible capacity observed during cation-GIC process on graphite anode has been proved as the crime culprit for the degradation of dual-graphite full cell in IL electrolyte system.

4.2.2 Degradation mechanism of cation-GIC process in IL-based electrolyte.

After locking in the dominate drawback within IL-based dual-graphite cell, revealing the irreversible mechanism during cation-GIC would be remarkably important for designing further modification strategy to remedy the defect. To the best of our knowledge, the current explanations for the related irreversible behavior are mainly speculated based on electrochemical behaviors, while there present very limited amount of spectroscopic evidence to clearly demonstrate this process.[42, 44] Herein, with the collections of several spectroscopic evidences, we conduct the analysis on both graphite structural variation and surface SEI formation.

Figure 6a shows the overview of in-situ Raman spectra recorded during cation-GIC in Li/graphite half-cell. The most prominent changes exhibited in Raman spectra is the splitting of the G-band (a sharp band around 1582 cm^{-1} assigned to highly crystalline graphitic E_{2g} mode) and the appearance of the D-band (a broad band at 1343 cm^{-1} assigned to disordered finite crystalline A_{1g} mode).[73, 76] During cation intercalation (discharging), the blue shift and splitting of G-band can be attributed to the well-known formation of stages intercalation compounds.[93] The increasing of peak at higher wavenumber ($E_{2g(b)}$, mode of boundary graphene layers adjacent to intercalation layers) indicates the growing amount of intercalated cations.[71] However, at the end of 1st charge, the blue shift of G-band do not store back and the spectrum still presents two splitting E_{2g} modes, which exhibits strong indication that the de-intercalation of cation is not complete, implying the residual cations remain in the graphite matrix. What was worse, the appearance of D-band after 1st charging indicates the formation of irreversible defects and disorder in the graphite structure.[76] Moreover, this irreversible structure degradation can be accumulated and become more aggravated after 2nd and 3rd cycles. Such an irreversible de/intercalation behavior is further visually illustrated by HR-TEM analysis (Figure 6b to 6d). Compared with the well-ordered lattice fringe (~0.33 nm, Figure 6b) observed on pristine graphite,[74] the graphene layers become wrinkled and exhibit two kinds of expanded interlayer distances: ~ 0.38 nm (a traditional Li^+ intercalated distance) and ~ 0.68 nm (intercalated by big Pyr_{13}^+ cation) after discharging (Figure 6c). However, after charging (Figure 2d), only Li^+ de-intercalates out from the graphite layer, while the Pyr_{13}^+ still remains residual within the interlayer. Thus, the irreversible capacity loss and low CE can be assigned to the irreversible co-intercalation of big IL cation. Notably, partial Pyr_{13}^+ intercalated into near-surface layered region maybe reversibly de-intercalated, but the related irreversible residue is clearly illustrated. Besides, the co-intercalation behavior inevitably exacerbates the stress and induces the exfoliation of graphite structure, which is demonstrated by SEM images of exfoliated graphite after cycled in IL electrolyte Figure 7).

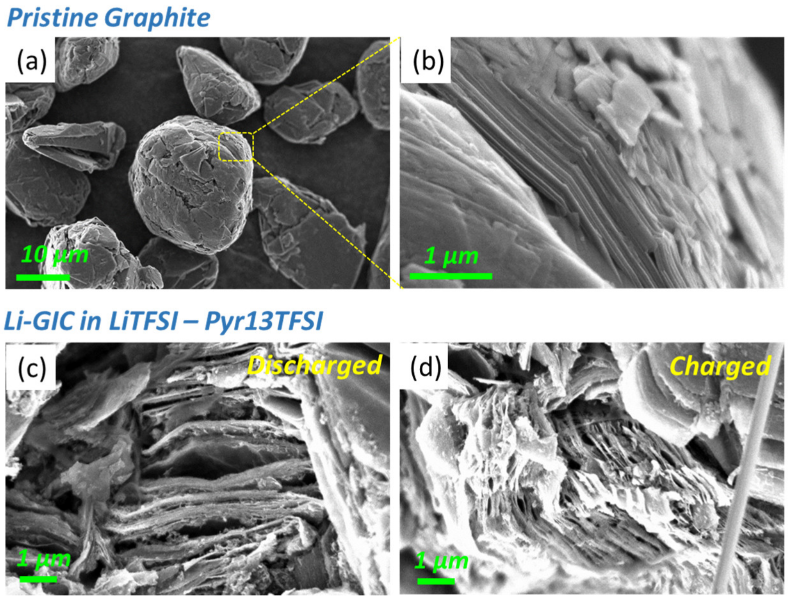

Figure 7. SEM images of the graphite electrodes. (a-b) Pristine graphite particles. Cycled graphite electrodes harvested from the Li-GIC graphite/Li half-cell assembled with IL electrolyte (1.5 M LiTFSI-Pyr_{13}TFSI): (c) after discharging (cation intercalated state); (d) after charging (cation de-intercalated state).

On the commercial graphite particles, well-distributed and homogeneous graphite galleries can be clearly observed. However, after discharged in Pyr_{13}TFSI-based electrolyte, Li co-intercalation leads to serious exfoliation of graphite layer. This irreversible destroy cannot be restored after charging, which present well coincide with the irreversible behavior of the co-intercalation of huge organic cation (Pyr_{13}^+) revealed by spectroscopic characterizations (shown in Figure 6). The SEM images also present as a visualized evidence to prove the related degradation mechanism proposed in the discussion section of Figure 6. Also, the graphite exfoliation behaviors have also been reported during various Li-GIC processes, which have been assigned to PC-related irreversible solvent co-intercalation and long-term cycling degradation, respectively.[75-76]

SEI formation is another core section within the discussion of GIC processes. Based on the pioneer explanations proposed in previous studies, owning to the superior reductive stability of IL, SEI cannot be stably formed during Li-GIC, and IL co-intercalation cannot be restrained.[38, 42] However, the contradiction point is although irreversible IL co-intercalation leads to the low CE during initial cycles in Li-GIC half-cell, the high reversibility during the subsequent hundreds of cycles indicates a stable irreversible process has been gradually achieved (blue traces, Figure 1c and 1d). Herein, based on XPS harvested from 1st discharged graphite electrode, the formation of LiF-based SEI can be clearly observed (bottom black trace, Figure 6e), which can be rationally ascribed to the reduction of another electrolyte component, LiTFSI salt. However, it is noteworthy that the LiF-composed SEI film suffer from an obvious damage after 1st charging process (cation de-intercalation), resulting in the re-exposure of fresh graphite surface (also PVdF binder), which proved by the observation of corresponding peaks in XPS spectrum (red trace, Figure 6e). Then, the surface of exposed graphite is re-covered by the newly-produced LiF-based SEI film after 2nd discharging (blue trace, Figure 6e). Moreover, both the destruction and re-construction of SEI are also clearly confirmed by NMR and HR-TEM results (Figure 8-10).

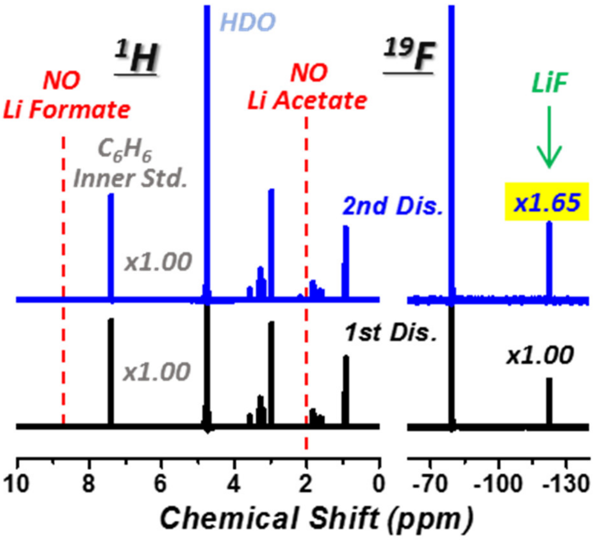

Figure 8. NMR analysis for SEI components during Li-GIC in IL electrolyte. ^{1}H and ^{19}F NMR spectra of D_2O-extracted components from discharged IL-based Li-GIC half-cells (un-rinsed graphite electrode and separator). Both the carboxylates (formate and acetate, etc.) and flouride (LiF, etc.) are quantitatively estimated based on the normalized peaks of C_6H_6 and C_6H_5F internal/inner standards.

Corresponding XPS analysis performed in Figure 6e has qualitatively confirmed the components of SEI film formed on graphite surface (in IL-based electrolyte system). Herein, quantitative NMR analysis would be very helpful to further clarify the SEI-formation mechanism. Herein, NMR results also indicate the formation of LiF and the absence of carboxylates component within SEI, which is consistent with the XPS results (Figure 6e). More importantly, the amount of LiF increases after 2nd discharging. This is a strong evidence to prove the proposed re-construction of LiF-based SEI film. The abnormal formation of SEI during 2nd discharge process also indicates the unstable nature of Li-GIC process conduct in IL-based electrolyte system.

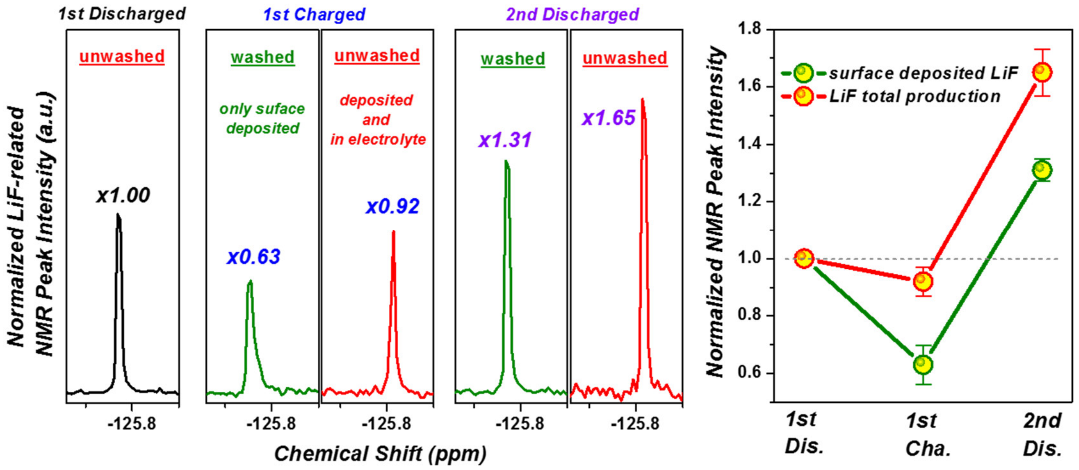

Figure 9. Normalized LiF-related ^{19}F NMR peaks collected from the graphite electrodes harvested from Li-graphite half cells (Li-GIC) assembled with LiTFSI-Pyr$_{13}$TFSI IL-based electrolyte.

Firstly, the difference between the peaks collected from washed and un-washed electrodes should be noted. Some of the loose LiF fragments (due to the destruction of SEI film after 1st charging/de-intercalation) would be washed off/away. In this case, there is obvious difference between washed (62%) and un-washed (92%) electrodes after 1st charging. Only 62% of SEI film stably deposited after de-intercalation, while the total amount of SEI components nearly do not change (92%, unwashed). In this case, the "damage/destruction" of SEI film after 1st charging/de-intercalation can be clearly revealed in IL-based electrolyte system upon Li-GIC process.

After 2nd discharging/intercalation, the "re-construction" of SEI film can be clearly exemplified by the increasing of SEI component (the newly-produced 70% SEI film). The amount of loose LiF fragments stay constant (around 30%) after 2nd discharging.

Traditionally, once produced after the 1st discharging process, SEI film cannot be destructed during subsequent discharging (pure Li$^+$ de-intercalation) in typical electrolytes (EC/DMC system, etc.).[94] However, in IL electrolyte system, some co-intercalated Pyr$_{13}$$^+$ within partial near-surface interlayer region would dynamically de-intercalate, and such a large cation cannot go through the SEI film, which unavoidably leads to the related destroy. With the accumulation of SEI fragment during cycling, both intercalation and de-intercalation of Pyr_{13}^+ is gradually restrained, and the pure Li-GIC process become dominated during subsequent cycles. In this case, the stable reversible GIC process during the hundreds of cycles in anodic half-cell can be rationally explained.

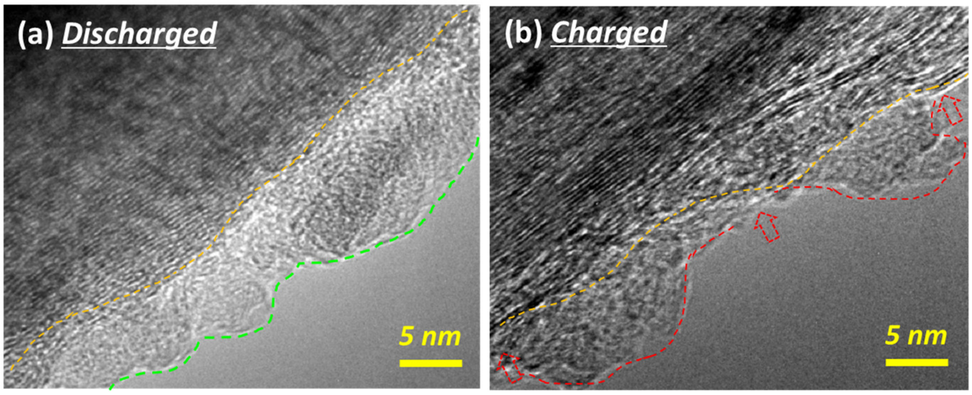

Figure 10. HR-TEM images of the cycled graphite electrodes harvested from the Li-graphite half-cell (cation-GIC) assembled with LiTFSI-Pyr13TFSI IL-based electrolyte. (a) after 1st discharging (intercalated state); (b) after 1st charging (de-intercalated state).

After the formation of homogeneous SEI film after discharging, the local destruction of the SEI film can be clearly observed after subsequent cation de-intercalation (charging process). This destroy phenomenon can be rationally attributed to the de-intercalation of huge Pyr_{13}^+ cation (near the surface region). Besides, the visual HR-TEM results also coincide with the quantitative analysis performed based on NMR spectroscopy (Figure 8-9).

In summary, this is the first time that the details of the cation-GIC mechanism in IL electrolyte has been illustrated. The irreversible capacity observed during initial several cycles have been assigned to both co-intercalation of IL cation and abnormal re-construction behavior of SEI-film, pair of inherent defects tightly correlated with each other. Even though the employment of specific additives would help the building of stable SEI protecting film, the co-intercalation of IL cation would not be immediately prevented during the initial cycles, which still remains the GIC process suffer from irreversible threaten. In this case, introducing a separated hybrid electrolytes system would be a solution, in which the cathodic GIC process is conducted in IL electrolyte and the anodic GIC process can be reversibly conducted in another specific electrolyte system.

4.2.3 Discovering a reversible Li-GIC process in super-concentrated ether-based electrolyte.

Ethers have been widely employed as electrolyte solvents for Li batteries (Li-ion, Li-air, Li-S, etc.).[95-96] However, although ethers own high Li salt solubility and good reductive stability for accommodating Li metal, ether-based electrolytes have been limited into primary Li batteries only assembled with Li metal. This embarrassment can be attributed to their intrinsically incompatible nature with graphite anode in corresponding full cells.[75] The co-intercalation of ether molecules would lead to the destruction of graphite layer and unstable SEI-formation.[97]

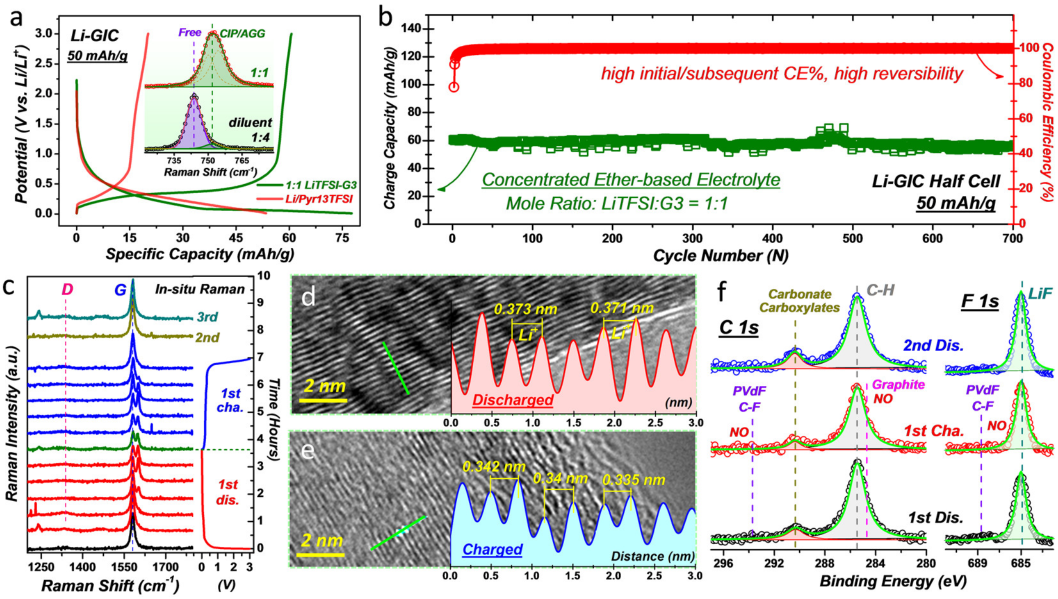

Figure 11. Reversible Li-GIC mechanism in super-concentrated ether electrolyte (1:1 mole ratio, LiTFSI:G$_3$). (a) Voltage profiles of graphite-Li half-cells. Compared with the IL system (red trace), the cell assembled with super-concentrated G$_3$ (green trace) exhibits improved reversible capacity during the initial cycle. Inset shows the Raman spectra of LiTFSI/G$_3$-based electrolyte with different mole ratios: typical diluent (1:4) and super-concentrated (1:1). The blue shift of TFSI-related peak observed in super-concentrated

electrolyte indicates the evolution of electrolyte structure, which directly leads to the essential difference on Li-GIC mechanisms. (**b**) Long-term cycling performance of graphite-Li half-cell at 50 mA/g. (**c**) Time dependent in-situ Raman spectra harvested during Li-GIC process (current density, 35 mA/g). The reversible variation trend of G-band indicates a reversible change of graphitic structure during Li^+ de/intercalation. (**d, e**) HR-TEM images of cycled graphite electrodes with each of their corresponding lattice distances: (**d**) after discharge (intercalated state) and (**d**) after charge (de-intercalated state). Compared with the lattice distance (~0.335 nm) observed in pristine graphite (Fig. 6b), the reversible Li^+ de/intercalation have been achieved. (**f**) XPS spectra (C 1s and F 1s) of cycled graphite electrodes harvested after 1st discharge (black trace), 1st charge (red trace) and 2nd discharge (blue trace) processes, respectively. Without re-exposure of graphite electrode, the LiF-dominated SEI film stably covered on the electrode surface and do not suffer from obvious change once it form after the initial discharge process.

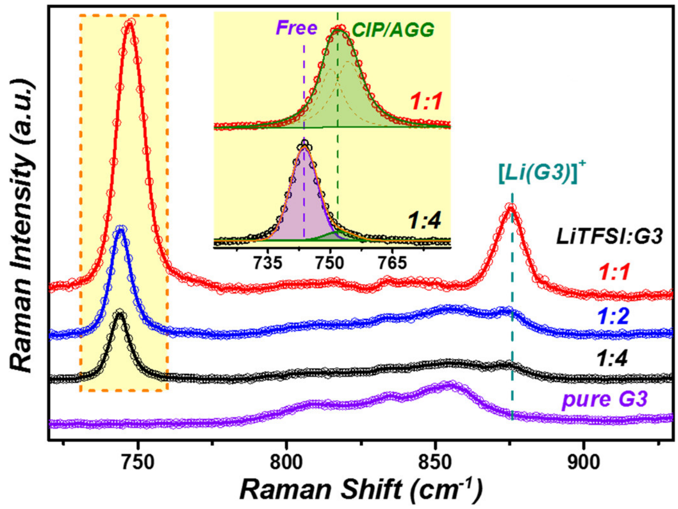

Figure 12. Raman spectra of ether-based electrolytes with various LiTFSI concentrations.

Herein, based on Raman spectroscopy analysis, we want to demonstrate the different electrolyte structures and various Li^+ solvation degrees in LiTFS-G_3 electrolytes with different LiTFSI salt concentrations. Different from the typically dilute electrolyte composed by solvent-separated-ion-pair (SSIP), super-concentrated electrolyte system (equimolar complexation of G_3 solvent and LiTFSI salt) is composed by a structure of contact-ion-pair (CIP), $[Li(G_3)_1][TFSI]$. Both the $TFSI^-$ and G_3 do not freely exist in the CIP-composed system. A G_3-based solvated shell tightly wrap around the Li^+ cation, resulting in the formation of highly solvated $[Li(G_3)_1]^+$. On the other hand, the soften behavior of Li^+ (based on the classic H) induces the interaction between solvated Li^+ and $TFSI^-$, resulting in the essential evolution of solvent structures. The formation of specific CIP structure has been exemplified by the blue shift of SNS stretching mode (variation of TFSI state) and increasing intensity of Li^+-glyme related peak (variation of Li^+ solvated state). The further discussion on the features of these "glyme-LiTFSI solvate ionic liquids" electrolyte systems had been extended by previous studies.[77, 80, 97-98]

For example, the typically dilute LiTFSI-ether electrolyte is mainly composed by solvent-separated ion-pairs (SSIP), in which both the ether molecule and $TFSI^-$ anion exist in a relative free state.[80, 99] Different from dilute system, within super-concentrated electrolyte, the freedom of ether (for example: triglyme ether, G_3) molecule can be largely restrained by the equimolar complexation (LiTFSI:G_3, 1:1) with LiTFSI salt, which indicates a formation of contact-ion-pair (CIP) structure, $[Li(G_3)_1TFSI]$. The formation of the specific solvated structure (Li^+ surrounded by a G_3 shell) has been exemplified by Raman observation, the blue shift of SNS stretching mode (Figure 11a inset) and increasing of Li^+-G_3 related peak Figure 12).[80] Without free G_3 molecule, the aggregated CIP structure effectively restrain the G_3 co-intercalation, which demonstrated by the pure Li^+-intercalation plateau (below 0.5 V vs. Li/Li^+) and disappearance of co-intercalation-related plateau (around 0.8 V vs. Li/Li^+) during GIC process (Figure 11a and Figure 13).[75, 81]

Contrary to the low CE (merely around 70%) and limited cycling stability observed in typical diluted ether electrolytes, both the cycle life (over 700 cycles) and CE (stabilized around 99.8%) have been remarkably improved in CIP-composed super-concentrated electrolyte (Figure 11b and Figure 14). This essentially change can be assigned by completed determining factors for both de-solvation and co-intercalation processes, which are discussed in Figure 14. More importantly, although sharing the similar IL-related structural features (consisting of large $[Li(G_3)]+$ cation and TFSI-anion), the irreversible capacity loss has been well controlled in super-concentrated electrolyte system, and the 1st CE has been largely improved (Figure 11a and Figure 15), performing a superior Li-GIC reversibility.

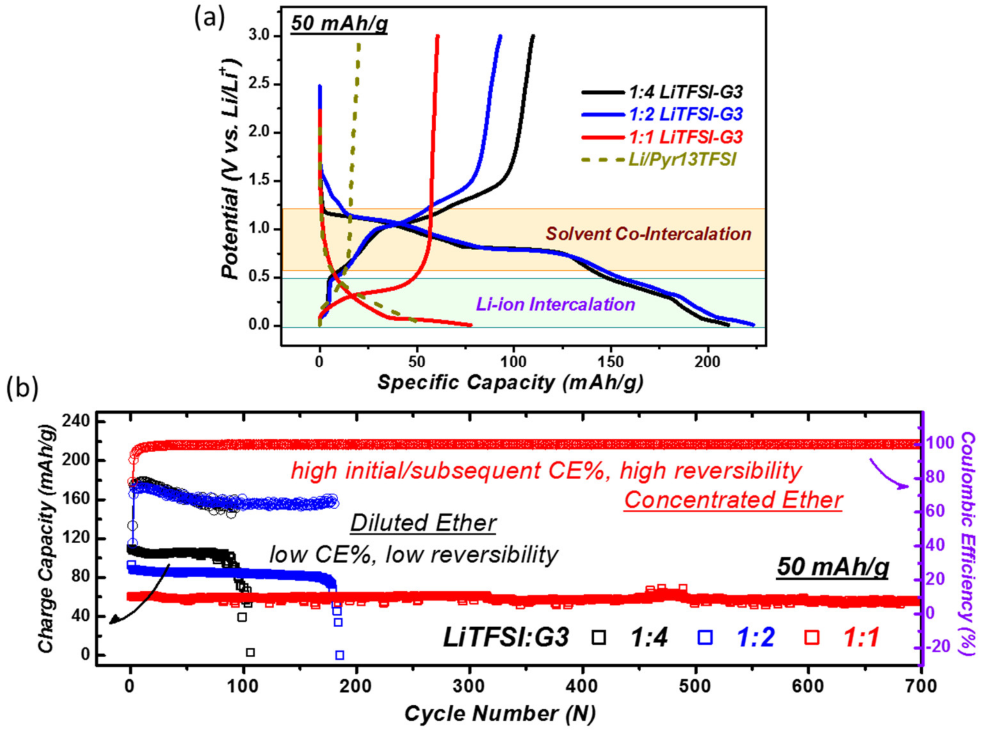

Figure 13. Li-GIC (graphite/Li half-cell) cycling performance of cells assembled by ether-based electrolytes with various LiTFSI concentrations. (a) Voltage profiles of the initial cycle. (b) Charge capacity and coulombic efficiency (CE) hysteresis against cycle number harvested from the corresponding cells.

The discharge/charge curves observed in typical dilute ether-based electrolytes present a traditional ether co-intercalation plateau around 0.8 V vs. Li/Li$^+$.[81] Compared with the subsequent Li$^+$ intercalation stage, the solvent co-intercalation contributes dominate discharge capacity. However, in typical dilute ether-based electrolyte system, the low CE (merely around 70%) indicates the existence of irreversible de/intercalation behavior in this system. Based on Kang and co-workers, the pure co-intercalation behavior observed in typical ether-based electrolyte can achieve very stable cycling performance (cycling with ~0.2 V vs. Li/Li$^+$ cut-off voltage, not extend to Li-intercalation region), which can be attributed to a SEI-free Li-GIC process.[75] However, once extended to a lower intercalation potential (0.01 V cut-off voltage), the irreversible behavior can be clearly observed. The related degradation mechanism would be further explained based on related spectroscopic evidences revealed below.

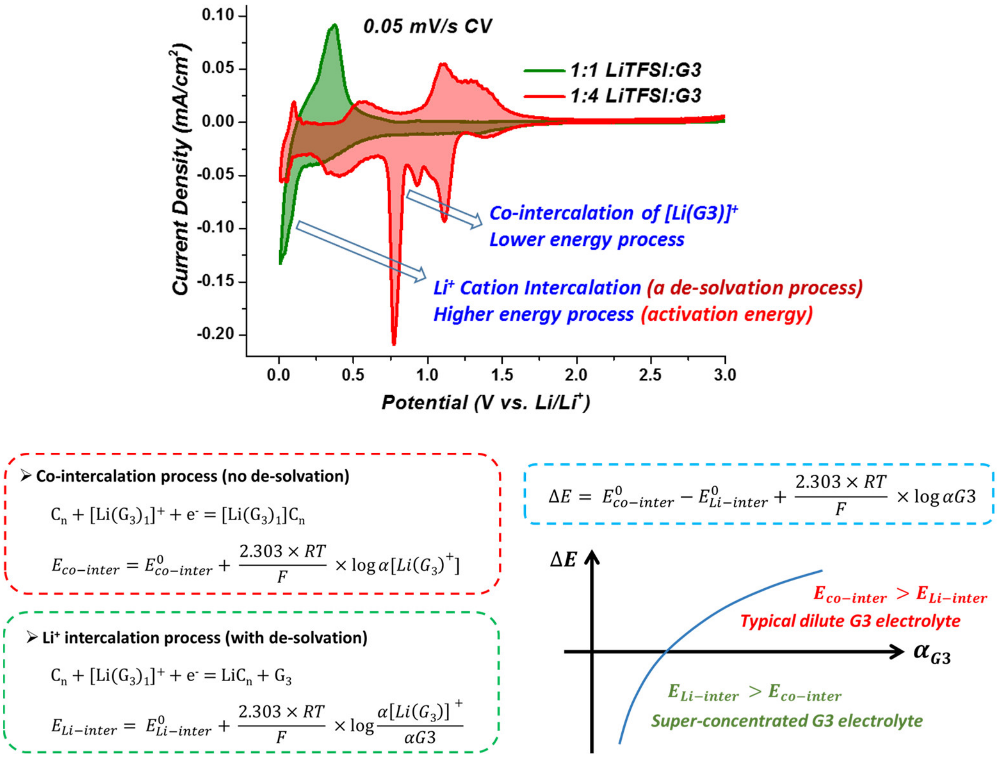

Figure 14. Proposed determining factors for co-intercalation or de-solvation behaviors during Li-GIC. Cyclic voltammetry (CV) curves collected during scanning in typical dilute G3-based electrolyte (red trace) and super-concentrated G3-based electrolyte (green trace). The half-cells are assembled with graphite/Li for Li-GIC investigations. Then, proposed determining factors for co-intercalation or pure Li+ intercalation (firstly de-solvation) behaviors during Li-GIC are discussed by corresponding equilibrium equations.

The related CV curves fit well with the corresponding galvanostatic curves shown in Figure 13. Notably, there is a very important step before pure Li^+ intercalation (GIC) process, Li^+ de-solvation process. However, there presents no de-solvation process for co-intercalation. The essential determining factor would be the activity of free G_3 solvent molecule in electrolyte, which can directly determine the order of co-intercalation and de-solvation processes.[80-81] For super-concentrated electrolyte, the activity of free G_3 solvent molecule has been largely restrained, which would lead to the de-solvation process takes the lead of solvent co-intercalation.

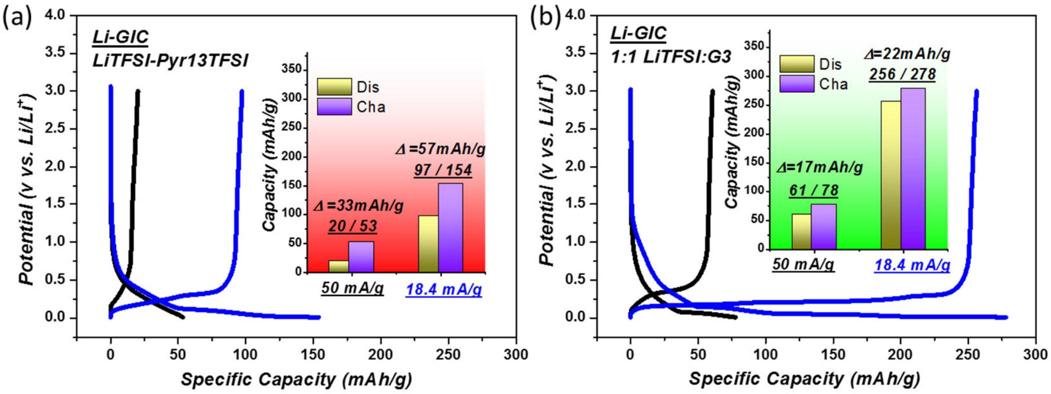

Figure 15. Voltage profiles of Li-GIC (graphite/Li half-cell) processes observed in different electrolyte systems. (a) IL-based electrolyte system (1.5 M LiTFSI-Pyr_{13}TFSI); (b) Super-concentrated ether-based electrolyte system (LiTFSI-G_3, 1:1 mole ratio). GIC processes are performed at various current density: 50 mA/g (black traces); 18.4 mA/g (blue traces). Corresponding discharge/charge capacities have been summarized in the inset bar graphs.

Based on the discharge/charge capacities summarized above, several differences between the two electrolyte systems have been revealed. With the reduction of current rate, the discharge capacity observed in IL system has been extended (from ~50 mAh/g to ~150 mAh/g). However, the irreversible discharge capacity also simultaneously increases (from 33 mAh/g to 57 mAh/g). With the increasing of discharge capacity, more Pyr_{13}^+ has been trapped within graphite layer, which can be well explained by the degradation mechanism proposed in Figure 6. However, for the newly-introduced super-concentrated system, the discharged capacity can be enlarged to ~270 mAh/g at smaller current rate. At the same time, the irreversible capacity loss during the initial cycle do not suffer from obvious increasing trend. In another word, the 1st cycle irreversible capacity loss has not relationship with the discharge capacity (amount of intercalated cation), which is very similar as the fixed SEI-formation related consumption observed in typical EC/DMS based electrolyte systems. The SEI-consumed irreversible capacity would be further proved by related characterizations.

Actually, as a pioneering work, Watanabe and co-workers have reported the related phenomenon by XRD analysis on graphite layer structure.[81] In this study, not only the long-term cycling stability in super-concentrated electrolyte system has been further improved for practical application, but also, on mechanism level, the intercalation behavior and SEI-formation process are systematically illustrated with the comparison of typical systems (dilute electrolyte and IL). For in-situ Raman observation, the reversible splitting of G-band observed in super-concentrated system (Figure 11c) exhibits sharp difference against the irreversible splitting in IL (Pyr_{13}^+ residue, Figure 6a) and remaining D-band in diluted ether (disordered layer defects, Figure 16).

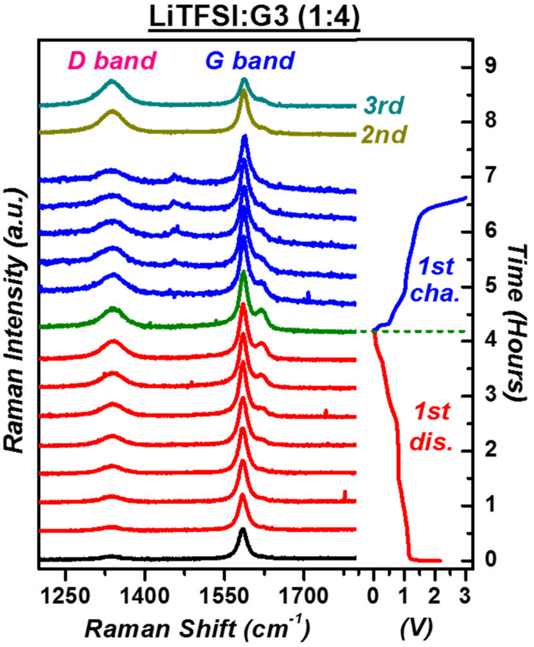

Figure 16. In-situ Raman observation of Li-GIC (graphite/Li half-cell) process conducted in typical dilute ether-based electrolyte (1:4 LiTFSI/G_3).

Compared with the reversible variation trend of G-band observed during Li-GIC process in super-concentrated electrolyte system (Figure 3c), there present an obvious difference in the related process conducted in typical dilute ether-based electrolyte system: the irreversible formation of D-band after de-intercalation. The splitting and restoration of G-band indicate the reversible intercalation of Li^+ cation. However, the irreversible formation of D-band indicates the formation of irreversible defects and disorder in the graphite structure during 1st discharging.[76] What was worse, the defects/destroy of the graphite structure become more and more serious during the subsequent cycles. Moreover, after several cycles, the formation of a small shoulder (band D') can be also attributed to the formation of defects in the crystal structure of graphite.[71-72, 76]

More visual HR-TEM images further exemplify the related reversible Li-GIC, in which the pure Li^+-intercalated layer displays a single expanded interlayer distance around 0.37 nm after discharging (Figure 11d). After charging, the graphene layers reversibly restore back to the pristine state (around 0.34 nm distance, Figure 11e), which indicates a reversible de-intercalation process has been achieved in super-concentrated electrolyte system. As a comparison, in diluted electrolyte system, the larger distance observed at intercalated state (~0.47 nm, Figure 17) and related irreversible behavior present well coincide with the classic co-intercalation explanation. Moreover, shown in SEM images collected after cycling Figure 18), the tightly layered structure can be well maintained in CIP-composed ether electrolyte, while the wrinkled interlayers and exfoliation of graphite structure can be clearly observed in diluted electrolyte condition. Turning to another important issue, the formation of stable LiF-composed SEI in CIP-composed electrolyte can be illustrated by corresponding XPS spectra (Figure 11f).

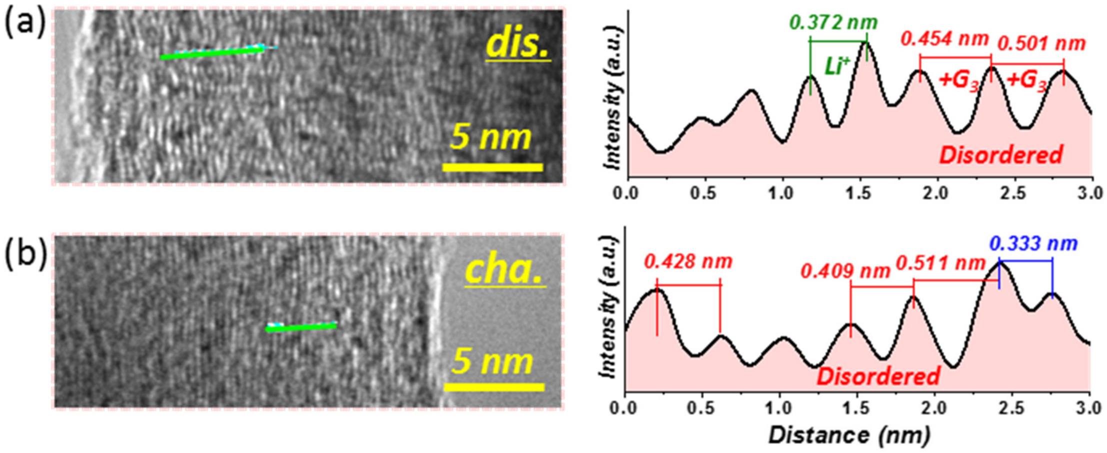

Figure 17. HR-TEM images and related lattice distances of graphite electrodes harvested after cycling (Li-GIC half-cell) in typical dilute ether-based electrolyte. (a) After discharging (intercalated state); (b) After charging (de-intercalated state).

Although the expansion/restoration of graphitic lattice distance (0.372 nm: Li^+ intercalated; 0.333 nm: Li^+ de-intercalated) proves the existence of reversible Li^+-related intercalation behavior during Li-GIC process, the irreversible lattice expansion (0.4~0.5 nm: solvent co-intercalated) also indicates the irreversible structure variation during cycling. The irreversible destroy of graphite layer structure can also be proved by the corresponding exfoliation phenomenon observed in SEM images.

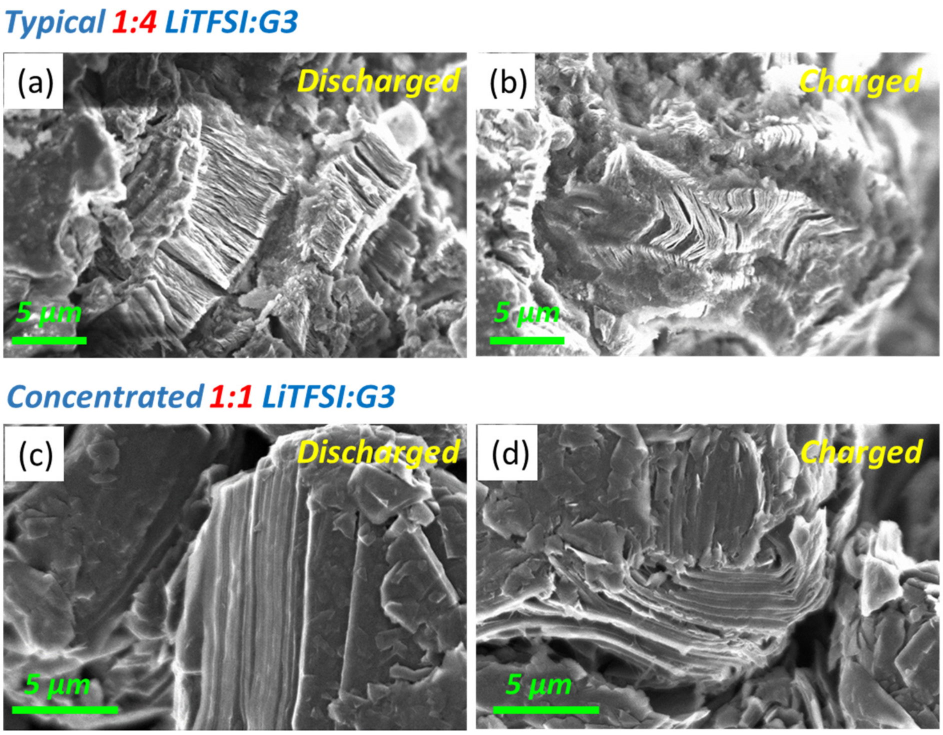

Figure 18. SEM images of the graphite electrodes collected after Li-GIC cycling. Graphite electrodes harvested from the Li-GIC graphite/Li half-cell assembled with typical dilute ether-based electrolyte (1:4 LiTFSI-G_3): (a) after discharging (intercalated state) and (b) after charging (de-intercalated state); super-concentrated ether-based electrolyte (1:1 LiTFSI-G_3): after (c) discharging and (d) charging.

Severely exfoliation of graphite galleries can be clearly observed on the graphite electrodes cycled in dilute ether-based electrolyte. The irreversible morphological degradation can be attributed to the commonly-accepted solvent (ether) co-intercalation upon Li-GIC process. This is also well consistent with the evidences exhibited in Figure 17-18. As a comparison, no obvious gallery exfoliation can be observed on the cycled graphite electrode harvested from the super-concentrated electrolyte system, which also indicates a reversible and stable Li-GIC behavior can be conducted in this specific electrolyte system.

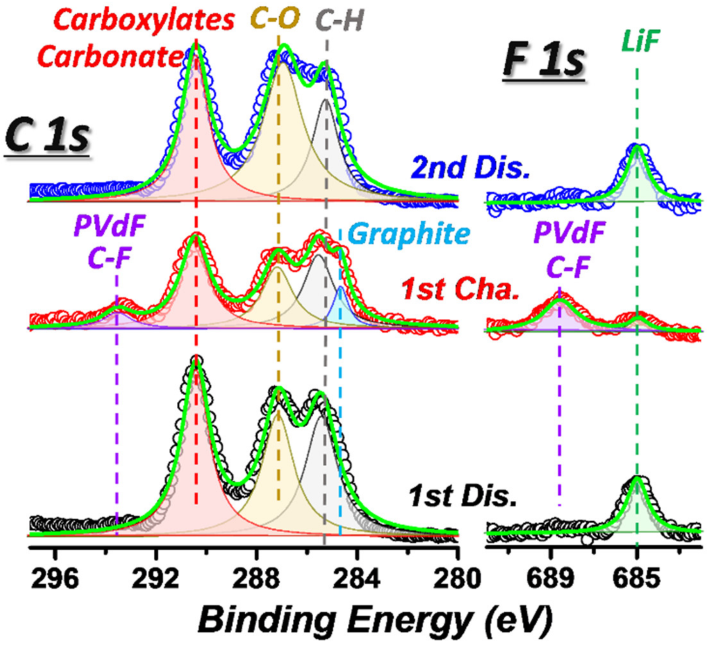

Figure 19. XPS spectra (C 1s and F 1s) of cycled graphite electrodes harvested from Li-GIC half cells cycled in typical dilute ether-based electrolyte. After 1st discharging (black trace); after 1st charging (red trace); after 2nd discharging (blue trace).

Different from IL and super-concentrated ether electrolytes, ether solvent molecules (relative free state) can also be reduced on graphite surface during discharging. In this case, the components of SEI film formed in dilute ether electrolyte system include carboxylates and carbonate species. This is very different from the SEI film (dominate by LiF) observed in IL (Figure 6e) and super-concentrated ether electrolyte (Figure 11f) systems. However, the abnormal re-constrution of SEI can be observed, which is very similar as the one revealed in IL system (Figure 6e). Notably, the destroy of SEI film (exposure of graphite cathode) after 1st charging can be attributed to the de-intercalation of co-intercalated species. Thus, SEI cannot stably exist due to co-intercalation behavior observed in dilute ether-based electrolyte system. This phenomenon also well coincide with the low CE (keeps around 70%) observed in the specific system. Further quantitative analysis (NMR, Figure 20) can confirm this phenomenon.

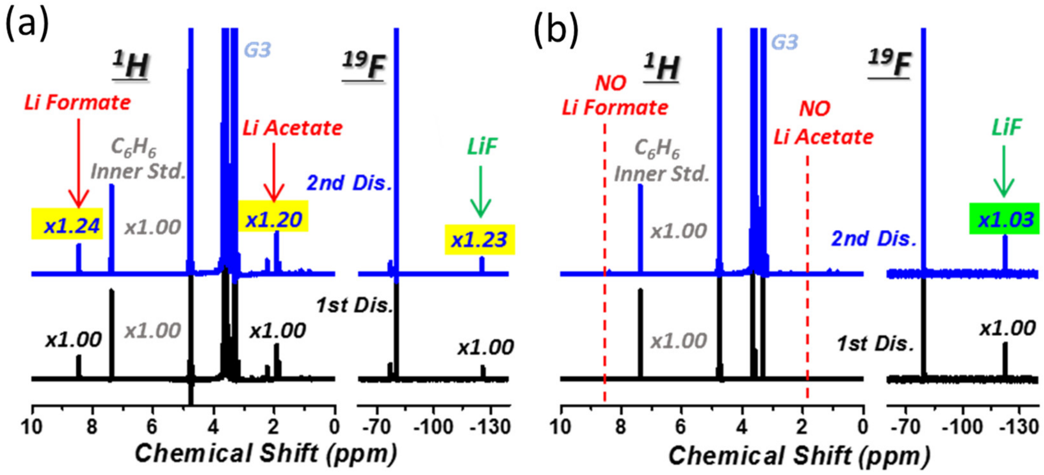

Figure 20. NMR analysis for SEI components during Li-GIC. (a) In typical dilute ether-based electrolyte system; (b) In newly-introduced super-concentrated ether-based electrolyte system. ^1H and ^{19}F NMR spectra of D_2O-extracted components from discharged Li-GIC half-cells (un-rinsed graphite electrode and separator). Both the carboxylates (formate and acetate, etc.) and flouride (LiF, etc.) are quantitatively estimated based on the normalized peaks of C_6H_6 and C_6H_5F internal/inner standards.

Corresponding XPS analysis performed in Figure 11f and Figure 19 have qualitatively confirmed the components of SEI film formed on graphite surface in corresponding systems. For dilute ether-based electrolyte system, NMR results indicate the formation of both LiF and carboxylates component within SEI, which is consistent with the XPS results (Figure 19). More importantly, the amount of SEI components increase after 2nd discharging. This is a strong evidence to prove the proposed destory and re-construction of SEI film. As for super-concentrated ether-based electrolyte system, NMR results indicate the formation of LiF and the absence of carboxylates component within SEI, which is consistent with the XPS results (Figure 11f). Notably, the amount of LiF keeps constant after 2nd discharging. This is also a strong evidence to prove the superior stability of LiF-based SEI film formed in this specific system.

While, in diluted electrolyte condition, the re-exposure of graphite electrode and re-building of new SEI can be revealed upon 1st charging and subsequent discharging processes, respectively Figure 19). Furthermore, this negative destroy and re-construction of SEI film during co-intercalation can be further proved by quantitative NMR characterizations Figure 20). Besides, the component of SEI present different. In diluted electrolyte system, the carbonate/carboxylates-related components in SEI can be assigned to the decomposition of free G_3 molecules. While in CIP-composed condition, all of the G_3 molecules tightly surround Li^+ (equimolar) and the related reductive stability has been largely enhanced. Thus, similar as the IL-based electrolyte system (Figure 6e), the dominate component of SEI formed in CIP-composed ether electrolyte system is LiF, which produced from reduction of $TFSI^-$. In conclusion, super-concentrated ether-based electrolyte can be regarded as a superior electrolyte system during Li-GIC process, and the reversible Li^+-related de-/intercalation profit from the formation of stable LiF-composed SEI and restraining effect against solvent co-intercalation.

4.2.4 Synergistical hybrid electrolytes design for dual-graphite battery with capacity-equivalent electrodes loading.

Turning back to the dual-graphite battery technology, combining the advantages of each electrolytes together and avoiding their inherent defects would be a promising modification target, which obviously cannot be achieved by rigidly mixing of the different electrolyte system. Herein, we want to introduce a specific hybrid electrolytes design strategy to realize the target. Typically, the concept of liquid-based hybrid electrolytes system has been introduced by integration of aqueous and organic electrolytes into a single battery.[82, 84, 100] Separated by a lithium super-ionic conductor glass film (LISICON), lithium metal can provide the most negative potential (-0.34 V vs. NHE) on the organic anodic side, while an aqueous system can be conducted on the cathodic side (oxygen reduction in Li-air system, NiOOH/$Ni(OH)_2$ couple in Li-NiOOH battery, etc.).[85, 101-102] Herein, we want to further design a dual-organic hybrid electrolytes strategy for dual-graphite battery. As illustrated in Figure 21a, super-concentrated LiTFSI-G_3 electrolyte system is employed within the anodic side, insuring the high reversibility of Li-GIC process. While on the cathodic side, the high oxidative stability of IL-based electrolyte system (LiTFSI-Pyr_{13}TFSI) enables the achievement of reversible TFSI-GIC process. In this case, both the IL co-intercalation on anode and electrolyte oxidation on cathode can be restrained. By simultaneous taking advantages and avoiding drawbacks of each electrolyte systems, this synergistical hybrid electrolytes design would become a promising strategy to realize the reversible long-term cycling of dual-graphite battery systems.

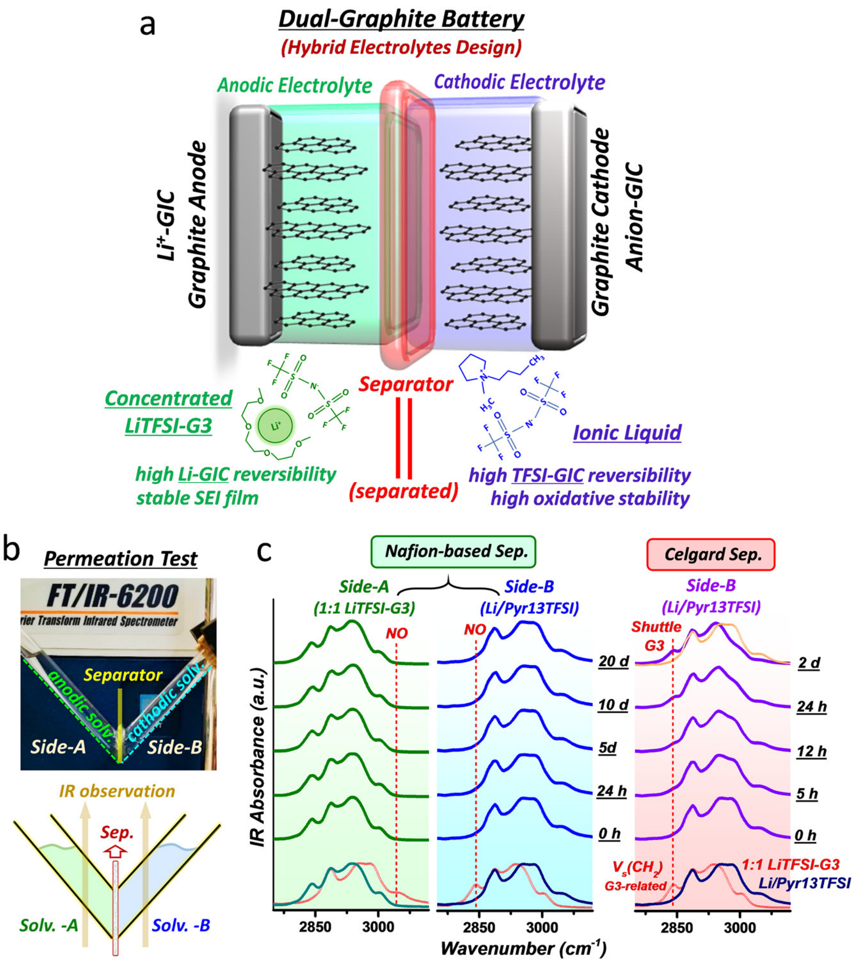

Figure 21. Nafion-based separator introduction into a dual-graphite cell fabricated with a hybrid electrolytes design. (**a**) Schematic illustration of hybrid electrolytes design strategy. The core of the design is taking full advantage of each electrolyte systems during cationic/anodic GIC processes by combining them into a single full-cell system, and simultaneously avoiding their shortcoming by separated them apart into different regions. Based on its excellent oxidative stability against high voltage decomposition, we hire IL

(LiTFSI-Pyr_{13}TFSI) as cathodic electrolyte, and try to obtain high TFSI-GIC reversibility. Without worrying about its irreversible co-intercalation on anodic side, we can employ a specific separator to restrain its diffusion to anode side. Similarly, due to its high Li-GIC reversibility, we use super-concentrated LiTFSI-G_3 as anodic electrolyte, and the separator should also prevent its shuttling to the cathodic side. (**b-c**) Permeation tests to assess the separation effect of Nafion-based separator. (**b**) For the homemade V-type device, each chambers are isolated by a fixed middle-layer separator and injected with different electrolytes (side-A: super-concentrated LiTFSI-G_3; side-B: LiTFSI-Pyr_{13}TFSI). Certain trace amount of electrolyte can be take out for IR observation after aging. (**c**) Separation effect comparison between Nafion-based separator and typical Celgard (as comparison). After 20 days aging, based on time-dependently collected IR spectra, no obvious shuttling can be observed on both sides in Nafion-based separator-assembled device. However, Celgard separator cannot effectively prevent the interpenetration of electrolyte, since obvious shuttling can be observed after only 2 days aging.

Inspired by the newly-designed organic/organic hybrid electrolytes strategy, introducing a suitable separator to separate each electrolytes becomes the final core issue. Compared with the conventional solid-state electrolytes (LISICON, etc.) and polymer electrolytes (PEO, etc.), perfluorinated sulfonate ionomer, namely Nafion, has been selected to obstruct the pair of electrolyte systems, due to its higher flexibility and lower cost than LISICON, and higher conductivity than PEO.[103-104] Benefit from the internal narrow channel structure, the barrier property of Nafion has been well accepted in Li-S batteries by effectively restraining the shuttling of polysulfide compound.[103, 105] However, introducing Nafion as an independent separator to isolate pair of different electrolyte systems still remains a challenging attempt. The permeation assessment of related isolation effect has been performed in a home-made V-type device (Figure 21b), in which the Nafion-based separator is fixed in the middle of device after traditional lithiation pretreatment. After certain period of aging, the probable inter-permeation can be well assessed by FTIR observation. Fabricated by Nafion-based separator, each of the selected electrolytes (side A: super-concentrated LiTFSI-G_3; side B: LiTFSI-

Pyr$_{13}$TFSI) can be well restricted in each of their corresponding chamber after 20 days aging. No obvious inter-permeation can be detected by sensitively spectroscopic characterization (left pair of groups in Figure 21c). As comparison, assembled with typical Celagrd separator, clear shuttling can be proved by the observation of ether-related adsorption peaks (around 2840 cm^{-1}, right group in Figure 21c) within counter side (IL side) after merely 2 days aging. In this case, Nafion-based separator can be regarded as an appropriate separator to achieve the design of hybrid electrolytes system.

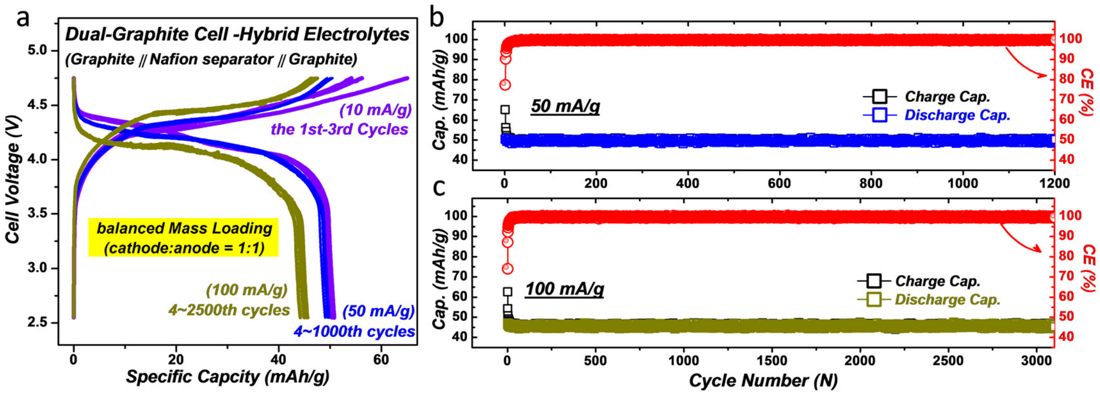

Figure 22. Electrochemical performance of dual-graphite cell fabricated by the hybrid electrolytes design strategy. Long term cycling performance of dual-graphite full cell fabricated with hybrid electrolytes strategy and capacity-equivalent cathode/anode mass loading proportion. Cell voltage range: 2.6-4.8 V. Specific current density: 10 mA/g for initial 1-3 cycles; 50 and 100 mA/g for subsequent cycles, respectively. (**a**) Voltage profiles. Charge/discharge and coulombic efficiency hysteresis against cycle number at (**b**) 50 mA/g and (**c**) 100 mA/g current rates.

Finally, fabricated by hybrid electrolytes and Nafion-based separator, dual-graphite full cell performance has been shown in Figure 22a to 22c. Due to the similar GIC capacities (around 50 mAh/g) on both electrodes, the full-cells are assembled with equi-mass of graphite electrodes (1:1 mass loading), which follow the basic criterion of practical capacity-equivalent loading proportion. The current density for the initial 3 cycles has been fixed at 10 mA/g, while the following cycles are performed at 50 and 100 mA/g, respectively. Based on collected voltage profiles (Figure 22a), the obvious irreversible capacity can be clearly observed during the first cycle, which is mainly related to the SEI-formation on anode and “kinetic hindrance” on cathode during very initial cycles.[36-37] As for the subsequent cycles, the hybrid electrolytes system exhibits stable long-term cycling stability at 50 mA/g over 1200 cycles, with a high CE (average value of 99.9%). Furthermore, although suffer from more polarization at higher current density (100 mA/g), the related system still keeps high CE and high capacity retention rate after over 3000 cycles (over 3 months cycling, Figure 22c).

4.3 Conclusion

In this study, after systematically revealing the intrinsic defect of IL during anodic Li-GIC process within dual-graphite full-cell system, we introduce a novel organic/organic-combined hybrid electrolytes design strategy. By retaining the IL electrolyte within the cathodic side, the anodic electrolyte has been replaced with CIP-composed super-concentrated ether-based electrolyte, in which the reversibility of Li-GIC can be largely enhanced. More importantly, a Nafion-based separator has been employed to successfully separate each of the specific electrolyte systems. Benefited from the synergistical hybrid electrolytes design, the advantages of both electrolyte systems can be sufficiently utilized (strong oxidative stability of IL and good Li-GIC reversibility of CIP-composed ether electrolyte), while simultaneously, each of their drawbacks can be well restrained (irreversible co-intercalation of IL on anode and oxidative decomposition of ether on cathode) by spatially isolated away from corresponding electrodes. Profit from this hybrid electrolytes design, the long-term cycling stability of dual-graphite batteries have been largely enhanced (over 3000 cycles at 100 mA/g), exhibiting a capacity close to 50 mAh/g and a CE exceeding 99.9% during cycling. Moreover, as a basic criterion of practical application, the full-cells herein have been assembled with balanced capacity-equivalent loading proportion, which is firstly highlighted to the forefront in related dual-graphite/ion cell systems. Besides, on mechanism level, the cation-GIC processes conducted in various electrolyte systems have been carefully revealed by the employment of systematical characterization methods (in-situ Raman, HR-TEM, XPS, NMR, etc.), which is also essential important for providing fundamental insights into the future development of graphite-intercalation-chemistry (GIC). Overall, despite of its moderate specific capacity intrinsically limited by anion-GIC process, the dual-graphite technology fabricated by hybrid electrolytes design strategy would still act as a promising candidate for practical stationary energy storage devices, since it owns high output voltage, ultra-stable cycling, low-cost graphite-based electrodes and safety superiorities over traditional Li-ion battery systems.

Chapter 5

General Conclusion and Perspective

Chapter 5. General Conclusion and Perspective

In this thesis, a unique organic/organic-combined hybrid electrolytes design strategy has been specifically introduced into two high-voltage Li-ion full-cell system.

For the first system, related research focus on typical cathode for Li-ion battery. The superior oxidative stability of ionic liquid (catholyte) can support the 5 V-class $LiNi_{0.5}Mn_{1.5}O_4$ cathode working at harsh elevated temperature, while a good Li-GIC reversibility of super-concentrated ether electrolyte (anolyte) can guarantee the operation of graphite anode. Simultaneously, drawbacks of each electrolytes can be well restrained (irreversible co-intercalation of ionic liquid on anode and oxidative decomposition of ether on cathode) by spatially isolated away from corresponding electrodes by the employment of sieve-like MOF-based separator.

As for the second system, dual-carbon/graphite battery system. The advantages of both electrolyte systems can be sufficiently utilized (strong oxidative stability of ionic liquid and good Li-GIC reversibility of super-concentrated ether electrolyte), while simultaneously, each of their drawbacks can be well restrained (irreversible co-intercalation of ionic liquid on anode and oxidative decomposition of ether on cathode) by spatially isolated away from corresponding electrodes.

Benefit from the advantages of each electrolyte systems (cathodic and anodic), the separator fully separate them into each of their own spaces. This desgin strategy would be empolyed into varying battery systems, for example, Li-O2 battery system with soluble redox mediators, and Na/K-ion battery systems.

References

(1) Grey, C. P.; Tarascon, J. M. Sustainability and in Situ Monitoring in Battery Development. *Nat. Mater.* **2017**, *16*, 45-56.

(2) Cano, Z. P.; Banham, D.; Ye, S.; Hintennach, A.; Lu, J.; Fowler, M.; Chen, Z. Batteries and Fuel Cells for Emerging Electric Vehicle Markets. *Nat. Energy* **2018**, *3*, 279-289.

(3) Schmuch, R.; Wagner, R.; Hörpel, G.; Placke, T.; Winter, M. Performance and Cost of Materials for Lithium-Based Rechargeable Automotive Batteries. *Nat. Energy* **2018**, *3*, 267-278.

(4) Li, W.; Song, B.; Manthiram, A. High-Voltage Positive Electrode Materials for Lithium-Ion Batteries. *Chem. Soc. Rev.* **2017**.

(5) Zeng, X.; Zhan, C.; Lu, J.; Amine, K. Stabilization of a High-Capacity and High-Power Nickel-Based Cathode for Li-Ion Batteries. *Chem* **2018**, *4*, 690-704.

(6) Xu, G.; Pang, C.; Chen, B.; Ma, J.; Wang, X.; Chai, J.; Wang, Q.; An, W.; Zhou, X.; Cui, G.*, et al.* Prescribing Functional Additives for Treating the Poor Performances of High‐Voltage (5 V‐Class) Lini0.5mn1.5o4/Mcmb Li‐Ion Batteries. *Adv. Energy Mater.* **2017**, *8*, 1701398.

(7) Chen, S.; Zheng, J.; Mei, D.; Han, K. S.; Engelhard, M. H.; Zhao, W.; Xu, W.; Liu, J.; Zhang, J. G. High‐Voltage Lithium‐Metal Batteries Enabled by Localized High‐Concentration Electrolytes. *Adv. Mater.* **2018**, *0*, 1706102.

(8) Shi, J.-L.; Xiao, D.-D.; Ge, M.; Yu, X.; Chu, Y.; Huang, X.; Zhang, X.-D.; Yin, Y.-X.; Yang, X.-Q.; Guo, Y.-G.*, et al.* High-Capacity Cathode Material with High Voltage for Li-Ion Batteries. *Adv. Mater.* **2018**, 1705575-n/a.

(9) Suo, L.; Xue, W.; Gobet, M.; Greenbaum, S. G.; Wang, C.; Chen, Y.; Yang, W.; Li, Y.; Li, J. Fluorine-Donating Electrolytes Enable Highly Reversible 5-V-Class Li Metal Batteries. *Proc. Natl. Acad. Sci.* **2018**, doi.org/10.1073/pnas.1712895115.

(10) Aurbach, D.; Markovsky, B.; Talyossef, Y.; Salitra, G.; Kim, H.-J.; Choi, S. Studies of Cycling Behavior, Ageing, and Interfacial Reactions of Lini0.5mn1.5o4 and Carbon Electrodes for Lithium-Ion 5-V Cells. *J. Power Sources* **2006**, *162*, 780-789.

(11) Yang, L.; Ravdel, B.; Lucht, B. L. Electrolyte Reactions with the Surface of High Voltage Lini0.5mn1.5o4 Cathodes for Lithium-Ion Batteries. *Electrochem. Solid-State Lett.* **2010**, *13*, A95-A97.

(12) Brutti, S.; Greco, G.; Reale, P.; Panero, S. Insights About the Irreversible Capacity of Lini0.5mn1.5o4 Cathode Materials in Lithium Batteries. *Electrochim. Acta* **2013**, *106*, 483-493.

(13) Pieczonka, N. P. W.; Liu, Z.; Lu, P.; Olson, K. L.; Moote, J.; Powell, B. R.; Kim, J.-H. Understanding Transition-Metal Dissolution Behavior in Lini0.5mn1.5o4 High-Voltage Spinel for Lithium Ion Batteries. *J. Phys. Chem. C* **2013**, *117*, 15947-15957.

(14) Kim, J.-H.; Pieczonka, N. P. W.; Li, Z.; Wu, Y.; Harris, S.; Powell, B. R. Understanding the Capacity Fading Mechanism in Lini0.5mn1.5o4/Graphite Li-Ion Batteries. *Electrochim. Acta* **2013**, *90*, 556-562.

(15) Michalak, B.; Berkes, B. B.; Sommer, H.; Bergfeldt, T.; Brezesinski, T.; Janek, J. Gas Evolution in Lini0.5mn1.5o4/Graphite Cells Studied in Operando by a Combination of Differential Electrochemical Mass Spectrometry, Neutron Imaging, and Pressure Measurements. *Anal. Chem.* **2016**, *88*, 2877-2883.

(16) Xu, M.; Zhou, L.; Dong, Y.; Chen, Y.; Garsuch, A.; Lucht, B. L. Improving the Performance of Graphite/Lini0. 5mn1. 5o4 Cells at High Voltage and Elevated Temperature with Added Lithium Bis (Oxalato) Borate (Libob). *J. Electrochem. Soc.* **2013**, *160*, A2005-A2013.

(17) Xu, M.; Tsiouvaras, N.; Garsuch, A.; Gasteiger, H. A.; Lucht, B. L. Generation of Cathode Passivation Films Via Oxidation of Lithium Bis(Oxalato) Borate on High Voltage Spinel (Lini0.5mn1.5o4). *J. Phys. Chem. C* **2014**, *118*, 7363-7368.

(18) Noguchi, T.; Yamazaki, I.; Numata, T.; Shirakata, M. Effect of Bi Oxide Surface Treatment on 5v Spinel Lini0.5mn1.5−Xtixo4. *J. Power Sources* **2007**, *174*, 359-365.

(19) Arunkumar, T. A.; Manthiram, A. Influence of Chromium Doping on the Electrochemical Performance of the 5v Spinel Cathode Limn1.5ni0.5o4. *Electrochim. Acta* **2005**, *50*, 5568-5572.

(20) Lu, D.; Xu, M.; Zhou, L.; Garsuch, A.; Lucht, B. L. Failure Mechanism of Graphite/Lini0.5mn1.5o4 Cells at High Voltage and Elevated Temperature. *J. Electrochem. Soc.* **2013**, *160*, A3138-A3143.

(21) Yoon, T.; Park, S.; Mun, J.; Ryu, J. H.; Choi, W.; Kang, Y.-S.; Park, J.-H.; Oh, S. M. Failure Mechanisms of Lini0.5mn1.5o4 Electrode at Elevated Temperature. *J. Power Sources* **2012**, *215*, 312-316.

(22) Hu, L.; Zhang, Z.; Amine, K. Fluorinated Electrolytes for Li-Ion Battery: An Fec-Based Electrolyte for High Voltage Lini0.5mn1.5o4/Graphite Couple. *Electrochem. Commun.* **2013**, *35*, 76-79.

(23) Wang, F.-M.; Pradanawati, S. A.; Yeh, N.-H.; Chang, S.-C.; Yang, Y.-T.; Huang, S.-H.; Lin, P.-L.; Lee, J.-F.; Sheu, H.-S.; Lu, M.-L.*, et al.* Robust Benzimidazole-Based Electrolyte Overcomes High-Voltage and High-Temperature Applications in 5 V Class Lithium Ion Batteries. *Chem. Mater.* **2017**, *29*, 5537-5549.

(24) Wang, J.; Nie, P.; Xu, G.; Jiang, J.; Wu, Y.; Fu, R.; Dou, H.; Zhang, X. High ‐ Voltage Lini0.45cr0.1mn1.45o4 Cathode with Superlong Cycle Performance for Wide Temperature Lithium ‐ Ion Batteries. *Adv. Funct. Mater.* **2017**, *28*, 1704808.

(25) Besenhard, J. O.; Fritz, H. P. The Electrochemistry of Black Carbons. *Angew. Chem. Int. Ed.* **1983**, *22*, 950-975.

(26) Carlin, R. T.; Hugh, C.; Fuller, J.; Trulove, P. C. Dual Intercalating Molten Electrolyte Batteries. *J. Electrochem. Soc.* **1994**, *141*, L73-L76.

(27) Seel, J.; Dahn, J. Electrochemical Intercalation of Pf 6 into Graphite. *J. Electrochem. Soc.* **2000**, *147*, 892-898.

(28) Shu, Z.; McMillan, R.; Murray, J. Electrochemical Intercalation of Lithium into Graphite. *J. Electrochem. Soc.* **1993**, *140*, 922-927.

(29) Olivier, J. P.; Winter, M. Determination of the Absolute and Relative Extents of Basal Plane Surface Area and "Non-Basal Plane Surface" Area of Graphites and Their Impact on Anode Performance in Lithium Ion Batteries. *Journal of power sources* **2001**, *97*, 151-155.

(30) Read, J. A.; Cresce, A. V.; Ervin, M. H.; Xu, K. Dual-Graphite Chemistry Enabled by a High Voltage Electrolyte. *Energy Environ. Sci.* **2014**, *7*, 617-620.

(31) Aubrey, M. L.; Long, J. R. A Dual−Ion Battery Cathode Via Oxidative Insertion of Anions in a Metal–Organic Framework. *J. Am. Chem. Soc.* **2015**, *137*, 13594-13602.

(32) Tong, X.; Zhang, F.; Ji, B.; Sheng, M.; Tang, Y. Carbon-Coated Porous Aluminum Foil Anode for High-Rate, Long-Term Cycling Stability, and High Energy Density Dual-Ion Batteries. *Adv. Mater.* **2016**, *28*, 9979-9985.

(33) Aladinli, S.; Bordet, F.; Ahlbrecht, K.; Tübke, J.; Holzapfel, M. Anion Intercalation into a Graphite Cathode from Various Sodium-Based Electrolyte Mixtures for Dual-Ion Battery Applications. *Electrochimica Acta* **2017**, *231*, 468-478.

(34) Rodríguez-Pérez, I. A.; Ji, X. Anion Hosting Cathodes in Dual-Ion Batteries. *ACS Energy Letters* **2017**, *2*, 1762-1770.

(35) Dahn, J.; Seel, J. Energy and Capacity Projections for Practical Dual‐Graphite Cells. *J. Electrochem. Soc.* **2000**, *147*, 899-901.

(36) Placke, T.; Fromm, O.; Lux, S. F.; Bieker, P.; Rothermel, S.; Meyer, H.-W.; Passerini, S.; Winter, M. Reversible Intercalation of Bis (Trifluoromethanesulfonyl) Imide Anions from an Ionic Liquid Electrolyte into Graphite for High Performance Dual-Ion Cells. *J. Electrochem. Soc.* **2012**, *159*, A1755-A1765.

(37) Schmuelling, G.; Placke, T.; Kloepsch, R.; Fromm, O.; Meyer, H.-W.; Passerini, S.; Winter, M. X-Ray Diffraction Studies of the Electrochemical Intercalation of Bis(Trifluoromethanesulfonyl)Imide Anions into Graphite For dual-Ion Cells. *Journal of Power Sources* **2013**, *239*, 563-571.

(38) Rothermel, S.; Meister, P.; Schmuelling, G.; Fromm, O.; Meyer, H.-W.; Nowak, S.; Winter, M.; Placke, T. Dual-Graphite Cells Based on the Reversible Intercalation of Bis(Trifluoromethanesulfonyl)Imide Anions from an Ionic Liquid Electrolyte. *Energy Environ. Sci.* **2014**, *7*, 3412-3423.

(39) Meister, P.; Fromm, O.; Rothermel, S.; Kasnatscheew, J.; Winter, M.; Placke, T. Sodium-Based Vs. Lithium-Based Dual-Ion Cells: Electrochemical Study of Anion Intercalation/De-Intercalation into/from Graphite and Metal Plating/Dissolution Behavior. *Electrochimica Acta* **2017**, *228*, 18-27.

(40) Shi, X.; Zhang, W.; Wang, J.; Zheng, W.; Huang, K.; Zhang, H.; Feng, S.; Chen, H. (Emim)+(Pf6)− Ionic Liquid Unlocks Optimum Energy/Power Density for Architecture of Nanocarbon‐Based Dual‐Ion Battery. *Adv. Energy Mater.* **2016**, *6*, 1601378.

(41) Fan, J.; Zhang, Z.; Liu, Y.; Wang, A.; Li, L.; Yuan, W. An Excellent Rechargeable Pp14tfsi Ionic Liquid Dual-Ion Battery. *Chem. Commun.* **2017**, *53*, 6891-6894.

(42) Nádherná, M.; Reiter, J.; Moškon, J.; Dominko, R. Lithium Bis(Fluorosulfonyl)Imide–Pyr14tfsi Ionic Liquid Electrolyte Compatible with Graphite. *J. Power Sources* **2011**, *196*, 7700-7706.

(43) Placke, T.; Bieker, P.; Lux Simon, F.; Fromm, O.; Meyer, H.-W.; Passerini, S.; Winter, M., Dual-Ion Cells Based on Anion Intercalation into Graphite from Ionic Liquid-Based Electrolytes. In *Z. Phys. Chem.*, 2012; Vol. 226, p 391.

(44) Fromm, O.; Meister, P.; Qi, X.; Rothermel, S.; Huesker, J.; Meyer, H. W.; Winter, M.; Placke, T. Study of the Electrochemical Intercalation of Different Anions from Non-Aqueous Electrolytes into a Graphite-Based Cathode. *ECS Trans.* **2014**, *58*, 55-65.

(45) Rodríguez-Pérez, I. A.; Jian, Z.; Waldenmaier, P. K.; Palmisano, J. W.; Chandrabose, R. S.; Wang, X.; Lerner, M. M.; Carter, R. G.; Ji, X. A Hydrocarbon Cathode for Dual-Ion Batteries. *ACS Energy Letters* **2016**, *1*, 719-723.

(46) Jiang, C.; Fang, Y.; Lang, J.; Tang, Y. Integrated Configuration Design for Ultrafast Rechargeable Dual-Ion Battery. *Advanced Energy Materials* **2017**, 1700913-n/a.

(47) Liao, H.-J.; Chen, Y.-M.; Kao, Y.-T.; An, J.-Y.; Lai, Y.-H.; Wang, D.-Y. A Freestanding Cathode Electrode Design for High-Performance Sodium Dual-Ion Battery. *J. Phys. Chem. C* **2017**, 24463–24469.

(48) Shaju, K. M.; Bruce, P. G. Nano-Lini 0.5 Mn 1.5 O 4 Spinel: A High Power Electrode for Li-Ion Batteries. *Dalton Trans.* **2008**, *40*, 5471-5475.

(49) Zhou, L.; Zhao, D.; Lou, X. D. Lini0. 5mn1. 5o4 Hollow Structures as High ‑ Performance Cathodes for Lithium ‑ Ion Batteries. *Angew. Chem. Int. Ed.* **2012**, *124*, 243-245.

(50) Zhang, X.; Cheng, F.; Yang, J.; Chen, J. Lini0.5mn1.5o4 Porous Nanorods as High-Rate and Long-Life Cathodes for Li-Ion Batteries. *Nano Letters* **2013**, *13*, 2822-2825.

(51) Qiao, Y.; Li, S. R.; Yu, Y.; Chen, C. H. Synthesis and Electrochemical Properties of High Performance Yolk-Structured Limn2o4 Microspheres for Lithium Ion Batteries. *J. Mater. Chem. A* **2013**, *1*, 860-867.

(52) Qiao, Y.; Yu, Y.; Jin, Y.; Guan, Y. B.; Chen, C. H. Synthesis and Electrochemical Properties of Porous Double-Shelled Mn2o3 Hollow Microspheres as a Superior Anode Material for Lithium Ion Batteries. *Electrochimica Acta* **2014**, *132*, 323-331.

(53) Ameloot, R.; Gobechiya, E.; Uji ‑ i, H.; Martens, J. A.; Hofkens, J.; Alaerts, L.; Sels, B. F.; De Vos, D. E. Direct Patterning of Oriented Metal–Organic Framework Crystals Via Control over Crystallization Kinetics in Clear Precursor Solutions. *Adv. Mater.* **2010**, *22*, 2685-2688.

(54) Guerrero, V. V.; Yoo, Y.; McCarthy, M. C.; Jeong, H.-K. Hkust-1 Membranes on Porous Supports Using Secondary Growth. *J. Mater. Chem.* **2010**, *20*, 3938-3943.

(55) Bai, S.; Liu, X.; Zhu, K.; Wu, S.; Zhou, H. Metal–Organic Framework-Based Separator for Lithium–Sulfur Batteries. *Nature Energy* **2016**, *1*, 16094.

(56) Liang, H.; Qiu, X.; Zhang, S.; Zhu, W.; Chen, L. Study of Lithiated Nafion Ionomer for Lithium Batteries. *Journal of applied electrochemistry* **2004**, *34*, 1211-1214.

(57) Su, L.; Darling, R. M.; Gallagher, K. G.; Xie, W.; Thelen, J. L.; Badel, A. F.; Barton, J. L.; Cheng, K. J.; Balsara, N. P.; Moore, J. S. An Investigation of the Ionic Conductivity and Species Crossover of Lithiated Nafion 117 in Nonaqueous Electrolytes. *Journal of The Electrochemical Society* **2016**, *163*, A5253-A5262.

(58) Qiao, Y.; Guo, S.; Zhu, K.; Liu, P.; Li, X.; Jiang, K.; Sun, C.-J.; Chen, M.; Zhou, H. Reversible Anionic Redox Activity in Na3ruo4 Cathodes: A Prototype Na-Rich Layered Oxide. *Energy Environ. Sci.* **2018**, *11*, 299-305.

(59) Qiao, Y.; Yi, J.; Wu, S.; Liu, Y.; Yang, S.; He, P.; Zhou, H. Li-Co_2 Electrochemistry: A New Strategy for Co_2 Fixation and Energy Storage. *Joule* **2017**, *1*, 359-370.

(60) Qiao, Y.; Wu, S.; Yi, J.; Sun, Y.; Guo, S.; Yang, S.; He, P.; Zhou, H. From O_2^- to Ho_2^-: Reducing by-Products and Overpotential in Li-O_2 Batteries by Water Addition. *Angew. Chem. Int. Ed.* **2017**, *56*, 4960-4964.

(61) Xiao, J.; Chen, X.; Sushko, P. V.; Sushko, M. L.; Kovarik, L.; Feng, J.; Deng, Z.; Zheng, J.; Graff, G. L.; Nie, Z.*, et al.* High-Performance Lini0.5mn1.5o4 Spinel Controlled by Mn3+ Concentration and Site Disorder. *Adv. Mater.* **2012**, *24*, 2109-2116.

(62) Idemoto, Y.; Narai, H.; Koura, N. Crystal Structure and Cathode Performance Dependence on Oxygen Content of Limn1.5ni0.5o4 as a Cathode Material for Secondary Lithium Batteries. *J. Power*

Sources **2003**, *119-121*, 125-129.

(63) Kim, J. H.; Myung, S. T.; Yoon, C. S.; Kang, S. G.; Sun, Y. K. Comparative Study of Lini0.5mn1.5o4-Δ and Lini0.5mn1.5o4 Cathodes Having Two Crystallographic Structures: Fd3̅M and P4332. *Chem. Mater.* **2004**, *16*, 906-914.

(64) Pereira, N.; Ruotolo, M. C.; Lu, M. Y.; Badway, F.; Amatucci, G. G. Elevated Temperature Performance of High Voltage Li1+Ymn1.5ni0.5o4−Xfx Spinel in Window-Shifted Li-Ion Cells. *J. Power Sources* **2017**, *338*, 145-154.

(65) Markevich, E.; Baranchugov, V.; Aurbach, D. On the Possibility of Using Ionic Liquids as Electrolyte Solutions for Rechargeable 5v Li Ion Batteries. *Electrochem. Commun.* **2006**, *8*, 1331-1334.

(66) Borgel, V.; Markevich, E.; Aurbach, D.; Semrau, G.; Schmidt, M. On the Application of Ionic Liquids for Rechargeable Li Batteries: High Voltage Systems. *J. Power Sources* **2009**, *189*, 331-336.

(67) Gao, X.-W.; Feng, C.-Q.; Chou, S.-L.; Wang, J.-Z.; Sun, J.-Z.; Forsyth, M.; MacFarlane, D. R.; Liu, H.-K. Lini0.5mn1.5o4 Spinel Cathode Using Room Temperature Ionic Liquid as Electrolyte. *Electrochim. Acta* **2013**, *101*, 151-157.

(68) Gilbert, J. A.; Shkrob, I. A.; Abraham, D. P. Transition Metal Dissolution, Ion Migration, Electrocatalytic Reduction and Capacity Loss in Lithium-Ion Full Cells. *J. Electrochem. Soc.* **2017**, *164*, A389-A399.

(69) Dong, Y.; Young, B. T.; Zhang, Y.; Yoon, T.; Heskett, D. R.; Hu, Y.; Lucht, B. L. Effect of Lithium Borate Additives on Cathode Film Formation in Lini0.5mn1.5o4/Li Cells. *ACS Appl. Mater. Interfaces* **2017**, *9*, 20467-20475.

(70) Kim, D.; Park, S.; Chae, O. B.; Ryu, J. H.; Kim, Y.-U.; Yin, R.-Z.; Oh, S. M. Re-Deposition of Manganese Species on Spinel Limn2o4 Electrode after Mn Dissolution. *Journal of The Electrochemical Society* **2012**, *159*, A193-A197.

(71) Hardwick, L. J.; Ruch, P. W.; Hahn, M.; Scheifele, W.; Kötz, R.; Novák, P. In Situ Raman Spectroscopy of Insertion Electrodes for Lithium-Ion Batteries and Supercapacitors: First Cycle Effects. *Journal of Physics and Chemistry of Solids* **2008**, *69*, 1232-1237.

(72) Sethuraman, V. A.; Hardwick, L. J.; Srinivasan, V.; Kostecki, R. Surface Structural Disordering in Graphite Upon Lithium Intercalation/Deintercalation. *J. Power Sources* **2010**, *195*, 3655-3660.

(73) Domi, Y.; Doi, T.; Nakagawa, H.; Yamanaka, T.; Abe, T.; Ogumi, Z. In Situ Raman Study on Reversible Structural Changes of Graphite Negative-Electrodes at High Potentials in Lipf6-Based Electrolyte Solution. *J. Electrochem. Soc.* **2016**, *163*, A2435-A2440.

(74) Kim, H.; Hong, J.; Park, Y. U.; Kim, J.; Hwang, I.; Kang, K. Sodium Storage Behavior in Natural Graphite Using Ether‐Based Electrolyte Systems. *Adv. Funct. Mater.* **2015**, *25*, 534-541.

(75) Kim, H.; Lim, K.; Yoon, G.; Park, J. H.; Ku, K.; Lim, H. D.; Sung, Y. E.; Kang, K. Exploiting Lithium–Ether Co‐Intercalation in Graphite for High‐Power Lithium‐Ion Batteries. *Adv. Energy Mater.* **2017**, 1700418.

(76) Markervich, E.; Salitra, G.; Levi, M. D.; Aurbach, D. Capacity Fading of Lithiated Graphite Electrodes Studied by a Combination of Electroanalytical Methods, Raman Spectroscopy and Sem. *J. Power Sources* **2005**, *146*, 146-150.

(77) Yamada, Y.; Furukawa, K.; Sodeyama, K.; Kikuchi, K.; Yaegashi, M.; Tateyama, Y.; Yamada, A. Unusual Stability of Acetonitrile-Based Superconcentrated Electrolytes for Fast-Charging Lithium-Ion

Batteries. *J. Am. Chem. Soc.* **2014**, *136*, 5039-5046.

(78) He, M.; Lau, K. C.; Ren, X.; Xiao, N.; McCulloch, W. D.; Curtiss, L. A.; Wu, Y. Concentrated Electrolyte for the Sodium–Oxygen Battery: Solvation Structure and Improved Cycle Life. *Angew. Chem. Int. Ed.* **2016**, *55*, 1-6.

(79) Zheng, J.; Lochala, J. A.; Kwok, A.; Deng, Z. D.; Xiao, J. Research Progress Towards Understanding the Unique Interfaces between Concentrated Electrolytes and Electrodes for Energy Storage Applications. *Adv. Sci.* **2017**, *4*, 1700032-n/a.

(80) Yoshida, K.; Nakamura, M.; Kazue, Y.; Tachikawa, N.; Tsuzuki, S.; Seki, S.; Dokko, K.; Watanabe, M. Oxidative-Stability Enhancement and Charge Transport Mechanism in Glyme–Lithium Salt Equimolar Complexes. *J. Am. Chem. Soc.* **2011**, *133*, 13121-13129.

(81) Moon, H.; Tatara, R.; Mandai, T.; Ueno, K.; Yoshida, K.; Tachikawa, N.; Yasuda, T.; Dokko, K.; Watanabe, M. Mechanism of Li Ion Desolvation at the Interface of Graphite Electrode and Glyme–Li Salt Solvate Ionic Liquids. *J. Phys. Chem. C* **2014**, *118*, 20246-20256.

(82) Zhou, H.; Wang, Y.; Li, H.; He, P. The Development of a New Type of Rechargeable Batteries Based on Hybrid Electrolytes. *ChemSusChem* **2010**, *3*, 1009-1019.

(83) Keller, M.; Varzi, A.; Passerini, S. Hybrid Electrolytes for Lithium Metal Batteries. *J. Power Sources* **2018**, *392*, 206-225.

(84) Wang, Y.; Zhou, H. A New Type Rechargeable Lithium Battery Based on a Cu-Cathode. *Electrochem. Commun.* **2009**, *11*, 1834-1837.

(85) He, P.; Zhang, T.; Jiang, J.; Zhou, H. Lithium–Air Batteries with Hybrid Electrolytes. *J. Phys. Chem. Lett.* **2016**, *7*, 1267-1280.

(86) Senthilkumar, S. T.; Bae, H.; Han, J.; Kim, Y. Enhancing Capacity Performance by Utilizing the Redox Chemistry of the Electrolyte in a Dual‐Electrolyte Sodium‐Ion Battery. *Angew. Chem. Int. Ed.* **2018**, 5433.

(87) Rowsell, J. L. C.; Yaghi, O. M. Effects of Functionalization, Catenation, and Variation of the Metal Oxide and Organic Linking Units on the Low-Pressure Hydrogen Adsorption Properties of Metal−Organic Frameworks. *J. Am. Chem. Soc.* **2006**, *128*, 1304-1315.

(88) Chui, S. S.-Y.; Lo, S. M.-F.; Charmant, J. P.; Orpen, A. G.; Williams, I. D. A Chemically Functionalizable Nanoporous Material [Cu3 (Tma) 2 (H2o) 3] N. *Science* **1999**, *283*, 1148-1150.

(89) Hu, X.; Wang, J.; Li, Z.; Wang, J.; Gregory, D. H.; Chen, J. Mcnts@ Mno2 Nanocomposite Cathode Integrated with Soluble O2-Carrier Co-Salen in Electrolyte for High-Performance Li–Air Batteries. *Nano letters* **2017**, *17*, 2073-2078.

(90) Li, W.; Yao, H.; Yan, K.; Zheng, G.; Liang, Z.; Chiang, Y.-M.; Cui, Y. The Synergetic Effect of Lithium Polysulfide and Lithium Nitrate to Prevent Lithium Dendrite Growth. *Nature Common.* **2015**, *6*, 7436.

(91) Placke, T.; Rothermel, S.; Fromm, O.; Meister, P.; Lux, S. F.; Huesker, J.; Meyer, H.-W.; Winter, M. Influence of Graphite Characteristics on the Electrochemical Intercalation of Bis (Trifluoromethanesulfonyl) Imide Anions into a Graphite-Based Cathode. *Journal of the Electrochemical Society* **2013**, *160*, A1979-A1991.

(92) Dahn, J. R. Phase Diagram of Lixc6. *Phys. Rev. B* **1991**, *44*, 9170-9177.

(93) Balabajew, M.; Reinhardt, H.; Bock, N.; Duchardt, M.; Kachel, S.; Hampp, N.; Roling, B. In-Situ

Raman Study of the Intercalation of Bis(Trifluoromethylsulfonyl)Imid Ions into Graphite inside a Dual-Ion Cell. *Electrochimica Acta* **2016**, *211*, 679-688.

(94) Vetter, J.; Novák, P.; Wagner, M.; Veit, C.; Möller, K.-C.; Besenhard, J.; Winter, M.; Wohlfahrt-Mehrens, M.; Vogler, C.; Hammouche, A. Ageing Mechanisms in Lithium-Ion Batteries. *Journal of power sources* **2005**, *147*, 269-281.

(95) Yin, Y. X.; Xin, S.; Guo, Y. G.; Wan, L. J. Lithium–Sulfur Batteries: Electrochemistry, Materials, and Prospects. *Angew. Chem. Int. Ed.* **2013**, *52*, 13186-13200.

(96) Chen, Y.; Freunberger, S. A.; Peng, Z.; Barde, F.; Bruce, P. G. Li-O_2 Battery with a Dimethylformamide Electrolyte. *J. Am. Chem. Soc.* **2012**, *134*, 7952-7957.

(97) Yamada, Y.; Yaegashi, M.; Abe, T.; Yamada, A. A Superconcentrated Ether Electrolyte for Fast-Charging Li-Ion Batteries. *Chem. Commun.* **2013**, *49*, 11194-11196.

(98) Qiao, Y.; Liu, Y.; Jiang, K.; Li, X.; He, Y.; Li, Q.; Wu, S.; Zhou, H. Boosting the Cycle Life of Aprotic Li–O2 Batteries Via a Photo-Assisted Hybrid Li2o2-Scavenging Strategy. *Small Methods* **2018**, *2*, 1700284.

(99) Yoshida, K.; Tsuchiya, M.; Tachikawa, N.; Dokko, K.; Watanabe, M. Change from Glyme Solutions to Quasi-Ionic Liquids for Binary Mixtures Consisting of Lithium Bis(Trifluoromethanesulfonyl)Amide and Glymes. *J. Phys. Chem. C* **2011**, *115*, 18384-18394.

(100) Black, R.; Adams, B.; Nazar, L. F. Non-Aqueous and Hybrid Li-O_2 Batteries. *Adv. Energy Mater.* **2012**, *2*, 801-815.

(101) Wang, Y. G.; He, P.; Zhou, H. S. A Lithium-Air Capacitor-Battery Based on a Hybrid Electrolyte. *Energy Environ. Sci.* **2011**, *4*, 4994-4999.

(102) Li, H.; Wang, Y.; Na, H.; Liu, H.; Zhou, H. Rechargeable Ni-Li Battery Integrated Aqueous/Nonaqueous System. *J. Am. Chem. Soc.* **2009**, *131*, 15098-15099.

(103) Bauer, I.; Thieme, S.; Brückner, J.; Althues, H.; Kaskel, S. Reduced Polysulfide Shuttle in Lithium–Sulfur Batteries Using Nafion-Based Separators. *Journal of Power Sources* **2014**, *251*, 417-422.

(104) Yu, X.; Manthiram, A. Performance Enhancement and Mechanistic Studies of Room-Temperature Sodium–Sulfur Batteries with a Carbon-Coated Functional Nafion Separator and a Na2s/Activated Carbon Nanofiber Cathode. *Chem. Mater.* **2016**, *28*, 896-905.

(105) Jin, Z.; Xie, K.; Hong, X.; Hu, Z.; Liu, X. Application of Lithiated Nafion Ionomer Film as Functional Separator for Lithium Sulfur Cells. *Journal of Power Sources* **2012**, *218*, 163-167.

Acknowledgements

As the growth of a perfect man/woman is extraordinarily difficult, the writing of a perfect thesis is also virtually impossible. At the final moments of the preparation of this thesis, I would like to state that all the imperfection in it is due to my inabilities, yet all the “local” perfection is achieved with the help of many people. Their names are not only just printed on this piece of paper but also deeply engraved in my memory during the rest of my life.

First of all, great many thanks to my doctoral supervisor Prof. Haoshen Zhou for his excellent supervision and great help through the past 3 years. His guidance, support and friendship have been tremendous for me, and his way of working and guiding students will benefit me forever. Most importantly, Prof. Zhou share all of his knowledge and experience on both energy storage devices and electrochemistry with me, which undoubtedly is a huge treasure in my career. He shared a helping hand and saved me out from the cold winter in Hokkaido, and this was definitely a turning point for my life.

I wish to express my gratitude to Mr. Kezhu Jiang and Ms. Xiaowei Mu (Nanjing University) for helping me for the XPS, TEM and GC-MS characterizations. I would also like to thank Prof. dr. Shaohua Guo, Prof. Ping He, Dr. Yang Sun, Prof. Na Li, Prof. dr. Shichao Wu, Prof. dr. Kaiming Liao, Prof. dr. Jin Yi, Prof. dr. Xizheng Liu and Prof. dr. Kai Zhu for their help on discussion with my experiment results. Their rich experience has been invaluable during my doctoral period.

I would also like to thank Dr. Songyan Bai, Dr. Yang Liu, Dr. Qi Li, Mr. Xiang Li, Ms. Yibo He, Ms Linlin Wang, Mr. Feilong Qiu, Mr. Han Deng, Mr. Zhi Chang and Ms. Min Jia, as colleagues in my group, for sharing their discovery with me, which is extremely precious for my research.

Yet again, I would like to express my greatest sincere gratitude to Prof. Chunhua Chen in USTC-my Alma Mater. His kindly help saved my career when I was a troubled teenager during my 1st year in undergraduate times. After all this time, his encouragement still boost my motivation. And I would also like to extend my gratitude to other teachers in USTC, Prof. Yan Yu, Prof. Yi Xie, Prof. Changrong Xia and Prof. Shuhong Yu. Their care and help through the years have always encouraged me.

I would also like to acknowledge scholarships from China Scholarship Council and Japanese Ministry of Education

Last, but surely not the least, special thanks go to my parents and girlfriend for their constant care and support. I know all of you are fully behind me, always!

謝　辞

完璧な人間に成長するのは、非常に難しいと同じように、完璧な卒業論文を書くのも基本的には不可能だと思います。この卒業論文の中に様々な不足は私自身の無能で、小さいな完璧なところも方々に助けられて作ったものです。その人たちはこの一枚の紙に、名前を印刷されていることだけではなく、私の心にも深く刻んでいます。

来つくばしてから、この三年の間に、指導教官の周豪慎先生に熱心なご指導と色々なご支援を頂いて、心より深謝致します。周先生からのガイダンス、サポートなどに深く影響されて、周先生の学生に向ける指導方法や働く方式なども非常に良い勉強になりました。その中に一番重要なのは、周先生に電気化学の知識を常に共有されて、貴重な富になりました。

このほか、XPS、TEM、GC-MS に関する研究について、南京大学の何平先生、江克柱さん、穆晓玮さんに色々助けていただいて、深謝致します。産総研の郭少華先生、孫洋先生、李娜先生、呉士超先生、廖開明先生、易金先生、劉喜正先生と朱凱先生も、私の実験結果を検討していただいて、深謝致します。

同研究室の柏松岩さん、劉洋さん、李琪さん、李翔さん、賀亦柏さん、王琳琳さん、邱飛竜さん、鄧翰さん、常智さんと賈敏さんもいつも私に実験結果を検討していただいて、感謝致します。

学部時代の指導先生、中国科学技術大学の陳春華先生に再度感謝致します。学部一年生の時に、事理を弁えない私は、陳先生に出会って、色々を励まして頂いた言葉は今までも覚えております。中国科学技術大学の余彦先生、謝毅先生、夏長栄先生と兪書宏先生にもご指導を頂いて、深謝致します。

中国留学基金委と日本文部省に奨学金をいただいて深謝致します。

母国にいる両親からいつも各方面を全力で支援していただいて、深謝致します。

Publications (Doctoral Period)

(1) **Qiao, Y.**; Wu, S.; Yi, J.; Sun, Y.; Guo, S.; Yang, S.; He, P.; Zhou, H. *Angew. Chem. Int. Ed.* **2017**, *56*, 4960-4964.

(2) **Qiao, Y**.; Yi, J.; Wu, S.; Liu, Y.; Yang, S.; He, P.; Zhou, H. *Joule* **2017**, *1*, 359-370.

(3) **Qiao, Y.**; Guo, S.; Zhu, K.; Liu, P.; Li, X.; Jiang, K.; Sun, C.-J.; Chen, M.; Zhou, H. *Energy Environ. Sci.* **2018**, *11*, 299-305.

(4) **Qiao, Y.**; Yi, J.; Guo, S.; Sun, Y.; Wu, S.; Liu, X.; Yang, S.; He, P.; Zhou, H. *Energy Environ. Sci.* **2018**, *11*, 1211-1217.

(5) **Qiao, Y.**; Jiang, K.; Li, X.; Deng, H.; He, Y.; Chang, Z.; Wu, S.; Guo, S.; Zhou, H. *Adv. Energy Mater.* **2018**, *8*, 1801120.

(6) **Qiao, Y.**; He, Y.; Jiang, K.; Liu, Y.; Li, X.; Jia, M.; Guo, S.; Zhou, H. *Adv. Energy Mater.* **2018**, *8*, 1802322.

(7) **Qiao, Y.**; Wu, S.; Sun, Y.; Guo, S.; Yi, J.; He, P.; Zhou, H. *ACS Energy Letters* **2017**, *2*, 1869-1878.

(8) **Qiao, Y.**; He, Y.; Wu, S.; Jiang, K.; Li, X.; Guo, S.; He, P.; Zhou, H. *ACS Energy Letters* **2018**, *3*, 463-468.

(9) **Qiao, Y.**; Liu, Y.; Jiang, K.; Li, X.; He, Y.; Li, Q.; Wu, S.; Zhou, H. *Small Methods* **2018**, *2*, 1700284.

(10) Li, X.†; **Qiao, Y.† (equal contribution)**; Guo, S.; Xu, Z.; Zhu, H.; Zhang, X.; Yuan, Y.; He, P.; Ishida, M.; Zhou, H.. *Adv. Mater.* **2018**, *30*, 1705197.

(11) Li, Q.†; **Qiao, Y.† (equal contribution)**; Guo, S.; Jiang, K.; Li, Q.; Wu, J.; Zhou, H. *Joule* **2018**, *2*, 1134-1145.

(12) Wu, S.†; **Qiao, Y.† (equal contribution)**; Deng, H.; Zhou, H. *J. Mater. Chem. A* **2018**, *6*, 9816-9822.

(13) He, Y.†; **Qiao, Y.† (equal contribution)**; Zhou, H. *Dalton Transactions* **2018**, *47*, 6881-6887.

(14) Wu, S.; **Qiao, Y.**; Yang, S.; Ishida, M.; He, P.; Zhou, H. *Nature Comm.* **2017**, *8*, 15607.

(15) Wu, S.; Yi, J.; Zhu, K.; Bai, S.; Liu, Y.; **Qiao, Y.**; Ishida, M.; Zhou, H. *Adv. Energy Mater.* **2017**, *7*, 1601759.

(16) Yang, S.; **Qiao, Y.**; He, P.; Liu, Y.; Cheng, Z.; Zhu, J.-j.; Zhou, H. *Energy Environ. Sci.* **2017**, *10*, 972-978.

(17) Yi, J.; Liu, Y.; **Qiao, Y.**; He, P.; Zhou, H. *ACS Energy Letters* **2017**, *2*, 1378-1384.

(18) Bai, S.; Sun, Y.; Yi, J.; He, Y.; **Qiao, Y.**; Zhou, H. *Joule* **2018**, *2*, 2117-2132.

(19) He, Y.; Bai, S.; Chang, Z.; Li, Q.; **Qiao, Y.**; Zhou, H. *J. Mater. Chem. A* **2018**, *6*, 9032-9040.

(20) Jiang, K.; Xu, S.; Guo, S.; Zhang, X.; Zhang, X.; **Qiao, Y.**; Fang, T.; Wang, P.; He, P.; Zhou, H. *Nano Energy* **2018**, *52*, 88-94.

(21) Li, Q.; Jiang, K.; Li, X.; **Qiao, Y.**; Zhang, X.; He, P.; Guo, S.; Zhou, H. *Adv. Energy Mater.* **2018**, *8*, 1801162.

(22) Li, X.; Guo, S.; Deng, H.; Jiang, K.; **Qiao, Y.**; Ishida, M.; Zhou, H. *Journal of Materials Chemistry A* **2018**, *6*, 15517-15522.

(23) Li, X.; Guo, S.; Jiang, K.; **Qiao, Y.**; Ishida, M.; Zhou, H. *ACS Applied Materials & Interfaces* **2018**, *10*, 16-20.

(24) Liu, Y.; Yi, J.; **Qiao, Y.**; Wang, D.; He, P.; Li, Q.; Wu, S.; Zhou, H. *Energy Storage Materials* **2018**, *11*, 170-175.

(25) Wu, S.; **Qiao, Y.**; Deng, H.; He, Y.; Zhou, H. *The Journal of Physical Chemistry Letters* **2018**, *9*, 6761-6766.

(26) Wu, S.; **Qiao, Y.**; Jiang, K.; He, Y.; Guo, S.; Zhou, H. *Advanced Functional Materials* **2018**, *0*, 1706374.

(27) Wu, S.; **Qiao, Y.**; Yang, S.; Tang, J.; He, P.; Zhou, H. *ACS Catalysis* **2018**, *8*, 1082-1089.

(28) Qiu, F.; Zhang, X.; **Qiao, Y.**; Zhang, X.; Deng, H.; Shi, T.; He, P.; Zhou, H. *Energy Storage Materials* **2018**, *12*, 176-182.

(29) Chang, Z.; He, Y.; Deng, H.; Li, X.; Wu, S.; **Qiao, Y.**; Wang, P.; Zhou, H. A *Advanced Functional Materials* **2018**, *28*, 1804777.

(30) Deng, H.; **Qiao, Y.**; Wu, S.; Qiu, F.; Zhang, N.; He, P.; Zhou, H. *ACS Applied Materials & Interfaces* **2018**.

(31) He, Y.; Chang, Z.; Wu, S.; **Qiao, Y.**; Bai, S.; Jiang, K.; He, P.; Zhou, H. *Advanced Energy Materials* **2018**, *8*, 1802130.